Optimisation des paramètres de fabrication additive et de post-traitement thermique pour l'acier à outils H13

Étude approfondie des interactions entre microstructurales et des performances mécaniques en fonction des paramètres du procédé

Thèse présentée

Dans le cadre du programme de doctorat en ingénierie

En vue de l'obtention du grade de Philosophie doctor (Ph.D)

PAR

© Narges Omidi

Octobre, 2024

Composition du jury :

Abderrazak El Ouafi, président du jury, Université du Québec à Rimouski

Noureddine Barka, directeur de recherche, Université du Québec à Rimouski

Raef Cherif, évaluateur, Université du Québec à Rimouski

Hendra Hermawan, examinateur externe, Université Laval

Alexandre Bois-Brochu, examinateur externe, Centre de métallurgie du Québec

Dépôt initial le 29 mai 2024 Dépôt final le 25 octobre 2024

À tous les êtres chers qui ont été derrière ce travail…

REMERCIEMENTS

Cette thèse actuelle est le résultat de nombreuses heures de travail et de recherche qui ont couvert plus de trois ans et demi. Cela a été une période riche en apprentissage, en échange d'informations et en recherche approfondie, et la conclusion de cette phase n'aurait pas été possible sans la participation de nombreuses personnes.

Tout d'abord, j'exprime ma gratitude envers mon superviseur, monsieur **Noureddine Barka**, pour ses encouragements et ses conseils en tant que directeur de recherche. Sa disponibilité et ses conseils judicieux ont grandement contribué à l'avancement et à l'orientation de mes recherches. Je tiens à souligner particulièrement son énergie, sa passion pour la recherche et sa quête insatiable d'innovation, qui ont constitué une source constante de motivation, me permettant de surmonter les défis et d'atteindre mes objectifs.

J'aimerais également exprimer ma gratitude envers monsieur **Mohammad Jahazi**, professeur à l'École de Technologie Supérieure, pour son soutien moral, ses conseils précieux et ses commentaires pertinents. Son soutien continu et sa présence constante tout au long de ce parcours ont joué un rôle déterminant dans le développement de mes recherches.

Je tiens à exprimer ma sincère appréciation envers mes collègues actuels et anciens du laboratoire à l'UQAR, particulièrement monsieur Pedram Farhadipour, monsieur Asim Iltaf, monsieur Karim Bensalem, madame Lamya Baali et monsieur Mohamed Meher Monjez, pour leur collaboration inestimable dans la réalisation de ce travail.

J'exprime ma gratitude envers monsieur Jean Brousseau, ancien professeur à l'UQAR, et le personnel du département de mathématiques, informatique et génie, en particulier monsieur Charles-André Fraser, monsieur Bruno Tremblay et monsieur Samuel Gagnon, pour leur assistance inestimable dans les travaux expérimentaux.

Mes sincères remerciements vont également à mes collègues, monsieur Claude Belzile de l'Institut des sciences de la mer de Rimouski, et madame Manel Houria de l'École de technologie supérieure, pour leur assistance dans la réalisation de ce travail.

J'exprime également ma gratitude envers les membres du jury d'avoir accepté d'évaluer mon projet de recherche. Votre expertise, votre temps précieux et vos remarques pertinentes ont contribué à enrichir ma thèse.

Enfin, j'exprime ma gratitude particulière envers ma famille. Leur amour, leurs efforts, leur soutien et leurs encouragements m'ont grandement motivé lors de la réalisation de cette recherche. Leur présence tout au long de mon parcours était inestimable ; j'admets que, sans eux, je ne serais pas là où je suis aujourd'hui.

RÉSUMÉ

L'acier à outils H13 est largement utilisé pour les moules d'injection en raison de sa résistance exceptionnelle à la fatigue thermique, particulièrement à haute température. Les canaux de refroidissement conformes (CCC) ont récemment émergé comme une solution innovante pour améliorer la productivité des processus de moulage, excédant les systèmes de refroidissement traditionnels. Ces CCC sont fabriqués grâce à des méthodes de fabrication additive, notamment la fusion sur lit de poudre (PBF). Cependant, le PBF, ayant une complexité thermique et des taux de refroidissement rapides, génère une microstructure déséquilibrée qui affecte les propriétés mécaniques des alliages d'acier, y compris l'acier H13. Malgré les avantages potentiels du PBF, des paramètres de fabrication mal adaptés peuvent entraîner des défauts dans l'acier H13, comme des contraintes résiduelles élevées, une ségrégation élémentaire et une structure principalement martensitique. Ces défauts compromettent la résistance mécanique du matériau, le rendant inadapté aux exigences de l'industrie du moulage.

L'objectif principal de cette thèse est d'optimiser les propriétés mécaniques de l'acier H13 fabriqué par PBF pour satisfaire aux besoins de l'industrie du moulage. Le premier objectif est de mener une revue de la littérature sur la microstructure et le comportement mécanique de l'acier H13 fabriqué par PBF. Le second objectif est d’explorer les paramètres de processus affectant la porosité, la microstructure et les propriétés mécaniques. Le troisième objectif est d’analyser les effets des paramètres de post-traitement thermique sur la microstructure et les propriétés mécaniques.

La méthodologie de cette étude est divisée en trois phases. La phase 1 est sous forme d’une revue approfondie de la littérature sur la microstructure, le comportement mécanique et la résistance à la fatigue de l'acier H13 produit par PBF. Cette revue a mis en lumière les capacités et les limitations du PBF pour les composants en acier H13. La phase 2 a permis l’expérimentation sur les paramètres de processus pour évaluer leur impact sur la porosité, la microstructure et les propriétés mécaniques de l'acier H13. La troisième phase est l’étude des effets des paramètres de post-traitement thermique sur la microstructure et les propriétés mécaniques de l'acier H13, visant à améliorer sa durabilité et sa résistance mécanique.

Un des résultats majeurs de cette recherche a permis l'identification d'une ségrégation élémentaire mésoscopique pendant le processus PBF, où les éléments d'alliage se sont regroupés vers les bords du bain de fusion. Ce phénomène est resté indétectable dans le matériau tel qu'il est construit et n'avait pas été signalé auparavant. Cependant, après le traitement thermique du matériau, ce phénomène est devenu évident par la formation de particules d'oxyde dans les zones où les éléments se sont regroupés en raison de leur forte

affinité pour l'oxydation. Ces particules d'oxyde ont contribué à une résistance mécanique du H13 fabriqué par PBF inférieure à celle de l'acier H13 conventionnel. Un autre résultat important de cette étude a été la reconnaissance de l'importance du type de porosité et de son emplacement dans la résistance du matériau à la déformation plastique. Les porosités allongées (remarquées par "keyhole") près de la surface ont augmenté la susceptibilité du matériau à la formation de fissures et ont réduit sa ductilité. Une valeur optimisée des paramètres de traitement a permis de réduire la formation de porosité, en particulier près de la dernière couche imprimée. De plus, une corrélation entre la rugosité de surface et la ségrégation mésoscopique dans le matériau fabriqué par PBF a été établie. Lorsque les paramètres du traitement ont entraîné une forte entrée de chaleur, un bain de fusion instable avec une fusion non uniforme, appelée "Balling formation", est apparu, conduisant à une plus grande rugosité de surface. Plus ce phénomène était sévère, plus la ségrégation élémentaire était observée. Le motif de la formation de boules correspondait au motif de la formation d'oxyde. Ainsi, la qualité de surface servait d'indicateur de la ségrégation élémentaire dans le matériau fabriqué par PBF. Une autre découverte importante concernait les considérations post-traitement thermique pour le H13 fabriqué par PBF, en particulier concernant la croissance des particules d'oxyde pendant le traitement thermique. Comme pour le H13 conventionnel, dans le H13 fabriqué par PBF, l'augmentation de la température et du temps de revenu a amélioré la ductilité du matériau grâce à la transformation de la martensite dure en martensite revenue et à la précipitation des carbures; cependant, dans le H13 fabriqué par PBF, cela a également augmenté la taille des particules d'oxyde, ce qui a réduit la ductilité du matériau. La plage de température de revenu optimale a été déterminée à 500-550°C. Enfin, un traitement de recuit avant le revenu a été recommandé pour réduire les contraintes internes causées pendant le processus PBF avant le traitement de revenu. Cette thèse offre une exploration complète des relations complexes entre le processus PBF, la microstructure et les propriétés de l'acier H13. Elle apporte des connaissances précieuses pour l'amélioration et l'optimisation des matériaux utilisés dans la fabrication des moules d'injection. La découverte de la ségrégation élémentaire mésoscopique constitue une contribution unique, ouvrant la voie à de futures recherches et avancées dans la fabrication additive et la science des matériaux.

Mots clés : PBF, SLM, Acier à outils H13, Porosité en trou de serrure, Porosité gazeuse, Traitement de recuit, Traitement de revenu, Oxydation, Ségrégation élémentaire des alliages

ABSTRACT

H13 tool steel is widely used for injection molds due to its exceptional resistance to thermal fatigue, particularly at high temperatures. Conformal cooling channels (CCCs) have recently emerged as an innovative solution to improve the productivity of molding processes, surpassing traditional cooling systems. These CCCs are manufactured using additive manufacturing methods, particularly powder bed fusion (PBF). However, PBF, with its thermal complexity and rapid cooling rates, generates an unbalanced microstructure that affects the mechanical properties of steel alloys, including H13. Despite the potential advantages of PBF, poorly adapted manufacturing parameters can lead to defects in H13 steel, such as high residual stresses, elemental segregation, and a primarily martensitic structure. These defects compromise the mechanical strength of the material, making it unsuitable for the requirements of the molding industry.

The main objective of this thesis was to optimize the mechanical properties of H13 steel manufactured by PBF to meet the needs of the molding industry. The first goal was to conduct a literature review on the microstructure and mechanical behavior of H13 steel manufactured by PBF. The second goal was to explore the process parameters affecting porosity, microstructure, and mechanical properties. The third goal was to analyze the effects of post-heat treatment parameters on the microstructure and mechanical properties.

The methodology of this study was divided into three steps. Step 1 consisted of an in-depth literature review on the microstructure, mechanical behavior, and fatigue resistance of H13 steel produced by PBF. This review highlighted the capabilities and limitations of PBF for H13 steel components. Step 2 involved experimenting with process parameters to evaluate their impact on porosity, microstructure, and mechanical properties of H13 steel. The objective was to determine the best manufacturing conditions. Step 3 was focused on the study of the effects of post-heat treatment parameters on the microstructure and mechanical properties of H13 steel, aiming to improve durability and mechanical strength.

One of the major results of this research was the identification of mesoscopic elemental segregation during the PBF process, where alloying elements segregated towards the boundaries of the melt pool. This phenomenon remained undetectable in the as-built material and had not been previously reported. However, after the material was subjected to heat treatment, this phenomenon became evident through the formation of oxide particles in areas where elements had segregated due to their high affinity for oxidation. These oxide particles contributed to the lower mechanical strength of PBF-ed H13 compared to conventional H13. Another significant outcome of this study was the recognition of the importance of porosity

type and location in the material's resistance to plastic deformation. Elongated porosities (remarked by keyholes) near the surface increased the material's susceptibility to crack formation and reduced its ductility. An optimized value of processing parameters was found to mitigate porosity formation, particularly near the final printed layer.

Furthermore, a correlation between surface roughness and mesoscopic segregation in the PBF-ed material was established. When processing parameters resulted in high heat input, an unstable melting pool with non-uniform melting, referred to as "balling formation," occurred, leading to higher surface roughness. The more severe the phenomenon, the more elemental segregation was observed. The pattern of the balling formation corresponded to the pattern of the oxide formation. Thus, surface quality served as an indicator of elemental segregation in PBF-ed material.

Another significant finding was regarding post-heat treatment considerations for PBF-ed H13, particularly concerning oxide particle growth during the heat treatment. Like conventional H13, in PBF-ed H13 increasing the tempering temperature and time increased the material's ductility due to the formation of tempered martensite and carbide precipitates; however, in PBF-ed H13, it also increased the size of oxide particles, which reduced the material's ductility. The optimal tempering temperature range was determined to be 500-550°C. Lastly, an annealing treatment prior to tempering was recommended to reduce internal stresses incurred during the PBF process before the tempering treatment.

This thesis offers a comprehensive exploration of the complex relationships between the PBF process, microstructure, and properties of H13 steel. Valuable insights are provided for the improvement and optimization of materials used in injection mold manufacturing. The discovery of mesoscopic elemental segregation constitutes a unique contribution, paving the way for future research and advancements in additive manufacturing and materials science.

Keywords: PBF, SLM, H13 Tool Steel, Keyhole porosity, Gas porosity, Annealing treatment, Tempering treatment, Oxidation, Elemental alloy segregation

TABLE DES MATIÈRES

LISTE DES TABLEAUX

LISTE DES FIGURES

LISTE DES ABRÉVIATIONS, DES SIGLES ET DES ACRONYMES

SLM	Fusion Sélective au Laser
SLM-ed	Fabriqué par Fusion Laser Sélective
PBF	Fusion sur Lit De Poudre
PBF-ed	Fabriqué par Fusion sur Lit De Poudre
TCC	Canal de Refroidissement Traditionnel
CCC	Canal de Refroidissement Conformal
AM	Fabrication additive
AM-ed	Fabriqué par Fabrication additive
LENS	Forme de Filet D'ingénierie Laser
ASTM	American Society for Testing and Materials
XRD	Diffraction des Rayons X
SEM	Microscope électronique à balayage
OM	Microscope optique
EBSD	Diffraction D’électrons rétrodiffusés
HIP	Pressage isostatique à chaud

LISTE DES SYMBOLES ET UNITÉS

Alpha-Fe	Fer alpha
Ar	Argon
C	Carbone
C°	Degrés Celsius
Cr	Chrome
d	Diamètre du spot
E_a	Valeur de construction de chaleur
E	Module d'élasticité
ε	Facteur d'accumulation de chaleur de multipiste
Fe	Fer
Fe_3C	Carbure de fer
GPa	Gigapascal
h	Dureté
H	Espacement des hachures
HV_{200}	Micro-dureté Vickers avec une charge de 200 g
J	Joule
$M_{23}C_6$	Carbure $M_{23}C_6$
M_3C	Carbure M_3C
M_7C_3	Carbure M_7C_3
MC	Carbure MC
mm	Millimètre
mm^3	Millimètre cube
MPa	Mégapascal
Mn	Manganèse

Mo	Molybdène
P	Puissance laser
ψ_3	Entrée d'énergie
S	Seconde
Si	Silicium
t	Épaisseur de couche de poudre
UTS	Résistance à la rupture
V	Vitesse de balayage
V	Vanadium
σ	Résistance à la traction ultime
σ_y	Limite élastique
e_f	Allongement à la rupture
wt. %	Pourcentage de masse
VED	Densité D'énergie Volumétrique
W	watt
µm	Micromètre

INTRODUCTION GÉNÉRALE

0.1. CONTEXTE GÉNÉRAL

Le moulage par injection, né à la fin du XIXe siècle, a révolutionné la fabrication grâce à sa capacité à produire en masse des pièces plastiques complexes. Développé initialement pour les billes de billard, il s'est rapidement étendu à diverses industries. Tout au long du XXe siècle, les avancées dans les matériaux, les machines et les techniques ont propulsé son évolution. Aujourd'hui, le moulage par injection est un pilier de la fabrication moderne, permettant la production rentable de composants plastiques complexes à grande échelle. Un moule d'injection, composé de diverses pièces, façonne le plastique fondu en une forme distincte. La Figure 1 illustre les composants du moule, y compris la pièce moulée (Figure 1-a en rouge), le noyau/la cavité du moule (Figure 1-b) et les canaux de refroidissement (Figure 1-a en bleu). Le processus de moulage comprend quatre étapes : le serrage du noyau du moule contre la cavité du moule pour former l'espace du produit, l'injection remplit l'espace avec du plastique fondu, le refroidissement se produit avec un agent de refroidissement circulant dans les canaux, et l'éjection libère le produit à l'aide d'une broche d'éjection [1]. La phase de refroidissement constitue 70 % du cycle de moulage par injection (Figure 1-c). Un système de refroidissement bien conçu accélère cette étape et améliore la productivité, tout en renforçant la résistance à la fatigue thermique du noyau et de la cavité en réduisant le gradient thermique [2].

Les canaux de refroidissement traditionnels (TCC), historiquement mis en œuvre à travers des méthodes telles que le perçage, présentent souvent des conceptions bien établies (Figure 1-c). Cependant, les TCC, avec leurs lignes droites, offrent une couverture partielle de la géométrie de la cavité, entraînant des problèmes tels qu'un refroidissement inégal, des temps de cycle accrus, des déformations et une qualité de produit sous-optimale, notamment

dans les géométries complexes. Les canaux de refroidissement conformes (CCC) émergent comme une solution innovante, offrant une gestion thermique nuancée pour des applications de moulage complexes [2, 3].

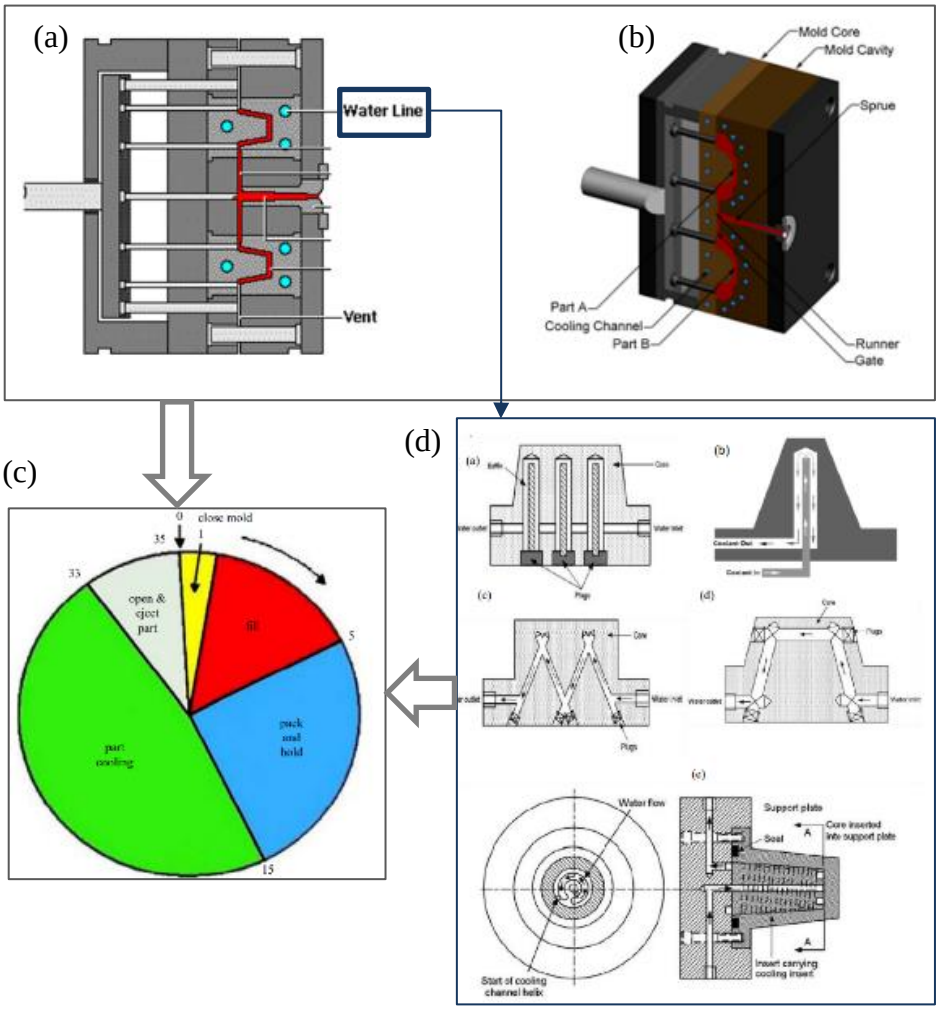

Figure 1. Schémas des composants d'un moule d'injection (a), (b) [4], (c) temps de cycle dans le moulage par injection [5], et (d) différents designs de TCC[2]

Un CCC est un passage qui suit la forme du noyau ou de la cavité du moule, facilitant un refroidissement rapide et uniforme dans les processus de moulage par injection ou de moulage par soufflage. La Figure 2 présente des schémas d'un CCC, le comparant avec un TCC utilisé dans un produit spécifique. De nombreuses études numériques et expérimentales sur différents designs de CCC ont été menées pour démontrer leur capacité à réduire le temps de refroidissement. Gerald R. Berger et al. [6] démontrent une réduction de 10 secondes dans

le cycle de moulage avec CCC. Kuo et al. [7] réalisent une impressionnante réduction de 93 % du temps de cycle, tandis que Chil-Chyuan Kuo et al. [8] démontrent une augmentation de 33,33 % de l'efficacité de refroidissement. Hong-Seok Park et al. [9] réalisent une remarquable réduction de 50 % de la phase de refroidissement. Jorge Manuel et al. [10] intègrent efficacement des systèmes de refroidissement en forme de treillis, améliorant l'efficacité des échanges thermiques. Chaolin Tan et al. [11] obtiennent une réduction de plus de 20 % du temps de refroidissement avec un CCC en forme de ressort autoportant pour un produit de forme de gobelet simple. Antonio Gruber et al. [12] illustrent une augmentation de 1,12 fois de la production annuelle grâce à la mise en œuvre optimisée de CCC dans une étude de cas spécifique. Kuo et al. [13] rapportent en outre une économie de 89,92 % du temps de refroidissement grâce à CCC.

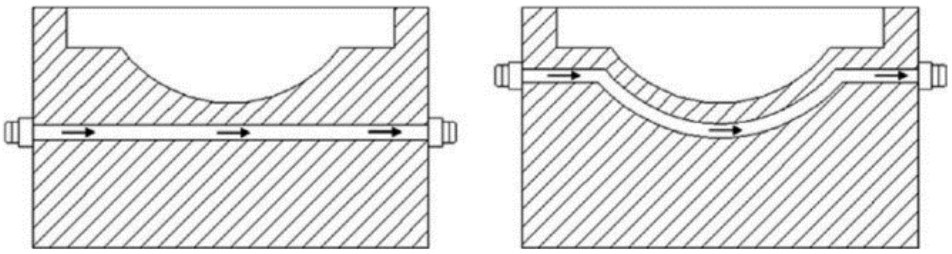

Figure 2. Schémas d'un (a) TCC et d'un (b) CCC

Les CCC représentent une approche sophistiquée pour améliorer la gestion thermique dans les moules d'injection, mais leurs conceptions complexes posent des défis pour les techniques de fabrication traditionnelles. La Fabrication additive (AM) émerge comme la solution idéale pour produire des CCC en raison de ses capacités uniques [14]. L'AM englobe diverses catégories, notamment l'extrusion de matériau, la photopolymérisation en cuve, la projection de matériau, la projection de liant, la lamination de feuilles, le dépôt d'énergie dirigée et la fusion de lit de poudre [15]. Le principe sous-jacent des méthodes d'AM implique la construction couche par couche d'un objet tridimensionnel à partir d'un modèle numérique. Contrairement aux méthodes traditionnelles soustractives, où le matériau est enlevé, l'AM construit la structure de manière incrémentielle [16]. Cette approche couche par couche et permet la génération de géométries avec précision et complexité, une exigence cruciale pour

les CCC intégrés dans un moule d'injection. Parmi les méthodes d'AM, la Fusion de Lit de Poudre (PBF) se distingue par sa capacité à produire des pièces métalliques. La Figure 3 montre un schéma du processus de PBF où une fine couche de poudre métallique est répartie uniformément sur une plate-forme de construction ; généralement, avec une épaisseur de couche de 20 µm à 100 µm. Un laser haute puissance, allant de 20 W à 1 kW, fait fondre ou solidifie la poudre selon le motif de section transversale du modèle numérique. Une fois qu'une couche est terminée, la plate-forme de construction descend et le racleur nivelle une nouvelle couche de poudre sur la précédente. Des structures de support, sous forme de treillis, sont également fabriquées pour soutenir la pièce pendant la fabrication, afin de prévenir toute déformation. Après la fabrication, ces structures de support sont retirées. Le processus se répète, couche par couche, jusqu'à ce que l'objet tridimensionnel entier soit formé. Le processus se déroule dans une chambre fermée avec une atmosphère de gaz inerte pour minimiser la teneur en oxygène et prévenir les interactions indésirables avec la poudre métallique [17, 18]. La capacité de la PBF à atteindre une grande précision et des détails complexes la rend particulièrement applicable à la fabrication de CCC pour les moules d'injection.

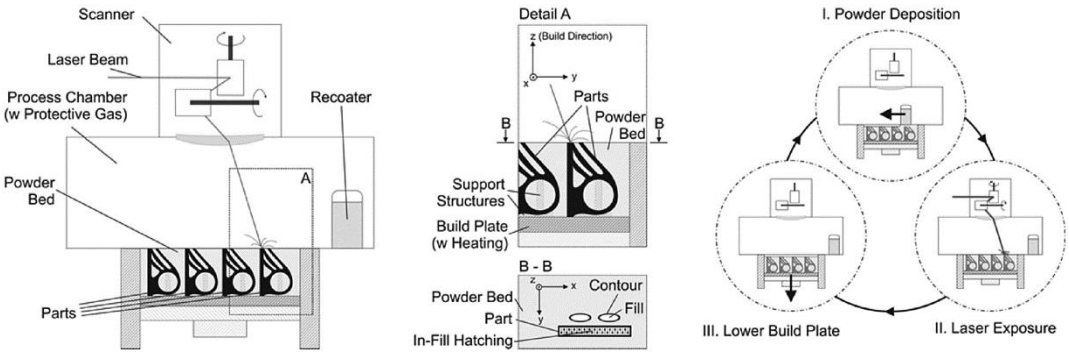

Figure 3. Schéma de la PBF

L’acier H13, avec une teneur en carbone variant de 0,32 % à 0,45 %, appartient au groupe des aciers pour outils de travail à chaud, ce qui le rend adapté aux applications nécessitant un moulage à haute température. Sa composition comprend du silicium, du chrome, du molybdène, du tungstène et du vanadium, contribuant à une excellente résistance

à l'usure, à la fatigue thermique, une bonne conductivité thermique, une dureté élevée, et une résistance mécanique élevée tout en conservant la ductilité appréciable. Grâce à sa combinaison supérieure de propriétés métallurgiques et mécaniques, l'acier H13 est largement utilisé dans l'industrie du moulage. Il est idéal pour résister aux conditions difficiles des processus de moulage à haute température et garantir des performances durables dans les applications de moulage, notamment le moulage sous pression, le moulage par injection et le forgeage à chaud[19, 20].

L’acier H13 produit par PBF présente des défauts, certains étant courants dans divers alliages d'acier. Les porosités, un problème fréquent, résultent soit d'une énergie d'entrée excessive, soit d'une énergie insuffisante. Les chercheurs les catégorisent en pores de gaz (gaz piégés), en défauts de manque de fusion (LOF) (vides avec des particules de poudre non fondues), et en pores de trou de serrure (causés par une densité d'énergie excessive) [21, 22]. Le "balling", un autre défaut, se produit lorsque le faisceau laser fait fondre les particules de poudre, les amenant à former une sphère de métal liquide pendant le processus de balayage [23]. Les contraintes résiduelles, résultant des fluctuations thermiques lors des cycles de chauffage et de refroidissement rapides, peuvent entraîner une distorsion des pièces, des fissures et un délaminage, impactant la précision dimensionnelle et la résistance mécanique [24]. Ces défauts pourraient être éliminés par la manipulation des paramètres du procédé. De plus, dans le H13 obtenu par PBF, en raison du refroidissement rapide, les grains d'austénite fins, avant de croître significativement, se transforment en martensite fine. Ce processus, facilité par la teneur en carbone appropriée dans le H13, conduit à la formation d'une structure presque entièrement martensitique caractérisée par une dureté de surface élevée [25]. Cette transformation induit une augmentation de volume de 4 %, contribuant à des contraintes internes qui peuvent entraîner la formation de fissures pendant le processus de fabrication. Elle crée également des contraintes résiduelles de compression à la surface [26]. Des études indiquent que les paramètres du procédé, y compris la puissance laser, la vitesse de balayage, l'épaisseur de la couche et la température de préchauffage, influencent significativement ces facteurs et les propriétés mécaniques globales. Le matériau construit se caractérise par une

grande fragilité, avec une résistance ultime comprise entre 1524 et 1909 MPa, un allongement variant de 1 % à 12 % et une dureté comprise dans la plage de 549 HV à 894 HV [7, 26-30].

Étant donné la fragilité du matériau tel qu'il est construit et la faible capacité d'allongement, le post-traitement devient impératif dans la fabrication additive de H13 [31]. Cependant, en raison des différences de microstructure, le traitement thermique commun du H13 forgé doit être adapté pour le H13 produit par PBF.

Dans le cas du H13 forgé, la recristallisation est un traitement important pour éliminer les contraintes, améliorer la structure, affiner le grain et réduire la dureté en vue d'opérations d'usinage ultérieures. Le traitement de revenu est appliqué au H13 après la trempe afin de minimiser la dureté excessive des pièces forgées en H13, éliminer les contraintes et augmenter la résilience à haute température. De plus, des traitements de surface tels que la nitruration au plasma, la sulfurisation-nitruration au plasma et la bromination ont été utilisés pour les moules fabriqués de manière conventionnelle [32, 33]. De plus, différents types de traitements de surface au laser ont été appliqués au H13, notamment la fusion de surface au laser (LSM) [34], le durcissement de surface au laser (LSH) [33], le glaçage de surface au laser (LSG) [35], et le rechargement au laser (LC) [36], afin d'augmenter la microdureté de surface et ainsi la résistance à la fatigue.

Les post-traitements pour le H13 produit par PBF comprennent divers traitements, y compris les traitements de surface, le pressage isostatique à chaud (HIP), la nitruration et le traitement en four.

Le traitement de surface dans ce cas vise à améliorer la finition de surface des produits. La haute rugosité de surface dans le matériau PBF-d est bien connue et attribuée aux particules de poudre adhérentes, qui sont partiellement fondues et adhèrent au matériau [37]. Cela nécessite une finition de surface, et le polissage de surface au laser (LSF) est la méthode préférée. Le LSF offre des avantages tels qu'un temps et des coûts de traitement réduits, l'absence de contraintes résiduelles sur la zone polie et l'adaptabilité à des formes complexes impossibles à réaliser avec d'autres méthodes. Le polissage macro-laser est conçu

pour une rugosité initiale plus élevée (60 s/cm^2 traitant la rugosité de 10 à 80 µm), tandis que le polissage micro-laser convient aux surfaces moins rugueuses (3,3 s/cm^2, traitant la rugosité de 0,5 à 5 µm). Dans les cas de haute rugosité, il est recommandé de procéder d'abord au macro-polissage suivi du micro-polissage [38-40]. Il y a eu quelques études sur le traitement de surface du H13 produit par PBF. M. Khalid et al. [41] qui ont mené une étude sur le polissage au laser pour le H13, examinant l'influence du chevauchement entre les pistes du faisceau laser sur la qualité de surface du matériau. Nüsseret et al. [42] ont examiné l'impact de la distribution d'intensité et de la durée de l'impulsion sur le H13 pendant le processus de micro-polissage.

Le processus HIP s'est révélé très efficace pour réduire le pourcentage de porosité et la contrainte ultime. En particulier, lorsqu'il est combiné avec le revenu, il est possible d'augmenter la dureté de 20 % et la ténacité de 61 % [43]. Le traitement HIP direct du matériau tel qu'il est construit pourrait augmenter le rendement et la résistance ultime de 3 % et 6 % respectivement [28, 30]. Malgré les effets positifs des autres traitements, la nitruration entraîne une réduction du rendement et de la résistance ultime de 7 % et 10 % respectivement [30]. Il est à noter que, bien que le traitement de recuit de relaxation des contraintes soit recommandé, pour le post-traitement HIP, le fait de sauter le recuit peut augmenter la dureté de 20 % et la ténacité à la rupture de 61 % [44].

En ce qui concerne le traitement en four, similaire au H13 forgé, les traitements courants du H13 produit par PBF sont la trempe suivie d’un revenu et le recuit de relaxation des contraintes. La trempe produit une grande quantité de carbures et d'austénite résiduelle, ce qui est une condition favorable pour le revenu. Le revenu transforme l'austénite résiduelle en cémentite et en ferrite et dissout la structure cellulaire dans la matrice pour former de la ferrite plate et précipiter le carbure sphérique, ce qui augmente la ténacité et rend le matériau plus souple [45]. Une étude de l'évolution des phases pendant ce traitement indique que le traitement de recuit ne modifie pas le pourcentage d'austénite résiduelle à une température inférieure à 620 °C. Le revenu réduit l'austénite résiduelle et forme des carbures de vanadium [46]. L'impact de différentes températures de revenu sur la micro-dureté montre que la dureté

maximale se produit à 550 °C, avec une réduction de la dureté observée à des températures inférieures ou supérieures à ce point [47, 48]. Le module de Young subit des changements mineurs de moins de 1 % entre 350 °C et 600 °C. À 650 °C, le module de Young augmente d'environ 3 % (de 317.87 GPa pour les échantillons tels qu'ils sont construits à 326.56 GPa pour le revenu à 650 °C) [47]. Pour le revenu à 600 °C, le seuil d'élasticité augmente de 81 % (de 818 MPa à 1483 MPa), la résistance maximale de 35 % (de 1430 MPa à 1938 MPa) et l'allongement de 1,3 fois. Le revenu à 700 °C réduit la résistance maximale de 25 %, avec une énorme augmentation de l'allongement de 3,5 fois l'échantillon construit [49].

0.2. PROBLÉMATIQUE

L'acier à outils de travail à chaud H13 est largement utilisé dans les applications de moulage par injection en raison de sa résistance exceptionnelle à la fatigue élevée et à la corrosion à des températures de travail élevées. Avec l'augmentation de l'utilisation des technologies AM pour la production de pièces métalliques, la mise en œuvre du H13 produit par PBF est considérée comme une avancée significative dans l'industrie du moulage.

La PBF du H13, en tant qu'acier à haute teneur en éléments d'alliage, présente des défis critiques qui se traduisent par des pièces fabriquées avec des propriétés mécaniques inférieures aux exigences de l'industrie. Ces défis découlent d'aspects inhérents du processus, mais peuvent être atténués grâce au contrôle des paramètres de traitement. Les paramètres clés incluent la puissance du laser, la vitesse du laser, l'épaisseur de la couche et l'espacement, encapsulés collectivement par la densité d'énergie volumique (VED), qui est l'énergie contenue dans un volume spécifique. Comprendre et optimiser ces paramètres est crucial pour obtenir les propriétés mécaniques désirées dans les pièces en H13 produites par PBF.

L'étude de l'effet de la densité d'énergie volumique (VED) sur la formation de la porosité est impérative pour comprendre la complexité des processus de fabrication additive par PBF. La présence de différents types de porosités, notamment en forme de trous de serrure, les pores de gaz et les défauts de manque de fusion, influe considérablement sur les

propriétés mécaniques des matériaux produits par PBF, conduisant à une densité relative inférieure à 100 %. Chaque type de porosité diminue la section transversale effective lorsqu'il est soumis à des charges cycliques ou statiques, réduisant ainsi la capacité de charge maximale du matériau. De nombreuses études ont exploré l'impact de la VED sur la densité relative, révélant que l'augmentation de la VED jusqu'à un seuil certain, généralement autour de 65 J/mm3, conduit à des matériaux avec une densité presque complète. Au-delà de ce seuil, cependant, aucune amélioration significative ne se produit, et des valeurs de VED excessivement élevées peuvent même diminuer la densité relative. Plus précisément, l'influence de la VED sur la formation du manque de fusion a été étudiée, mettant en évidence la nécessité de maintenir une valeur minimale pour éviter la fusion partielle de la poudre. Cependant, la relation entre la VED et la formation d'autres types de porosités, comme les trous de serrure et les pores de gaz, reste inexplorée en raison de la complexité inhérente du processus. La porosité de type trou de serrure se produit dans le soudage au laser lorsque l'intensité de la poudre dépasse un seuil, faisant passer le mode de soudage du mode de conduction au mode de trou de serrure. Par conséquent, bien que l'augmentation de la VED puisse atténuer le manque de fusion, elle peut également induire la porosité de type trou de serrure. Le mécanisme de formation de la porosité de gaz a été identifié, mais aucune étude n'a élucidé la corrélation entre la VED et la formation de la porosité de gaz. Par conséquent, élucider la relation complexe entre la VED et les différents types de formation de porosité est crucial pour optimiser les processus de fabrication additive. De plus, le manque d'exploration complète dans la littérature existante souligne le besoin urgent de recherches supplémentaires pour aborder cet aspect critique du H13 produit par PBF de manière efficace.

Concernant le H13 produit par PBF, la microstructure est non homogène. La littérature existante indique que la microstructure du H13 tel qu'il est construit se compose de structures cellulaires. Ces structures cellulaires présentent des formes arrondies avec une uniformité au sein des couches d'impression. Cependant, dans la direction de construction, en se déplaçant de la plaque de base à la dernière couche imprimée, ces structures cellulaires deviennent non uniformes, principalement orientées vers le flux de chaleur. Par conséquent, la microstructure du matériau varie considérablement en fonction de la direction de

l'échantillon, conduisant à des propriétés mécaniques dépendantes de la direction. La recherche indique également un gradient de contamination de phase de la plaque de base à la surface supérieure, avec une teneur maximale en martensite dans les dernières couches et une martensite réduite dans les couches initiales en raison de la décomposition de la martensite en austénite. La ségrégation élémentaire, une autre source d'inhomogénéité dans la microstructure, un phénomène bien connu dans les processus de soudage au laser, est également observée dans la PBF du H13. Bien que la littérature suggère que les parois cellulaires sont riches en éléments d'alliage, la ségrégation mésoscopique des éléments d'alliage dans chaque piste laser pendant la fusion et la solidification de la poudre n'a pas été largement discutée. Les études sur le soudage au laser du H13 ont établi la migration des éléments d'alliage vers les limites des pistes laser, les paramètres du traitement au laser ayant montré son influence sur les taux de ségrégation. Par exemple, une densité d'énergie laser dépassant 80 $^{J}/_{mm^2}$ a été montrée pour avoir un impact sévère sur la stabilité microstructurale. Par conséquent, explorer l'impact de la VED sur la ségrégation élémentaire du H13, qui contient une quantité considérable d'environ 8 % d'éléments d'alliage, est essentiel pour optimiser les processus de fabrication additive et contrôler l'homogénéité microstructurale, un aspect qui n'a pas encore été abordé.

Le facteur crucial dans la PBF du H13 est l'étude de l'effet du préchauffage et de la stratégie d'impression. Cette préoccupation découle de plusieurs facteurs. Un problème notable est le gradient dans le champ de contraintes résiduelles à l'intérieur du matériau. Initialement, et dans les couches intermédiaires, il existe des contraintes de traction variables qui se transforment ensuite en une fraction volumique élevée de contraintes résiduelles compressives dans les dernières couches imprimées. Les contraintes résiduelles compressives élevées, liées à la formation de martensite se produisant à des vitesses de refroidissement rapides, constituent un facteur qui contribue à la susceptibilité aux fissures pendant le processus de fabrication. Les contraintes résiduelles de traction dans les couches initiales et intermédiaires sont causées par la transformation inverse de la martensite en austénite. Des études existantes indiquent que l'historique thermique pendant la fabrication,

influencé par des paramètres de traitement tels que la puissance du laser, la vitesse et l'espacement, affecte ce champ de contraintes résiduelles et, par conséquent, la résistance mécanique. Cependant, l'impact de deux autres paramètres critiques, la stratégie d'impression et la température de préchauffage, sur ce sujet, reste inexploré. La stratégie d'impression a été identifiée comme un contributeur significatif aux contraintes résiduelles dans la PBF d'autres métaux, tandis que la température de préchauffage, en maintenant la température au-dessus de la transformation de la martensite tout au long du processus, aide à réduire les contraintes résiduelles. Étudier l'effet de ces paramètres sur la résistance mécanique du H13 est essentiel pour optimiser le processus de PBF et atténuer les problèmes liés aux fortes contraintes résiduelles, améliorant ainsi la qualité et la fiabilité des composants fabriqués.

La recherche s'articule autour de la compréhension de l'influence de la densité d'énergie volumique (VED) sur la formation de "balling" dans la PBF du H13, ce qui est crucial pour plusieurs raisons. La formation de "balling" pose un problème important dans la PBF des aciers, parce que le processus peut échouer dans des cas graves de "balling". Lorsque ce dernier se produit de manière excessive, les sphères résultantes peuvent dépasser l'épaisseur définie de la couche dans la machine, endommageant potentiellement le racleur et perturbant le bon déroulement du processus. Même des cas plus légers de "balling" peuvent introduire des porosités pendant le traitement. De plus, la formation de "balling" à la fin du processus et dans la dernière couche imprimée peut entraîner des finitions de surface irrégulières et une qualité de rugosité inférieure, impactant la stabilité dimensionnelle et la précision du processus de fabrication. La formation de "balling" est intimement liée à la dynamique du transfert de chaleur pendant le processus de fusion, qui dépend à son tour de la VED. Bien que la formation de "balling" soit bien étudiée dans le domaine du soudage au laser, sa présence dans la PBF du H13 a été signalée, mais l'effet de la VED sur ce phénomène est rarement documenté. Étant donné le rôle critique de la formation de "balling" dans la stabilité dimensionnelle et la précision de la PBF, comprendre l'impact de la VED sur cet aspect est primordial pour aborder l'optimisation des processus et le contrôle de la qualité.

Dans l'ensemble, explorer l'impact des paramètres de traitement sur divers aspects tels que l'évolution de la porosité, l'homogénéité microstructurale, la ségrégation élémentaire et la formation de "balling" dans l'acier H13 produit par PBF présente une lacune significative dans la recherche actuelle. Comprendre ces effets est impératif pour faire progresser le domaine et optimiser le processus de fabrication.

Malgré les efforts pour optimiser les paramètres de traitement, la persistance de la fragilité du matériau souligne l'importance cruciale de l'étude du post-traitement, en particulier du traitement thermique. La caractéristique de refroidissement rapide de la fabrication conduit à une accumulation excessive de martensite, résultant en une durabilité insuffisante sous des charges cycliques. Pour atténuer ce problème, des traitements en four tels que le recuit et le revenu sont recommandés. Le recuit, impliquant un chauffage contrôlé et un refroidissement progressif, conduit à de légères modifications de la structure cellulaire, améliorant ainsi partiellement l'allongement et influençant le comportement de déformation plastique du matériau. En revanche, les processus de trempe et de revenu facilitent la transformation de la microstructure en martensite revenue, améliorant significativement l'allongement et les propriétés de déformation plastique. Cependant, la littérature existante manque d'exploration complète des effets de ces traitements sur les défauts de fabrication tels que la formation d'oxydes due à la ségrégation élémentaire. De plus, il existe un manque d'études complètes sur la sensibilité de ces traitements et de leurs paramètres sur les propriétés mécaniques du H13 produit par PBF. Comprendre l'effet de ces deux traitements et de leurs paramètres, y compris le temps et la température, sur la microstructure et les propriétés mécaniques du H13 produit par PBF est crucial pour acquérir des connaissances sur le comportement du matériau et prédire ses propriétés mécaniques.

Comprendre et relever ces défis est nécessaire pour faire progresser le domaine de l'acier H13 produit par PBF, ouvrant ainsi la voie à des processus de fabrication améliorés et à des performances matérielles accrues.

0.3. OBJECTIFS

L'objectif de cette thèse est de fournir une meilleure compréhension et un meilleur contrôle des propriétés mécaniques et physiques de l'acier à outils H13 fabriqué par PBF avec et sans post-traitement thermique, en se basant sur divers paramètres influents. Pour atteindre ces objectifs, il est nécessaire de passer par des sous-objectifs correspondant à des étapes spécifiques du projet de recherche.

1. Le premier objectif est d'examiner en profondeur la revue la littérature pour comprendre la nécessité d'étudier le processus PBF du H13 en considérant la faisabilité d'augmenter la productivité des moules avec des canaux de refroidissement conformes. En ce sens, il est question d'étudier l'effet de la microstructure et des caractéristiques mécaniques du H13 traité par PBF. En outre, il est important d'examiner l'effet des paramètres de traitement sur la densité, la microstructure et le comportement mécanique. Enfin, on procède à examiner les traitements postérieurs possibles pour améliorer les propriétés mécaniques du H13 selon les besoins.
2. Le deuxième objectif consiste à optimiser les paramètres du processus de PBF. Cela impliquera une investigation systématique des variables telles que la puissance du laser, la vitesse du laser, l'espacement, la température de préchauffage et la stratégie d'impression. L'objectif est d'identifier la combinaison optimale de ces paramètres qui conduit à la production de pièces en H13 avec une homogénéité microstructurale améliorée et l'élimination des porosités et de la formation de "balling". Cette optimisation devrait contribuer à l'amélioration des propriétés mécaniques.
3. Le troisième objectif consiste à étudier l'impact des processus de post-traitement, en comparant spécifiquement l'influence de divers traitements tels que le recuit et le revenu sur la microstructure et les propriétés mécaniques du matériau. L'étude explorera également les effets du temps et de la température pendant ces traitements afin d'évaluer la sensibilité des propriétés mécaniques

du matériau à ces paramètres. En fin de compte, l'objectif est de proposer un traitement thermique adapté pour le H13 produit par PBF.

En accomplissant ces objectifs, ce travail de recherche peut contribuer à l'industrie manufacturière en proposant une méthode qui permet de produire des pièces mécaniques en acier H13 qui résistent aux conditions de travail exigeantes; d'une façon comparable à l'acier H13 produit par les méthodes conventionnelles.

0.4. MÉTHODOLOGIE

Pour répondre aux objectifs principaux de l'étude, une méthodologie méticuleusement conçue, composée de trois étapes fondamentales a été élaborée. Ces étapes ont été soigneusement élaborées pour garantir une approche complète visant à atteindre les objectifs de recherche et à éclairer les aspects clés de l'enquête.

La première phase de l'étude consiste en une revue approfondie de la littérature existante sur le procédé de fusion sélective par laser (SLM), utilisé dans cette étude pour le PBF. Cette revue englobe un large éventail d'études explorant le potentiel du H13 produit par PBF dans l'industrie, ainsi que les effets de divers paramètres de traitement sur des aspects critiques tels que la densité relative, l'évolution microstructurale et les propriétés mécaniques du H13 produit par SLM. De plus, un examen approfondi de la recherche portant sur différents post-traitements, y compris le traitement de surface et le traitement thermique, et leurs impacts sur le comportement mécanique du H13 produit par SLM est entrepris. Grâce à cette revue approfondie, l'objectif principal est d'identifier méticuleusement les obstacles existants et les lacunes de recherche dans ce domaine, fournissant ainsi des perspectives inestimables pour orienter les futures recherches dans une direction plus éclairée.

Dans la deuxième phase de la méthodologie, le deuxième objectif, visant à comprendre l'impact des paramètres du processus de fusion sélective par laser (SLM) sur les performances de l'acier à outils H13, a été abordé. Cela a impliqué la sélection de cinq paramètres cruciaux - puissance du laser, vitesse de balayage, espacement des lignes de

balayage, température de préchauffage et stratégie d'impression - en fonction de leur importance dans la littérature existante. Pour optimiser ces paramètres, une investigation complète a été menée, explorant initialement une large gamme de valeurs pour la puissance du laser, l'espacement des lignes de balayage et la vitesse de balayage en utilisant la méthode de conception Taguchi (3 niveaux avec 9 conceptions orthogonales). Ensuite, ces plages ont été réduites et une autre conception Taguchi avec 3 niveaux a été menée. Au cours de cette phase, les effets de ces paramètres de traitement sur la morphologie de la porosité, la microstructure, la ségrégation élémentaire et la résistance mécanique ont été analysés. Les paramètres de traitement optimisés obtenus ont ensuite été utilisés pour les étapes suivantes. Dans les phases suivantes, une température de préchauffage de 150 degrés Celsius a été appliquée, entraînant une amélioration de la résistance mécanique. Une stratégie d'impression améliorée a ensuite été utilisée pour renforcer davantage la résistance mécanique. Tout au long de ces phases, une batterie de tests, comprenant la microdureté, la diffraction des rayons X (DRX), les essais de traction uniaxiale, la microscopie électronique à balayage (MEB) et des observations en microscopie optique, a été réalisée pour étudier les effets des paramètres de traitement. Au total, 21 configurations expérimentales ont été conçues pour explorer l'influence de ces paramètres sur la microstructure, les propriétés mécaniques et la formation d'oxydes. Toutes les expériences ont été menées dans les laboratoires du Département de mathématiques, d'informatique et de génie de l'UQAR.

Dans la troisième phase de l'étude, le troisième objectif, qui visait à adapter un traitement thermique pour l'acier à outils H13 produit par SLM, a été abordé. L'accent a été mis sur le développement d'un protocole de traitement thermique personnalisé spécifiquement pour l'acier à outils H13 fabriqué par le processus de PBF. Cette phase a impliqué la conception de 14 ensembles différents d'expériences. Un ensemble comprenait des échantillons traités avec un double revenu direct, dans le but de comprendre la nécessité d'une pré-trempe même lorsqu'il s'agit d'une structure presque entièrement martensitique. Six ensembles ont étudié les effets de la variation des paramètres de temps et de température, allant de 500°C à 750°C et de 2 à 6 heures de revenu. De plus, cinq ensembles ont examiné les paramètres de temps et de température du recuit, allant de 400°C à 650°C et de 2 à 6

heures de durée. Deux ensembles ont été conçus pour étudier l'effet du recuit avant le revenu à des températures de recuit de 500°C et 600°C, respectivement. Pour chaque ensemble, des observations microstructurales ont été réalisées à l'aide de la microscopie électronique à balayage (MEB) et de la microscopie optique, et une analyse des particules d'oxyde a été réalisée à l'aide de méthodes d'analyse d'images. Des tests de micro-dureté, ainsi que des essais de traction uni-axiale, ont été réalisés, les données analysées comprenant l'allongement, la limite d'élasticité, la résistance à la traction et le module d'élasticité. L'analyse de la fractographie a également été effectuée avec la microscopie électronique à balayage (MEB). La sensibilité de chaque résultat aux variations de temps et de température a été soigneusement examinée. Cette analyse méticuleuse a abouti à la proposition d'un protocole de traitement thermique finement réglé et adapté, optimisé spécifiquement pour l'acier à outils H13 produit par PBF. Les exigences spécifiques et les défis associés au processus de fabrication additive ont été pris en compte par ce protocole, offrant ainsi une solution complète pour améliorer les propriétés et les performances des matériaux.

0.5. ORGANISATION DE LA THÈSE

La thèse est organisée en une introduction générale, chapitre 1, chapitre 2, chapitre 3, et conclusion générale. L'introduction générale représente un aperçu global à la thèse et est rédigée en français. Le chapitre 1, le chapitre 2 et le chapitre 3 sont chacun dédiés à la réalisation d'objectifs spécifiques 1, 2 et 3 respectivement, et sont rédigés en anglais.

Dans le chapitre 1, l'article de revue de littérature explore l'application complexe des processus de fabrication additive dans l'industrie du moule d'injection, en mettant particulièrement l'accent sur l'état de l'art dans la conception des canaux de refroidissement. Ensuite, un examen détaillé de la microstructure et des propriétés mécaniques de l'acier H13 fabriqué par ajout de matière, adapté à cette application spécifique, est l'objectif principal des sections suivantes.

Dans le chapitre 2, l'accent est mis sur une exploration approfondie des impacts des paramètres du processus PBF sur les performances de l'acier à outils H13. L'investigation

vise à découvrir l'influence des paramètres de traitement sur la ségrégation élémentaire, la formation d'oxydes, l'évolution de la porosité, la micro-dureté et la résistance mécanique.

Dans le chapitre 3, l'attention est portée sur un examen détaillé de l'impact des paramètres de recuit et de revenu sur la microstructure, la formation d'oxydes et la résistance mécanique. Cette étude explore également les effets combinés des deux traitements, fournissant des aperçus complets de leur influence sur les propriétés du matériau.

Enfin, dans la conclusion générale, une synthèse globale de la thèse est présentée en français.

CHAPITRE 1
REVUE EXHAUSTIVE DE L'ACIER A OUTIL H13 FABRIQUE PAR FABRICATION ADDITIVE POUR L'INDUSTRIE DES MOULES D'INJECTION : APPLICATIONS, CONCEPTIONS, MICROSTRUCTURE ET PROPRIETES MECANIQUES

Narges Omidi[1], Pedram Farhadipour[1], Lamya Baali[1], Karim Bensalem[1], Noureddine Barka[1],

Mohammad Jahazi[2]

[1] University of Quebec at Rimouski, Department of Mathematics, Computer Science and Engineering, Quebec, Canada

[2] École de technologie supérieure (ÉTS), Department of Mechanical Engineering, Québec, Canada

RÉSUMÉ EN FRANÇAIS DU PREMIER ARTICLE

La fabrication additive (AM) s'est révélée une technologie prometteuse pour les applications industrielles critiques nécessitant des propriétés mécaniques de haute performance. Contrairement aux méthodes de soustraction, l'AM offre aux industriels la flexibilité de produire des géométries complexes, ce qui le rend particulièrement adapté aux applications complexes. Une telle application est la fabrication de moules d'injection avec des canaux de refroidissement conformes complexes (CCC), qui permettent une extraction de chaleur efficace et améliorent la durée de vie en fatigue du moule en acier. Cet article de revue examine les études récentes sur les moules d'injection fabriqués à l'aide de techniques AM, organisées en trois sections. La première section explore la recherche sur la conception de CCC visant à optimiser la distribution de la température dans le moule. La deuxième section fournit une analyse détaillée de l'acier H13, un matériau communément utilisé dans la fabrication de moules, en se concentrant sur sa microstructure et ses propriétés mécaniques lorsqu'il est produit à l'aide de la technologie AM. Enfin, la troisième section passe en revue

les traitements post-traitement visant à améliorer davantage les propriétés mécaniques des moules d'injection fabriqués par AM.

Cet article, intitulé « *A Comprehensive Review of Additively Manufactured H13 Tool Steel Applicable in the Injection Mold Industry: Applications, Designs, Microstructure, Mechanical Properties*», a été accepté pour publication dans sa version finale en 2023 par les éditeurs du Journal de la Société des minéraux, métaux et matériaux (JOM). En tant que premier auteur, j'ai apporté une contribution significative à la revue de la littérature, à la majorité de la revue de la littérature et j'ai rédigé la plupart des sections. Pedram Farhadipour, Lamya Baali et Karim Bensalem, respectivement deuxième, troisième et quatrième auteur, ont contribué à la révision de l'article et à la revue de la littérature sur l'effet environnemental. Le professeur Noureddine Barka, le cinquième auteur, a fourni l'idée originale, a aidé à la revue de la littérature, au développement de la méthode et à la révision de l'article. Le professeur Mohammad Jahazi, le sixième auteur, a également contribué à la révision de l'article.

1.1.A Comprehensive Review of Additively Manufactured H13 Tool Steel Applicable in the Injection Mold Industry: Applications, Designs, Microstructure, Mechanical Properties

1.1.1 Abstract

Additive manufacturing (AM) has emerged as a promising technology for critical industrial applications requiring high-performance mechanical properties. Unlike subtractive methods, AM offers manufacturers flexibility in producing intricate geometries, making it particularly suitable for complex applications. One such application is the fabrication of injection molds with complex conformal cooling channels (CCCs), which enable efficient heat extraction and enhance the fatigue life of the steel mold. This review paper examines recent studies on injection molds manufactured using AM techniques, organized into three sections. The first section explores research on the design of CCCs aimed at optimizing temperature distribution within the mold. The second section provides a detailed analysis of H13 steel, a common material used in mold manufacturing, focusing on its microstructure and mechanical properties when produced using AM technology. Finally, the third section reviews post-processing treatments aimed at further enhancing the mechanical properties of AM-manufactured injection molds.

1.1.2 Introduction

Injection molding is a widely used manufacturing method for producing high- or medium-volume components. The process involves melting the starting material and injecting it into a mold cavity, where it solidifies to form the desired product. After cooling, the product is ejected using equipment such as ejector pins [50, 51]. Thermal fatigue, resulting from repeated thermal cycles during production, is a common cause of mold failure. To address this issue, various design strategies, such as baffle systems and specialized cooling techniques, are employed to enhance thermal conductivity and reduce high-temperature points within the mold. Additionally, optimizing cooling times is essential, as it can significantly impact production efficiency and costs, with cooling time typically

accounting for 50-70% of the injection process duration. Effective thermal management is therefore crucial for maximizing mold lifespan, productivity, and cost-effectiveness [2, 52].

AM encompasses a range of manufacturing methods wherein the final product is created by progressively adding layers until the desired part is formed. This technology offers significant advantages over subtractive methods, particularly when dealing with intricate geometries like spiral or profiled holes. AM could benefit the plastics and aluminium die-casting industries in two ways. First, injection molds may be replaced by AM, leading to plastic parts being directly printed using the technology[53]. According to a comparative study by Achillasa et al. [54], suggests that for medium- to high-volume production, AM technologies often outperform conventional injection molds, except for specific complex geometries. Secondly, AM technology facilitates the production of more durable molds, thereby enhancing overall productivity. This is achieved through the utilization of novel cooling systems within the mold, made possible by AM's capabilities. Examples include lattice structures for improved thermal conductivity and curved cooling channels strategically positioned at high-temperature zones within the mold. These innovative cooling solutions, such as CCCs, surpass traditional cooling methods in terms of thermal management effectiveness.

This paper aims to provide a comprehensive review of research conducted thus far to enhance mold productivity using AM technology. It is structured into three main sections. The first section examines modified molds designed to improve thermal conductivity through innovative additive manufacturing methods, including the integration of cellular structures and CCCs. The second section addresses the challenges encountered in manufacturing such innovative designs using powder-based additive manufacturing methods, with a specific focus on issues related to the mechanical properties of AM-ed H13 steel. Lastly, the third section explores potential post-treatments aimed at achieving the desired mechanical properties of as-built materials

1.1.3 Exploring “bio-inspired” designs and “mold-conforming” designs for improved cooling

Injection molds can benefit from AM techniques to achieve optimal thermal distributions using innovative molds or innovative cooling channels. Innovative molds often incorporate cellular structures, inspired by natural designs, to replace bulk mold components. These bio-inspired designs, also known as generated designs or bioinspired sustainable products, draw inspiration from nature's efficient structures, such as molecular lattice or honeycomb patterns, renowned for their strength-to-weight ratio and stiffness [55-57]. Recent research indicates that incorporating cellular or lattice structures within injection molds enhances heat conductivity while maintaining sufficient strength for molding applications. These structures also exhibit excellent energy absorption properties under external loads, contributing to improved mold durability and fatigue life, while reducing material usage due to lighter mold weights [14, 58, 59].

Innovative cooling channels so-called CCCs further enhance thermal management by maintaining consistent distances between the mold cavity and the cooling channels. Many designs have been proposed for CCCs, some simply following the mold cavity contours while others incorporate bio-inspired designs. These designs aim to optimize heat transfer and improve cooling efficiency by conforming closely to the mold geometry. Additionally, CCCs can be combined with traditional cooling channels (TCCs). These hybrid systems leverage both conformal and traditional cooling channels to achieve desired thermal profiles. The following sections explore the implementation of bio-inspired molds and CCCs, drawn from the literature, to achieve improved cooling efficiency.

1.1.3.1 Bio-inspired cellular structure as alternatives to traditional mold components

To enhance heat conduction in injection molds, cellular structures can be applied either throughout the entire mold or selectively to specific areas. Malca et al. [60] used the selective laser melting (SLM) method to create two hexagonal and cub-octahedral lattice structures (Figure 4-a, and Figure 4-b) and showed that the hexagonal cellular structure has a higher

mechanical strength, while the cub-octahedral cellular structure outperforms it in thermal conductivity. In other studies, thermomechanical topology has been used to create partial, non-repeatable cellular structures and saved an existing injection mold from 10% to 30% of material while keeping the von Mises stress and surface temperature within safe limits[61]. Vegard et al. [14] propose similar structures with different design logic. By introducing the lattice structure inside the molds around cooling channels (Figure 4-c), the proposed structure aims to improve the fatigue strength of the mold. The authors believe that the cellular structure prevents initial cracks from propagating.

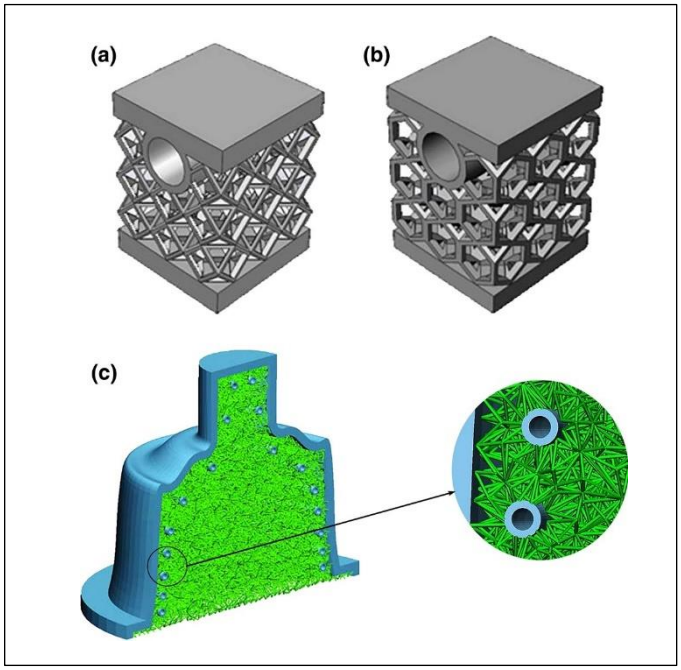

Figure 4. Proposed cellular structures: (a) cub-octahedral, and (b) hexagonal[60] (Adapted with permission from reference [61]), and (c) cellular structure around conventional cooling channels (Adapted with permission from reference [14])

1.1.3.2 Bio-inspired CCC designs for injection molds

Compared to cellular structures, CCCs have received more extensive research attention. Various CCC designs have emerged, ranging from nature-inspired concepts to those generated through optimization methods. One notable study proposed a fast-cooling

system inspired by human body vessels to enhance cooling efficiency in critical points of automotive oil filter housings (Figure 5). When compared to conventional copper pins (Figure 5-a) and even CCCs (Figure 5-b), the nature-inspired design (Figure 5-c) significantly reduces temperatures in hotspots. However, a challenge arises with small-diameter channels, as they are highly susceptible to blockage from impurities in the cooling flow [6]. Another study utilized genetic algorithms to optimize CCC designs for molds containing cavities with concave, slender details, internal turrets, and housings (Figure 5-d). The resulting design drew inspiration from honeycomb structures for lower and upper half of the mold respectively Figure 5-e and Figure 5-f. Experimental results across various real cases demonstrated reduced cooling times in deep parts with lattice cooling channels. Nonetheless, the study did not delve into the mold's fatigue strength, warranting further investigation[10].

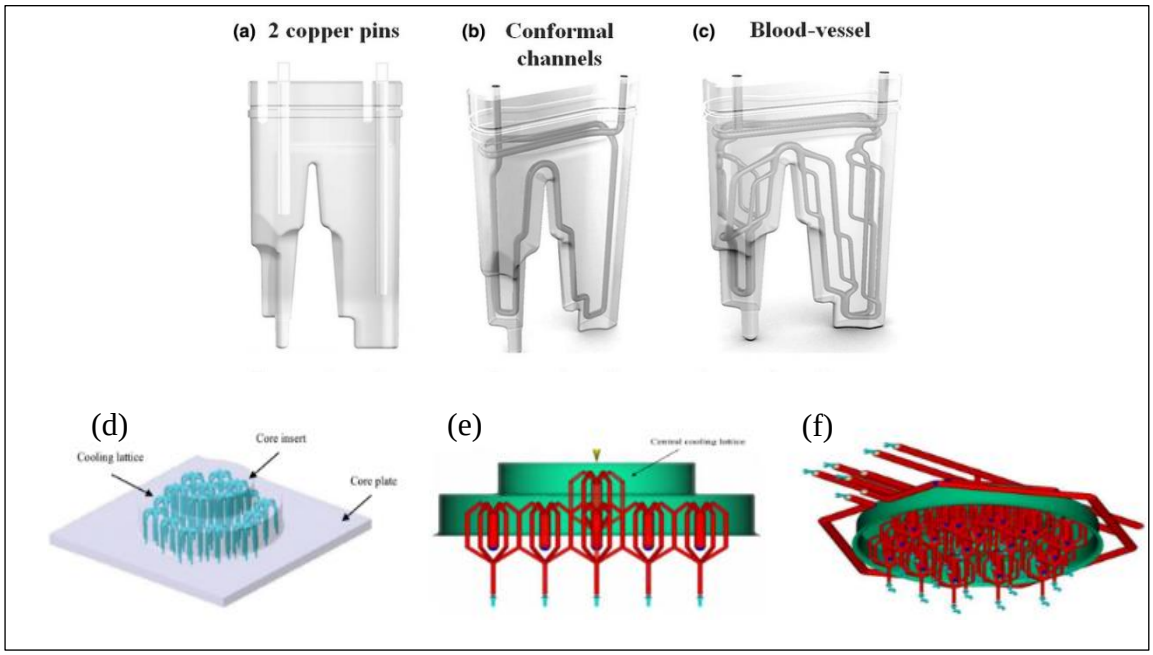

Figure 5 . Schematics of different cooling channels: (a) cooper pin, (b) conformal channels, (c) bioinspired design with subdivisions of 2 small diameters (Adapted with permission from reference [6]), (d) isometric view of proposed Honeycomb design, (e)Schematics of the Honeycomb design for lower half , and (d) upper half of the mold [10]

The cooling process is accelerated by increasing the diameter of the cooling line. However, the limitations of AM must be kept in mind, including the collapse, or warping of large internal channels/holes, which can lead to the failure of parts. Tan et al. [11] proposed support structures beneath the overhang to solve the mentioned challenges, as illustrated in Figure 6. Self-supporting channels (Figure 6-b) can successfully reduce the cooling time of an injection mold by more than 20% compared to CCC with smaller diameters (Figure 6-a), while also maintaining the mold's strength. Notably, the strength of these molds exceeds that of solid molds, with a measured ultimate strength of 1340 MPa compared to 1165 MPa.

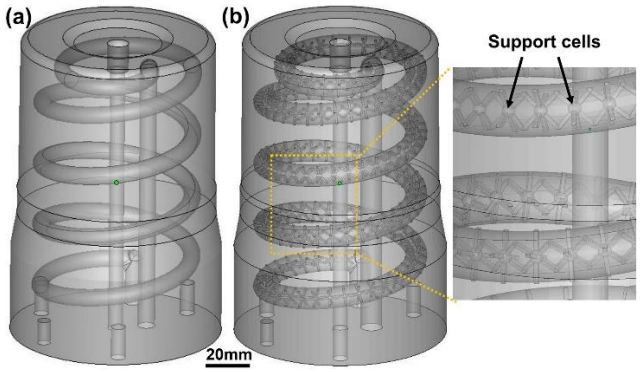

Figure 6. CAD design of one half of mold containing: (a) CCC and (b) with its support preventing distortion during the manufacturing process [11]

1.1.3.3 Other Alternative Approaches: mold-conforming CCC Designs

Numerous comparative studies have examined CCCs in injection molding, both numerically and experimentally, in comparison to conventional cooling channels. studies showed that conformal cooling systems can significantly improve the quality of the molded part during the injection molding process, and could provide 89.92% - 93% faster cooling than the mold without cooling channels [7, 13, 59]. Gruber et al. [12] emphasized the efficiency of CCC designs in reducing cooling time. In their study, various CCC designs were compared with a conventional cooling channel, including Z type, rectangular, and helical shapes (Figure 7-a to Figure 7-c, respectively). Although the differences in cooling time among the systems were marginal (less than 3 seconds), productivity was significantly impacted. For instance, the helical shape outperformed the Z type, yielding approximately

1.12 times more parts per year, equivalent to around 600 additional pieces. Additionally, Kuo et al. [8] investigated profiled CCCs (PCCC) (Figure 7-e), demonstrating their advantages over circular CCCs (CCCC) (Figure 7-d). The study revealed that PCCC-equipped injection molding tools exhibited smaller temperature differences between parts, shorter wax pattern cooling times, and higher cooling efficiency compared to circular CCCs. A combination of the conventional cooling channels like baffle design with the newly generated CCC could also improve the production rate and quality, and reduces the number of weld lines, warpage, residual stress, sink marks, and shrinkage [62]. Park et al. [9] commented on the importance of CCC in cycle times in addition to cooling time. When switching from conventional to CCCs, the cooling time could be reduced from 42s to 13s (approximately 69%), while the cycle time could be reduced from 56 to 27 s (approximately 52%). Reduced cycle times will reduce energy and manufacturing costs, and thus represent a significant benefit of CCC in injection molding.

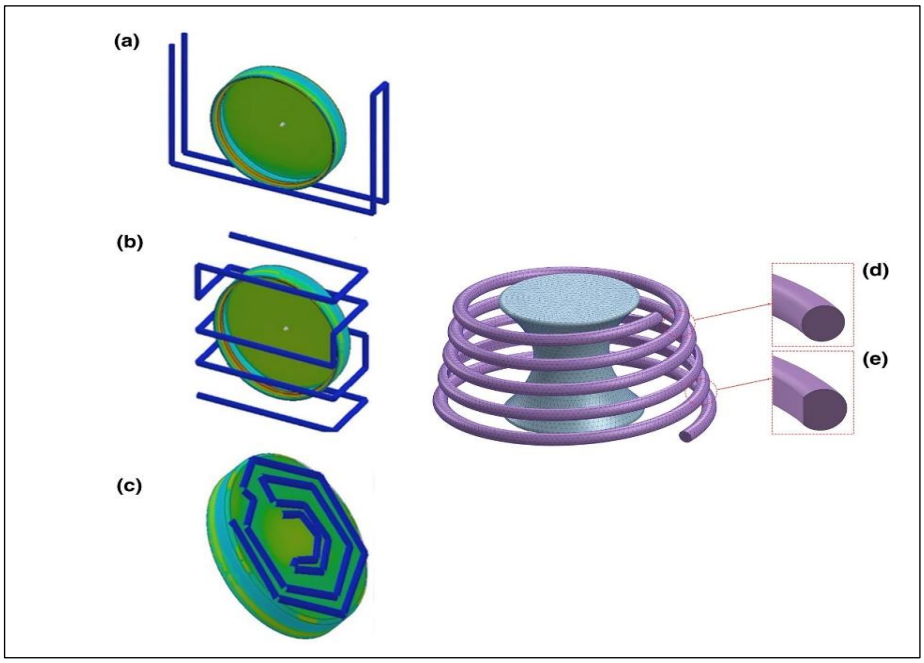

Figure 7. Three different designs of (a) "U" type circuit, (b) "Rectangle" type circuit, and (c) "Helical" type circuit (Adapted from reference [12] under the terms of the Creative Commons CC BY license), and schematic of one proposed profiled with (d) circular CCC(CCCC), and (e) profiled CCC(PCCC)

Another study introduces a novel method for generating conformal cooling channels (CCCs) in injection molds. In this method, manufacturers only need to identify hot or critical points in the software, following which the CCC line is automatically generated using the centroidal Voronoi diagram (CVD). The generation process is illustrated step by step in Figure 8-a to Figure 8-e, using a helmet case study—from the creation of the offset from the object to the generation of CCCs. While the simulated injection technique using these CCCs demonstrates a shorter cooling time, further investigation is required to assess their mechanical strength and durability [63].

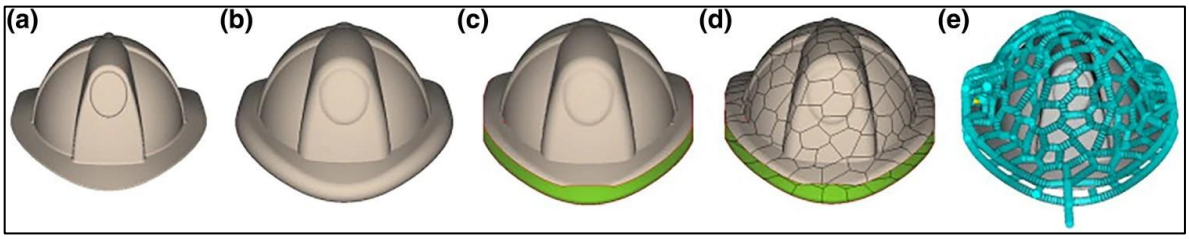

Figure 8. CCC generation process: a) helmet, b) offset of the helmet, c) Voronoi diagram, d) CAD view of generated CCC(Reprinted with permission from reference [63])

Beyond simply reducing cooling time, molds produced by additive manufacturing (AM) must also consider their final price. Marques et al. [64] assert that CCC become particularly valuable when the product features complex geometries that conventional linear cooling channels cannot adequately address in terms of heat transfer. Moreover, Gruber et al. [12] emphasize the significance of proper CCC design, noting that it can lead to a shorter return on investment (ROI). For example, helical channels (Figure 7-c) demonstrate a more favourable ROI compared to Z-type and rectangular designs (Figure 7-a and Figure 7-b, respectively). This suggests that investing in the proper design of CCC can yield substantial cost benefits, especially when dealing with intricate geometries where traditional cooling methods fall short

In this regard significant effort has been dedicated to establishing a comprehensive guideline for the design of CCCs. In terms of geometry and design, Kuo et al. [65] suggests the 2mm would be optimum distance between the CCC wall and the mold’s surface. A

comprehensive guideline of CCC design is presented in Table 1 with three important parameters of a,b, and c which are further presented in Figure 9. In this table, three types of classification according to the literature are presented. For each classification, a specified range of the hole diameter (cooling channel diameter specified by parameter b) is provided, along with recommended distances of the centre of CCC from the mold surface, illustrated by parameter c. Additionally, recommended distances between the centres of the channels are shown by parameter a.

Table 1. Design recommendations for cooling channel dimension regarding 3 different wall thickness classifications [64]

Classification	Wall thickness (mm)	Hole diameter (mm)-b	Centerline from a hole distance (mm)-a	Center hole from cavity distance (mm)-c
1	0–2	8–10	$c = 0.7a + 1.6b$	
	2–4	10–12		
	4–6	10–14		
2	0–2	4–8	$2b \leq a \leq 3b$	$1.5b \leq c \leq 2b$
	2–4	8–12		
	4–6	12–14		
3	–	6–12	$2b \leq a \leq 5b$	$b \leq c \leq 5b$

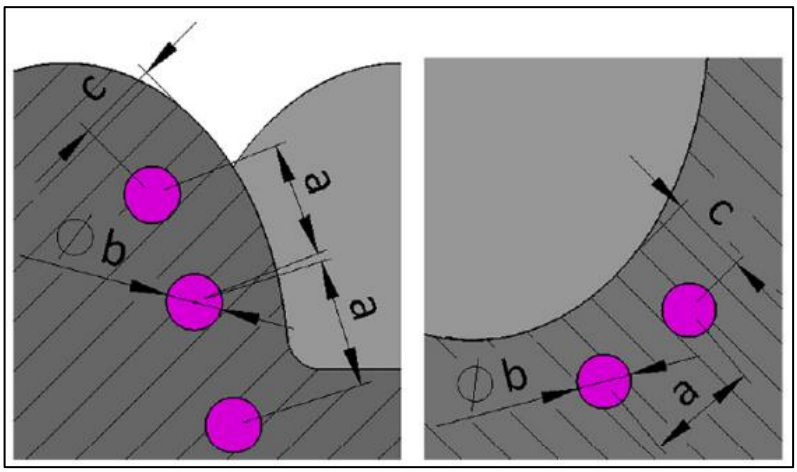

Figure 9. Parameters a and b are presented for CCC design (Reprinted from reference [64]under the terms of the Creative Commons CC BY license)

1.1.3.4 Integrating traditional and CCC designs for enhanced mold cooling; hybrid cooling designs

In the case of large molds, the manufacturing costs associated with additive AM may render CCC economically unfeasible. Therefore, the next logical consideration is hybrid manufacturing, which involves the use of additively manufactured inserts in existing forged molds to modify them. Mueller et al. [66] conducted a successful study highlighting the advantages of using AM to produce metal forming and aluminium die-casting tools through laser beam melting (LBM). They observed that employing new-generation additively manufactured tool inserts could reduce holding time (cooling) by 50%, resulting in a 20% reduction in the total cycle time. Similarly, Armillotta et al. [48] reported that incorporating CCC inserts into molds improves casting production efficiency by reducing shrinkage and loosening. They conducted approximately 2000 casting cycles using AM-inserts, which showed no signs of wear or damage

1.1.4 **Reviewing AM of H13 tool steel: processing parameters, density, and microstructural**

Hot work steels are preferred for tooling applications due to their outstanding mechanical properties at high temperatures, toughness, and resistance to thermal fatigue cracking [67]. Although AM of steels presents challenges, there have been several reports of successful manufacturing of metals material by different methods of AM such as selective laser melting (SLM) of hot work steel tools, laser engineering net shape (LENS) of H13 [25] and free crack fabricated samples by laser metal deposition [31]. SLM has been reported as one successful and high precision method for fabricating CCC with H13. In the following sections, the effect of the most influential parameters of SLM process including pre-heating, laser power, scanning speed, and hatching space on the physical, microstructural and mechanical properties of the SLM manufactured (SLM-ed) H13 has been discussed.

1.1.4.1 Relative Density

In powder bed manufacturing methods such as SLM, achieving 100% relative density in parts is challenging due to several factors. Firstly, the process parameters such as low laser power density, high scanning speed, and hatching distance lead to partial melting of powders during the process, resulting in irregularly shaped porosities upon cooling. Additionally, spherical or keyhole porosities can form due to metal alloy element evaporation or inert gas trapping, also angular or rectangular porosities may occur due to fusion failure [27, 51]. Consequently, the relative density often falls below 100%. Table 2 presents optimal processing parameters suggested by literature for SLM-ed H13.

There are different reports on the effect of laser speed on relative density. A study by Fonseca et al.[51] shows that increasing the speed results in an increased relative density for speeds ranging from 300 to 700 mm/s, another study by Jungsub Lee et al [27] shows that increasing scanning speed up from 200 mm/s to 800 mm/s reduces the relative density, which is shown in Figure 10. This is due to the effect of other parameters like laser power, hatching distance, the printing strategy, pre-heating temperature, etc. To comprehensively assess the impact of key parameters together, researchers often employ volumetric energy density (VED), as depicted in Equation 1as a variable parameter, which is a combination of laser power, scan speed, hatch space, and layer thickness. There is an optimum VED, as VED increases, density increases, and after the turning point, density decreases, also the part loses surface quality due to the ball effect. However, because VED combines several parameters, it is not recommended that it be used solely as a processing parameter. It could be increased, for example, by increasing the laser power or decreasing the scanning speed. A high laser power level results in a ball effect and poor surface quality, but the same VED can be achieved by slowing down and increasing the hatching distance [68, 69]. On the other hand, it should mention that VED does not cover all the processing parameters, including laser specifications such as the laser beam type (fiber or CO2) and laser beam diameter.

$$E = \frac{P}{V \times H \times t}$$ Equation 1

E: Energy density (J/mm^3)

t: Layer thickness (mm)

P: Laser power (W)

V: Laser scan speed (mm/s)

H: Hatch distance (mm) [69]

Table 2. Maximum obtained relative density of SLM-ed H13 with the corresponding processing laser power, scanning speed, hatch distance, and layer thickness parameters

Equipment	**Laser power (W)**	**Scanning speed (mm/s)**	**Hatch distance (µm)**	**Layer thickness (µm)**	**Density (%)**	**Reference**
OmniSint-160 machine	172	700	80	30	98.3	[51]
SLM Solutions 250 HL	150	300	50	*	99.7 ± 0.1 200	[70]
SLM 125 HL solution	160.4	534.7	100	30	99.94	[69]
	300	1000	100	30	99.94	
ORLAS CREATOR	152	100	40	50	~99%	[48]
EOS M280	100-300	200-1200	80-120	40	99.7%	[71]
SLM machine of KU Lueven	170	400, 800	105	30	>99%	[26]
EOS M280	200	1000	90	20	99.13	[72]
SLM Realizer II 250	200	100	180	50	≥ 99.8%	[73]
SLM 280HL	375	790	120	50	99.9	[74]

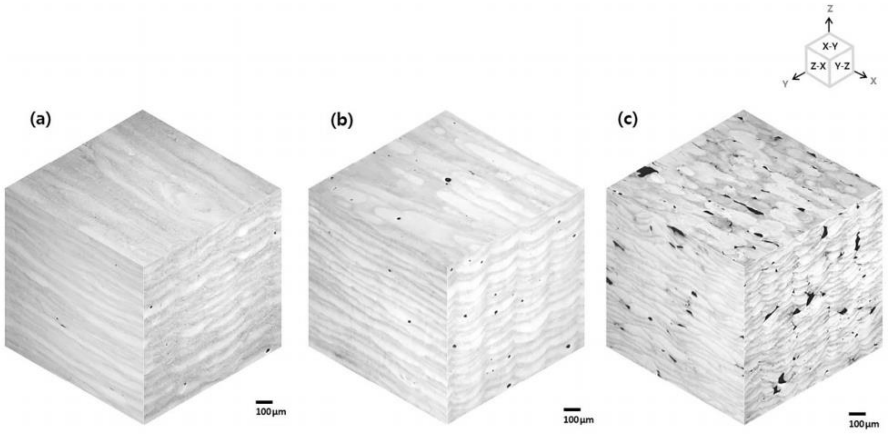

Figure 10. Isometric view of the sample showing the porosity for the different scanning speeds: (a) 200, (b) 400, and (c) 800 (Reprinted with permission from reference [27])

1.1.4.2 Microstructure

H13 tool steel contains Cr, V, Mo, Mn, and Si as alloying elements. In the annealed H13 phase diagram, alpha-Fe has been determined to be the dominant phase, followed by cementite. However, SLM-ed H13 show slightly different phases. During SLM of H13, the powder particles melt and cool rapidly, and as a result, some undesirable and unpredictable phases appear, affecting the mechanical properties. Table 3 compares the recognized phases of wrought H13 and SLM-ed H13 based on different reports. Mainly Wrought H13 consists of the bcc-structured alpha-Fe as the dominating phase and the cementite Fe_3C phase, while, a significant volume of retained austenite (FCC structure) and martensite are dominant phases in SLM-ed H13. Martensitic transformation is due to the high cooling rate during SLM, approximately 1.83×10^4 K/s, which is more than the critical cooling rate for martensite transformation of wrought H13 (20 K/s). It is important to understand that retained austenite is not a desirable phase for molds and dies because volumetric expansion during the transformation of retained austenite to martensite causes distortion or cracking. In wrought H13 subjected to three different treatments, the formed carbides remain relatively consistent, primarily comprising $M_{23}C_6$ and M_7C_3. However, in the case of SLM-ed H13, a diverse range of carbides is reported, including M_7C_3, MC, and M_3C [26, 28, 31, 51, 70].

Table 3. Phase distribution and precipitated/microconstituents in wrought and SLM-ed H13

Annealed wrought H13[75]	Quenched wrought H13[75]	Quenched and tempered wrought H13[75]	Annealed- SLM-ed H13
Alpha-Fe	Alpha-Fe	Alpha-Fe	Alpha-Fe[48]
Fe_3C[48]	Fe_3C[48]	Fe_3C[48]	Fe_3C[48]
$M_{23}C_6$	$M_{23}C_6$	$M_{23}C_6$	Martensite [71, 76, 77]
M_7C_3	M_7C_3	M_7C_3	Austenite[71] (less than initial powder)[76]
	Martensite	Martensite	Retained austenite (16.5%–29.7%) [51, 71, 77]
		Tempered martensite	M_7C_3[76]
		vanadium carbides (not dissolved during austenizing)	MC [76]
		Bainite	M_3C[76]
		Pearlite-bainite	Binate (by preheating)[26]

The inherent tempering treatment during the SLM process contributes to microstructural heterogeneity in SLM-ed H13. This phenomenon arises from the layer-by-layer methodology, where each solidified layer undergoes reheating and recooling during subsequent layers, potentially leading to re-austenitization and tempering of the initial layers. This results in a material with a high content of retained austenite, predominantly found in the initial and mid layers, while the last manufacturing layers exhibit a higher content of martensite. Microstructural studies reveal a heterogeneous structure in grain orientation also, with grains oriented along the building direction corresponding to the highest heat flux towards the base plate. The grain orientation and microstructure in the martensitic structure are influenced by diffusion less transformation, characterized by the rapid cooling from FCC to BCT [51, 78]. Scanning speed shown to be significantly affective in grain size, with higher speeds resulting in smaller grains[27, 31, 51, 70]. In the following the microstructure along the building direction will be examined at two scales: initially, focusing on a single laser track and subsequently, analysing the entire sample (Figure 11).

On a smaller scale in one laser track (separated by black lines in Figure 11-a), in the heat affected zone (HAZ) and bottom areas, a cellular/dendritic structure and some precipitation (even more in HAZ) has been reported. It is reasonable to conclude that the materials in each layer have different microstructures and that the hardness increases from bottom to top.

Regarding the microstructural changes throughout whole the sample and in the building direction, in the last melted layer, un-tempered martensite and retained austenite phases are recognized because of the high solidification rates and no reheating. In contrast, several treatments occur in early printed layers as a result of the heat transmitted to them when the new layer is printed. In this case, there are two possibilities: if temperatures rise above AC3, austenite transforms to martensite via fast cooling, except for the cell walls, which remain austenitic due to segregation. Second, by continuing the process, the lower materials are subjected to tempering, and a mixed microstructure of martensite and austenitic phase forms, as shown in Figure 12. It is worth mentioning that this unavoidable tempering leads to nonuniform microhardness through the building direction and the microhardness decreases from the edge to the middle [51].

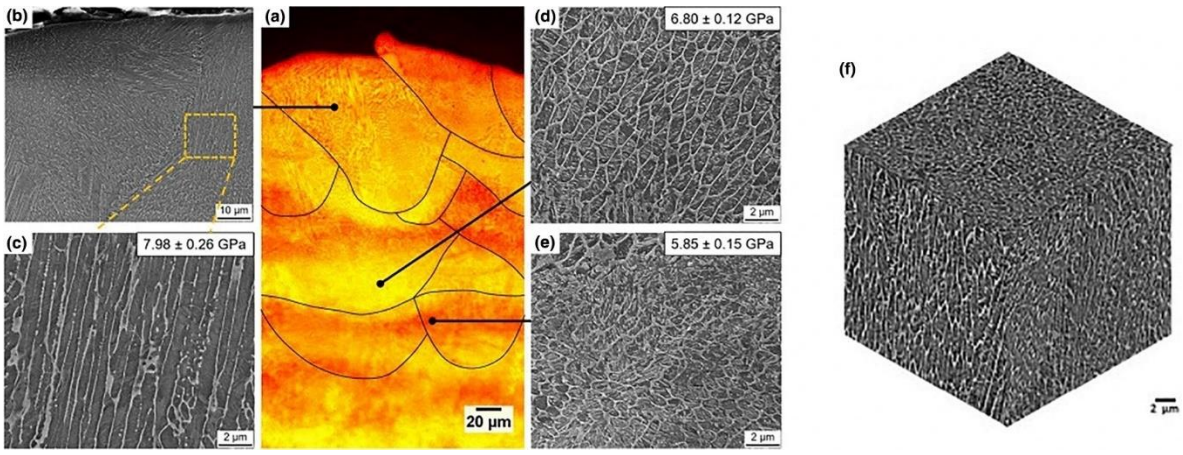

Figure 11. Microstructure of H13 in: (a) schematic of laser track in building direction and (b,c,d,e) higher magnification of microstructure in different melting zoon in the laser track, (Reprinted with permission from reference [51]),and (f) isometric view of microstructure (Adapted with permission from reference [27])

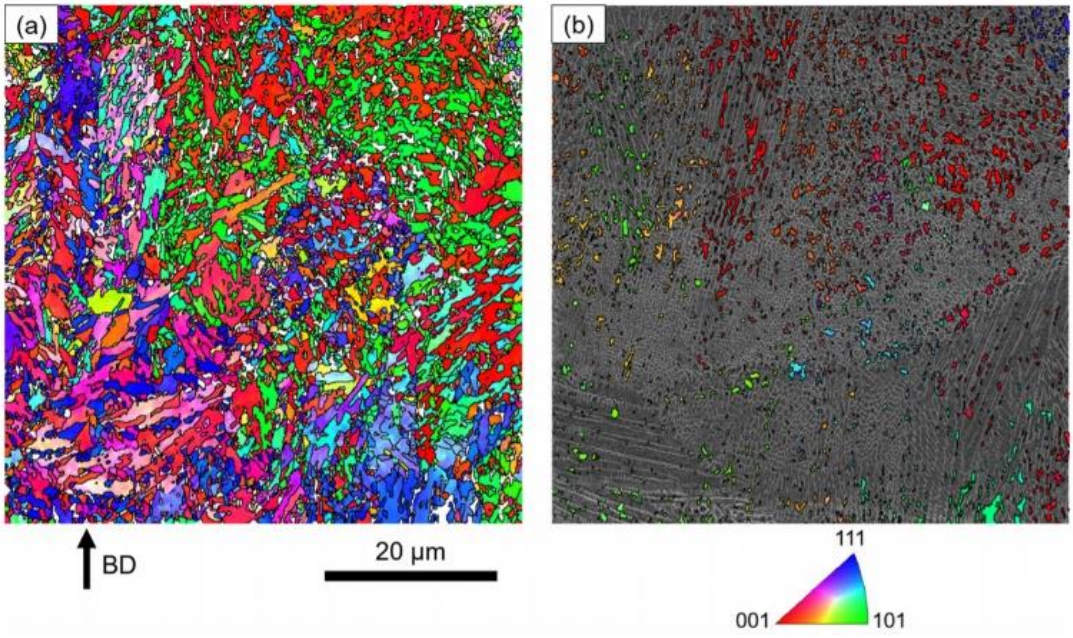

Figure 12. Morphology of (a) Martensite, and (b) austenite directions(Adapted with permission from reference [51])

a) *EFFECT OF PRE-HEATING ON THE MICROSTRUCTURE*

During the H13 SLM process, rapid solidification leads to martensite formation, especially in the area close to the surface the formed martensite is more since the lower layers experience tempering treatment. This difference in microstructure leads to compressive stress. Preheating the base plate up to 400ºC keeps the material temperature above the martensite transformation temperature (300-350ºC), resulting in bainite formation and a more uniform microstructure. This could change the surface stress from 324 MPa of compressive stress to 371 MPa of tensile stress, also a reduction in microhardness value compared to the not preheated plate. By increasing the preheating temperature up to 400ºC, the Ultimate strength of SLM-ed H13 will increase to around 1965 MPa which is higher than the ultimate strength of not pre-heated plate (around 1712 MPa), and even very close to the wrought H13 (approximately 1990 MPa). However, by increasing the preheating temperature the yield stress and elongation will drop, and the obtained values at 400ºC are less than both the wrought and not pre-heated plate[26].

1.1.5 **Reviewing AM of H13 tool steel: mechanical behaviour**

1.1.5.1 Tensile behavior

The yield and tensile strengths of wrought H13 in the hardened condition were in the range of 1290-1570 and 1500-1960 MPa, and in the annealed condition were around 370-510 and 670 MPa, respectively [76]. The tensile strength of AM-ed H13 tool steel is affected by manufacturing parameters such as the scanning speed, which affects the porosity and microstructure. A higher scanning speed leads to more porosity and, as a result, lower tensile strength. However, there is an optimal speed for the highest ultimate strength [27]. The tensile strength obtained from the literature is shown in Table 4.

Table 4. Tensile strength of H13 steel manufactured by additive manufacturing

Equipment	**Laser power (W)**	**Scanning speed (mm/s)**	**Hatch distance (µm)**	**Ultimate strength (MPa)**	**Condition**	**Reference**
Concept laser M-LAB	90	200	80	1700	As built	[27]
EOS-M290	160-180	350-450	100	1909	As built	[28]
SLM machine of KU Lueven	170	400, 800	105	1965	As built	[26]
SLM 125 HL	175	720	120	1289 ± 6	As built and stress relieved	[30]
SLM 125 HL	100	250	120	513	As built	[79]
SLM 125 HL	175	725	100	1430±12	As built	[49]

1.1.5.2 Fatigue behavior

Thermal fatigue is the primary cause of mold failure, accounting for approximately 70% of cases. According to reports by Pellizzari et al. [80], the fatigue resistance of SLM-ed H13 at room temperature is approximately half that of forged H13. A study by Dörfert et al. [81] confirms the lower fatigue resistance of SLM-ed H13 compared to wrought H13. Similarly, Maciej Mazur et al. [82] reported inferior fatigue resistance of tempered SLM-ed H13.

In contrast, the fatigue behavior of SLM-ed H13 at high temperatures (650 °C) demonstrates improved fatigue resistance. The main parameters influencing the fatigue behavior of SLM-ed H13 include hardness, phase distribution, and defects arising from the SLM process.

The initial and final hardness of the material strongly affect its fatigue resistance. The as-built SLM-ed H13 exhibits higher initial hardness compared to wrought H13 due to the presence of a significant amount of martensite. This martensite formation occurs because the temperature during the process exceeds the austenitic transition temperature (Ac3), followed by rapid cooling rates sufficient for martensite formation (around 350 °C). Additionally, the hardness of SLM-ed H13 increases under mechanical load at 650 °C, contrasting with wrought forged H13. The increase in microhardness of as-built SLM-ed H13 is attributed to the transformation of a significant volume of soft retained austenite (approximately 11%, accumulated in the cellular wall) into the hard martensite phase, along with secondary precipitation of carbides occurring at higher temperatures (around 650 °C). In addition, microstructural investigations during thermal fatigue tests reveal that the cellular structure dissolves into the alpha matrix, reducing lattice spacing and increasing hardness [83, 84].

The presence of a significant volume of retained austenite in as-built SLM-ed H13, which is softer compared to the martensite phase, plays a crucial role in increasing fatigue resistance under high-temperature and mechanical load conditions. Retained austenite enhances fatigue resistance by impeding crack initiation and propagation through two mechanisms. Firstly, the presence of retained austenite softens the material, reducing resistance to dislocation movements, thereby preventing crack propagation and increasing initiation resistance. Secondly, retained austenite aids in crack closure by inducing compressive residual stress during transformation to martensite at approximately 650 °C. However, it should be noted that the effect of retained austenite diminishes over time due to near-complete transformation to martensite. Figure 13-a, and Figure 13-b and illustrates the crack growth for as-built SLM-ed H13 (printed with a strategy of 67-degree rotation in each layer) compared to forged H13 during a high-temperature fatigue test. It is evident that for

each cycle number, the crack length is shortest for the unheated specimen, followed by the heat-treated SLM-ed, and finally the forged specimen [83].

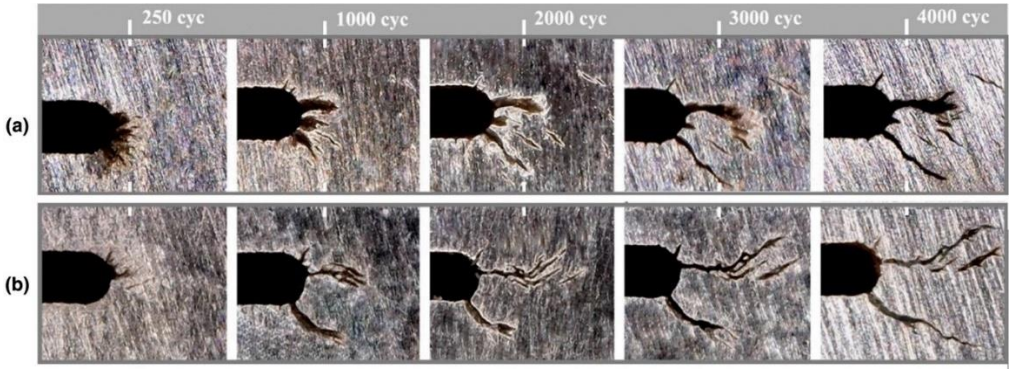

Figure 13. Crack images of the (a) As-built SLM-ed H13 (b) Forged H13 after different numbers of cycles (250, 1000, 2000, 3000, and 4000) (Adapted with permission from reference [83] under the terms of the Creative Commons CC BY license)

Manufacturing defects in SLM-ed H13, including microporosity and lack of fusion (LOF), inevitably impact fatigue resistance. These defects vary in size, shape, and distance from the surface, with LOF identified as the primary contributor to poor fatigue behavior. Figure 14illustrates how these defects are oriented differently in samples depending on the building direction. In particular, defects in the 0-degree direction are larger, closer to the surface, and perpendicular to the fatigue force loading, often characterized by sharp tips. Consequently, the fatigue behaviours of SLM-ed material is non-uniform. Optimizing processing parameters to minimize LOF is essential for enhancing fatigue resistance [80].

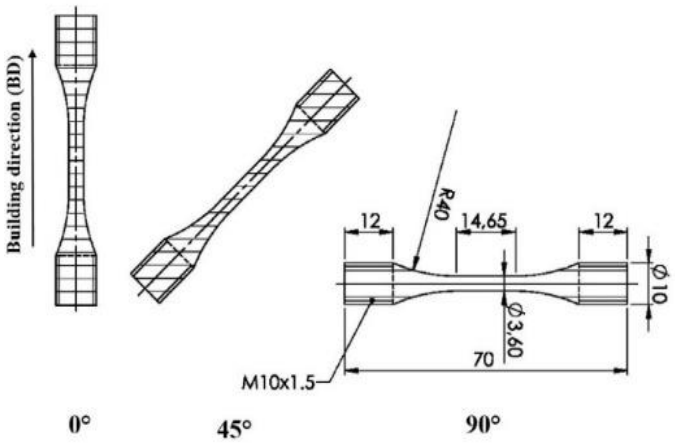

Figure 14. Fatigue samples manufactured by SLM and their attributed orientation that is defined by the degree of samples from the building direction (Adapted with permission from reference [80])

To enhance fatigue resistance, surface treatments following the manufacturing process are recommended. It's crucial to investigate crack growth in terms of both surface propagation and depth. Among surface treatments, gas nitriding stands out for offering an optimal combination of hardness and toughness, thereby extending the thermal fatigue cycles. Additionally, combining shot peening post-treatment with gas nitriding further enhances fatigue properties by inducing compressive residual stress in SLM-ed H13. Laser surface treatment presents another viable option by quickly remelting and cooling a surface layer, thereby forming martensite and increasing hardness, ultimately extending fatigue life [85-88].

1.1.5.3 Hardness

The hardness map is varied, owing to the various microstructures within printed parts [51]. The hardness of the as-built H13 is 57 HRC, while that of the wrought H13 is 45 HRC (after tempering at 610°C) [70]. Some martensite structures may have decomposed into alpha- Fe and carbides because of the presence of different cooling rates in different regions and the cyclic thermal effects from successively built layers (i.e., Fe_3C). From the support material to the final printed surface, the hardness map shows an increasing trend, which could

be explained by the tempering of each layer, while new layers are molten. A suitable temperature causes a global hardness rise with a lower gradient in hardness when moving from the top surface to the support-stacked surface [26]. The global hardness and scanning speed have an inverse relationship: increasing the scanning speed reduces hardness due to the increased porosity present [27]. Table 5 summarizes the average hardness value for the previous studies.

Table 5. Summary of hardness values reported in previous studies versus their corresponding processing parameters

Equipment	Laser power (W)	Scanning speed (mm/s.)	Hatch distance (μm)	Hardness (HV)	Reference
Concept laser M-LAB	90	200	80	585	[27]
SLM 125 HL	150-175	450-720	120	562	[28]
SLM solution	280	980	120	597	[83]
ORLAS CREATOR	152	100	40	708.4	[48]
EOS M280	100-300	200-1200	80-120	650-689	[71]
SLM machine of KU Lueven	170	400, 800	105	894	[26]
SLM 125 HL	175	720	120	47	[30]
SLM 125 HL	100	250	120	549	[79]

1.1.5.4 Residual stress

Residual stress plays a critical role in the accuracy and stability of parts during the manufacturing process, often leading to issues such as cracking and breakage. In the case of as-built H13 processed by SLM, a residual stress map reveals significant compressive residual stress along the building direction. However, it is noteworthy that this stress distribution is non-uniform and varies throughout the building direction [70].

Generally, residual stress is calculated by a material's young's modulus, Poisson's ratio, lattice spacing, and tilt angle. Assuming the SLM-ed H13 has the same Poisson's ratio and Young's modulus as wrought H13, the lattice of the a-Fe phase in the as-built SLM-ed H13 is distorted, meaning that the lattice parameters are increased compared to the wrought H13. This is due to the Cr, Mo, and V elements enrichment in the alpha-Fe phase and results

in high residual stress. Other contributors to the residual stress of SLM-ed H13 that are attributed to the fast cooling during the SLM process are elastic and plastic deformation, thermal gradient, and phase transformation during the cooling stage. The high value of residual stress (ranging from 940 MPa to 1420 MPa, compared to 1650 MPa for yield stress) is still in the elastic area and could be removed by the post-treatment treatments. Two other remaining factors are the thermal gradient and phase transmission. martensite transformation causes 4% volume expansion and compressive residual stress in contrast to the tensile residual stress caused by the thermal gradient. The compressive stress caused by phase transformation is far greater than the tensile residual stress caused by the thermal gradient. As a result, martensite phase transformation is the main reason for a significant portion of the compressive stress. For wrought H13 parts containing the phases mentioned, a stress-relieving heat treatment at 600–650°C is recommended. During stress-relieving post-treatment, which is mostly done for 3D printed parts, the decomposition of martensite to ferrite and carbides will reduce the amount of final residual stress [26, 28, 70]. However, the retention of austenite and martensite in SLM-ed H13 may necessitate different furnace treatments, which will require further investigation.

1.1.6 **Post-treatment**

In high thermal cycles, statistical or cyclic loads cause thermal fatigue, wear erosion, and stress corrosion. As a result, post-treatments are applied to the molds to improve their mechanical qualities and hence lengthen their life cycle. The normal post-treatments of wrought H13 are annealing, quenching, and tempering, which are consequently required for SLM-processed H13. For SLM-ed H13, the initial challenge of residual stress is partially controlled by printing parameters and could largely be removed by a stress-relieving post-treatment. Retained austenite will decrease from 19% to 2% by austenitizing and quenching at 1020ºC. Tempering treatment converts martensite into tempered martensite and precipitated carbides. For a tempering temperature in the 350-650ºC range, the maximum hardness can be obtained at a mid-tempering temperature of around 550 ºC due to needle-form carbides (600 Hv0.3) and secondary hardening phenomenon. At higher tempering

temperatures around 650 ºC, needle-form carbides change into coarse-form resulting in lower hardness. The ultimate strength and yield strength of as-built H13 could be raised to 1938 MPa, and 1483 MPa respectively at a tempering temperature of around 600 ºC. Increasing in tempering temperature to around 700 ºC leads to a reduction in hardness (half of the hardness at 600 ºC; 376 to 629 respectively at 700ºC and 600ºC), and a reduction in mechanical strength(1076 MPa and 877 MPa respectively for ultimate strength and yield strength), but doubles the breakage elongation; 10.95% at 700ºC. Yong's modulus value is less sensitive to the tempering temperature and the change is around 2.5% with a maximum value of Yong's modulus at 650 ºC (326.56 MPa and 318.87 MPa respectively for tempered H13, and as-built H13) [47-49, 89].

The Hot Isostatic Pressing (HIP) process reduces the porosity and improves mechanical properties such as tensile strength but has no significant effect on the global hardness [28, 30, 44]. Kumar et al. [35] researched improving the hardness and wear resistance of additively produced H13 by tempering and coating. The microhardness of the as-built sample increased after using both post-treatments by 1.55 times and 3.99 times, respectively.

Post-surface treatments are also required for materials processed by SLM due to the relatively high surface roughness of such materials. High surface roughness is one source of weakness in fatigue resistance, and wear resistance. Various types of surface treatments are recommended, such as chemical treatments (where there is a limitation in geometry for mechanical post-treatments like lattice structures), laser-based treatment like laser peening, laser cleaning, and laser polishing (where improvement in mechanical properties is necessary), mechanical surface treatments like sandblasting and shot peening (which can impose compressive residual stress), and coating [34, 90-92]. Based on a comparative study of laser polishing, electrochemical polishing, and shot peening surface treatments on the fatigue life and hardness of H13 manufactured by SLM, laser polishing and shot peening were shown to be more reliable than chemical polishing since there is a possibility of a chemical reaction and new phase formation, also forming porosity due to chemical reaction.

Results imply that SLM-ed and post-treated parts could have more fatigue strength compared to wrought H13 if they are followed by machining post-treatment [93].

1.1.7 Conclusion

In conclusion, the paper has explored the potential of AM in injection mold manufacturing to enhance mold lifespan and productivity. Despite the promising advantages of AM, such as the implementation of conformal cooling channels CCCs for superior thermal distribution, the current cost constraints may limit its widespread adoption, particularly for large mold's. However, hybrid manufacturing, which integrates AM with conventional methods, emerges as a viable alternative, with H13 hot work steel identified as a key material despite inherent processing challenges.

A comprehensive study of the microstructure of SLM-ed H13 has been conducted, revealing a cellular structure resulting from rapid cooling, enriched with alloying elements like V, chromium, and Si, indicating elemental segregation. While the material exhibits a near-full martensitic structure with relatively high retained austenite content, attributed to inherent tempering treatment during processing, mechanical property analysis highlights high hardness and brittleness. Nevertheless, fatigue life appears promising, surpassing that of conventional H13 due to martensite transformation to soft austenite under cyclic load.

Moreover, the material demonstrates high compressive residual stress from rapid cooling and martensite formation, leading to subsequent expansion and shrinkage, causing tensile residual stress. Surface roughness is notably elevated, prompting the recommendation of laser surface treatment for improvement. Additionally, to enhance toughness, annealing, tempering, and hot isostatic pressing (HIP) are suggested as potential post-processing methods.

Overall, the findings underscore the potential benefits and challenges associated with utilizing AM, particularly with H13 hot work steel, in injection mold manufacturing. Further research and development efforts focusing on optimizing processing techniques and post-treatment methods are warranted to fully harness the capabilities of AM in this domain.

CHAPITRE 2

OPTIMISATION DES PARAMÈTRES DE TRAITEMENT POUR AMÉLIORER LA RÉSISTANCE MÉCANIQUE DE L'ACIER À OUTIL H13 FABRIQUÉ PAR FUSION SUR LIT DE POUDRE (PBF) : RÉDUCTION DE L'INHOMOGÉNÉITÉ MICROSTRUCTURALE, LES POROSITÉS ET LA FORMATION D'OXYDES

Narges Omidi[1*], Manel Houria[2], Mohamed Meher Monjez[1], Mohammad Jahazi[2]
Noureddine Barka[1],
[1]Department of Mathematics, Computer Science and Engineering, Université du Québec à Rimouski, Rimouski, QC, Canada
[2]Department of Mechanical Engineering, École de technologie supérieure, Montréal, Québec, H3C 1K3, Canada

RÉSUMÉ EN FRANÇAIS DU DEUXIÈME ARTICLE

Ce travail de recherche met en lumière l'importance de la densité d'énergie volumétrique (VED) dans des aspects cruciaux de l'acier H13 fabriqué par la méthode PBF, à savoir la morphologie de la porosité, l'homogénéité microstructurale et l'oxydation. L'étude montre que la porosité en forme de trou de serrure près du bord est le principal facteur préjudiciable à l'intégrité de la pièce construite, et que la morphologie peut être contrôlée par une sélection appropriée de la VED. De plus, il a été constaté que l'inégalité microstructurale dans l'acier H13 fabriqué par PBF est causée par la ségrégation des éléments d'alliage lors de la fusion et de la solidification, ce qui devient plus prononcé et distinct lorsqu'il est associé au phénomène de formation de bouchons à des niveaux de VED plus élevés. Il a été observé qu'avec plus de ségrégation, il y a une possibilité plus élevée de formation d'oxyde à l'intérieur du matériau après traitement thermique, ce qui est préjudiciable aux propriétés mécaniques. La plage de VED de 57 à 59 J/mm^3 est identifiée comme une plage appropriée pour éviter les trous de serrure et les gros pores de gaz près de la surface, tout en maintenant

un bain de fusion stable avec un minimum d'effet de formation de bouchons, contrôlant ainsi la formation d'oxyde après traitement thermique. De plus, une corrélation entre l'uniformité du profil de microdureté et la résistance mécanique est établie, ce qui indique l'utilisation potentielle de la microdureté comme critère prédictif pour la résistance mécanique dans les échantillons imprimés. Enfin, les résultats de l'étude ont été validés par la fabrication d'échantillons avec une VED dans la plage proposée, en utilisant des paramètres de traitement modifiés qui ont donné des échantillons fabriqués avec succès sans défauts de surface, et une taille d'oxyde optimisée, ce qui indique une résistance mécanique supérieure.

Cet article, intitulé « *Processing parameters optimization for enhanced mechanical strength in PBF-ed processed H13 tool steel: minimizing manufacturing defects including microstructural inhomogeneity, sub- surface porosities, and oxide formation*», a été soumis aux éditeurs de la revue The International Journal of Advanced Manufacturing Technology. En tant que premier auteur, ma contribution inclut la réalisation de recherches de pointe, la réalisation de tests expérimentaux, l'interprétation des résultats et la rédaction du manuscrit. Manel Houria, le deuxième auteur, contribue à l'analyse des données de diffraction des rayons X (XRD), et Mohamed Meher Monjez, le troisième auteur, contribue à la révision de l'article. Le professeur Mohammad Jahazi, le quatrième auteur, contribue au développement de la méthodologie et aux aspects métallurgiques de cet article en tant que mon co-superviseur. Le professeur Noureddine Barka, le cinquième auteur, a fourni l'idée originale, développé la méthodologie et révisé l'article.

2.1 PROCESSING PARAMETERS OPTIMIZATION FOR ENHANCED MECHANICAL STRENGTH IN PBF PROCESSED H13 TOOL STEEL: MINIMIZING MANUFACTURING DEFECTS INCLUDING MICROSTRUCTURAL INHOMOGENEITY, SUB- SURFACE POROSITIES, AND OXIDE FORMATION

2.1.1 Abstract

Additive manufacturing (AM) of H13 tool steel using the Powder Bed Fusion (PBF) process is often limited by issues such as porosity (including lack of fusion, gas, and keyhole porosity), balling formation, and elemental segregation. These factors significantly impact the mechanical properties of the final product. This research investigates how volumetric energy density (VED) influences these issues and their subsequent effects on mechanical properties. VED affects the mechanical properties in multifaceted ways. An optimized VED prevents lack of fusion, minimizes gas and keyhole porosities, especially near edges, ultimately reducing the material's susceptibility to fracture under tensile load. Additionally, VED influences elemental segregation within a single laser track during the process; lower VED leads to less elemental segregation. This reduced segregation minimizes oxide formation, which are crack initiation sites after heat treatment, thereby enhancing mechanical strength. The study also identifies that an optimal VED minimizes balling formation, further reducing elemental segregation and improving mechanical properties. A VED range of 57-59 J/mm³ is found to be optimal to prevent lack of fusion, minimize segregation, and reduce near-surface defects. Furthermore, a relationship is established between these defects, the microhardness profile, and the mechanical properties, suggesting that microhardness can serve as a predictive tool for mechanical properties.

Keywords: PBF, Oxidation, Balling effect, keyhole porosity, Gas porosity

2.1.2 Introduction

Injection molding, a cornerstone of modern manufacturing, enables mass production of complex plastic parts. However, conventional methods for creating injection molds often face limitations in cooling channel design, leading to uneven cooling, longer cycle times, and decreased efficiency. H13 tool steel, renowned for its exceptional hardness, toughness, and heat resistance, is the preferred material for these molds due to its ability to withstand demanding conditions [94, 95]. Recent advancements in Additive Manufacturing (AM) technologies, particularly powder bed fusion (PBF), offer a breakthrough solution. AM overcomes these limitations by enabling the creation of complex, conformal cooling channels (CCC) that closely follow mold cavity contours [96]. This innovation in mold design promises significant improvements, such as enhanced heat dissipation, faster cycle times, and ultimately, a more efficient and competitive injection molding process [97].

Porosity formation is a significant challenge in PBF of metals, including H13 tool steel. This defect negatively impacts the mechanical properties of manufactured parts and is typically measured and studied through the relative density of samples. PBF-ed samples exhibit both spherical gas porosities and irregular-shaped porosities [98]. Spherical gas pores arise from a dynamic process involving pore nucleation, growth, and outgassing during rapid solidification in melt pools. The formation of these pores is closely linked to the thermal conditions within the melt pool. Higher temperatures can promote gas entrapment by enhancing material vaporization and extending cooling. However, excessively high temperatures can also accelerate thermal gradients and thermal stress, leading to Marangoni convection. Marangoni convection, driven by variations in surface tension due to temperature gradients, pushes gas pores towards the melt pool surface. This phenomenon is crucial because gases are nearly insoluble in liquid metals. Consequently, Marangoni convection allows gases to escape from the surface, preventing their formation within the material [99, 100]. Irregular-shaped porosities in PBF fall into two main categories: lack-of-fusion (LOF) and keyhole pores.

LOF defects occur due to insufficient heat input, hindering proper bonding between melted material layers. In contrast, keyhole pores form as vapor-filled cavities when laser power is high enough to vaporize the material [101]. Figure 15 schematically compares the conduction mode in laser welding, where laser heat gradually melts and solidifies the material without creating a keyhole (Figure 15-a). Figure 15-b shows the keyhole mode. As the keyhole traverses the material in PBF, it may leave behind a void, resulting in a keyhole pore. These elongated pores can concentrate stress, making them susceptible to crack initiation and potentially compromising the structural integrity of the component [98, 102]. Laser power, speed, and beam size all influence keyhole formation and characteristics [102, 103]. Studies on porosity formation in PBF-ed H13 are largely limited to optimizing processing parameters for maximum relative density (Table 6). Researchers have investigated parameters like laser power, speed, and hatch spacing (refer to Table 6 for results). Additionally, studies like Narvan et al. [104] explored the correlation between Volumetric Energy Density (VED) and relative density. Their findings suggest a positive correlation between VED and relative density up to a threshold value (around 60 J/mm^3). Beyond this threshold, the effects become less clear, and not discussed. In addition, Mazur et al. [94] identified that VED exceeding 80 J/mm^3, while beneficial for density, can introduce dimensional inaccuracies, that is not also discussed clearly. Overall, the influence of processing parameters on the evolution of porosity within H13 PBF remains an under-explored area.

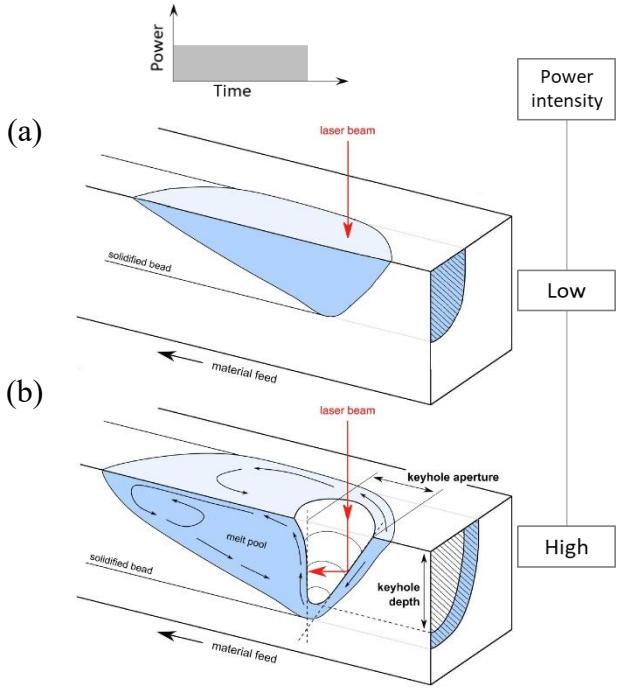

Figure 15. schematic of the keyhole prose formation in continuous laser welding at low and high power intensity in laser welding process (adopted from references [105, 106])

Table 6. Summary of previous studies investigating the influence of processing parameters on relative density

	Equipment	*Laser power (W)*	*Scanning speed (mm/s)*	*Hatch distance (μm)*	*Layer thickness (μm)*	*Relative Density (%)*	*Ref.*
POROSITY	OmniSint-160 machine	172	700	80	30	98.3	[51]
	SLM Solutions 250 HL	150	300	50	*	99.7 ± 0.1	[70]
	SLM 125 HL solution	160.4	534.7	100	30	99.94	[69]
	ORLAS CREATOR	152	100	40	50	~99%	[26]
	EOS M280	100-300	200-1200	80-120	40	99.7%	[71]
	SLM machine of KU Lueven	170	400, 800	105	30	>99%	[26]
	EOS M280	200	1000	90	20	99.13	[72]
	SLM Realizer II 250	200	100	180	50	≥ 99.8%	[73]
	SLM 280HL	375	790	120	50	99.9	[74]

The rapid solidification inherent to the PBF process significantly impacts the microstructure of H13 tool steel compared to conventional manufacturing methods. This rapid cooling presents two key challenges: retained austenite and elemental segregation.

One well-documented consequence is the presence of retained austenite (ranging from 16.5% to 29.7%) in PBF-ed H13 [75, 107, 108]. This occurs because the rapid cooling hinders the complete transformation of austenite to the desired martensitic phase [51, 71, 77]. Mitigation strategies, such as preheating the baseplate during PBF to maintain temperatures above the martensite transformation point, are being explored to address this challenge.

However, a less understood and potentially more critical challenge arises from elemental segregation within the melt pool of PBF-ed H13. Elemental segregation refers to the uneven distribution of alloying elements within the solidified materials [109, 110]. This phenomenon can have a dual effect on mechanical properties. On the one hand, it can concentrate elements in specific areas, potentially enhancing localized strength (similar to how chromium segregation improves properties in 316L stainless steel) [111]. Conversely, high concentrations of elements like Mn, Si, S, and C in steels can lead to micro-segregation at grain boundaries, increasing crack susceptibility [112]. In the case of H13, well-documented research exists on micro-segregation within the cellular walls of the microstructure, which often includes carbon and other alloying elements like vanadium (V), molybdenum (Mo), chromium (Cr), and silicon (Si) [111, 113-119]. However, research specifically focused on macro-segregation at the melting pool boundaries in PBF-ed H13 is scarce. Interestingly, studies on laser surface hardening of H13, a process with similar rapid solidification rates, report significant segregation of alloying elements at these boundaries [120]. Higher VED and lower scanning speed values promote increased segregation rates due to elevated temperatures and enhanced atomic movement, facilitating the formation of segregated regions [110, 121].

The balling effect, a significant concern in PBF, is particularly pronounced in H13 tool steel due to its inherent material properties – low viscosity and high surface tension [122]. This phenomenon arises when surface tension causes the molten metal track to shrink and form droplets rather than a uniform layer, leading to defects like impurities, lack-of-fusion, and porosity, ultimately contributing to poor surface quality [123, 124]. Four main factors contribute to balling in H13: (i) Wettability - poor compatibility between molten metal and the substrate hinders spreading (high contact angle) and promotes balling. Adjusting process parameters like laser power and scan speed can improve wettability [124]. (ii) Plateau-Rayleigh Instability - surface tension can break liquid cylinders formed during PBF into smaller droplets. Factors like laser wavelength and initial droplet size influence this instability [125]. (iii) Thermodynamic factors - surface tension inherently drives molten metal to minimize its surface area, leading to ball formation during rapid cooling [124]. (iv) Dynamic factors - faster spreading compared to solidification helps prevent balling. Optimizing process parameters to control these factors is essential for mitigating balling and achieving a high-quality surface finish in PBF-ed H13 components [124]. Wang Di et al. [126] delved deeper into understanding balling formation in 316L stainless steel PBF by considering the cumulative effect of energy input. This cumulative effect is influenced by two key factors: the overlap rate of laser tracks and the heat buildup value (Ea). The formula (Eq.2) calculates Ea, which takes into account laser power (P), spot diameter (d), scan speed (v), and a heat accumulation factor for multi-track layers (ε). Notably, Ea is dynamic and changes throughout the process due to factors like the ratio of P/v, the scanning area of each layer, and cooling rate. As the PBF process progresses with multiple layers, the cumulative heat accumulation increases the overall energy input. This can cause the laser track to transition from a uniform spread to irregularly shaped particles, leading to balling. The study suggests using lower laser power or higher scan speed as potential strategies to mitigate balling formation.

$$\psi 3 = \frac{4P}{\pi d^2 . v}(1 + \varepsilon) + E_a \qquad \textit{Eq.2}$$

Other research on the balling effect in stainless steel and nickel powder has yielded contrasting findings regarding the influence of processing parameters. Studies have observed that higher scan speeds and lower laser powers tend to accelerate balling, while hatching distance appears to have minimal impact. Additionally, thicker layers can increase the likelihood of balling by reducing the overall energy input. Conversely, a scanning strategy that involves remelting the printed layer has been shown to be effective in preventing balling formation [123]. The critical volumetric energy density required to avoid balling in Mg alloy is reported to be between 133.9 and 187.5 J/mm^3 [124]. This value is significantly lower at 77 J/mm^3 for AZ91 [124]. Furthermore, Dongdong et al. [127] identified splashing of molten material at high scanning speeds as another factor contributing to the formation of small balls on the PBF-ed surface.

Limitations are currently recognized in the understanding of PBF for H13 tool steel, particularly regarding the influence of process parameters on factors such as porosity, balling formation, mechanical properties, and microhardness. Valuable insights into PBF have been provided by previous research, but material-specific data for H13 is necessary for optimal process development. This study addresses this gap by investigating the effects of VED on relative density, porosity evolution, balling formation, elemental segregation, their relationships with the mechanical properties of PBF-ed H13 components, and the resulting microhardness. It is expected that by elucidating these relationships, optimal VED parameters will be established that minimize defects like porosity and balling. Ultimately, this will lead to the production of high-density H13 components with superior mechanical properties and microhardness.

2.1.3 **Materials and methods**

2.1.3.1 Materials

In this study, a gas atomized H13 hot work steel powder with a particle size ranging from 15-50 μm was utilized. The shape and size distribution of the H13 powder were illustrated by the SEM image presented in Figure 16, revealing spherical powder particles with a mixture of larger and smaller particles. An optimal combination of size and shape for achieving maximum packing density was provided by this distribution. The detailed chemical composition of the initial powder is provided in Table 7.

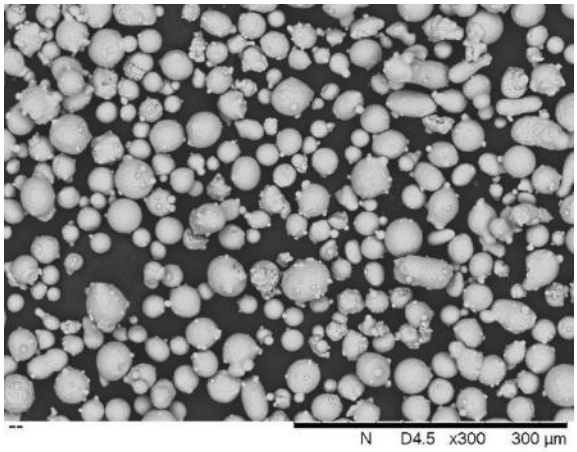

Figure 16 . SEM image of the H13 powder

Table 7. Chemical composition of the initial powder

Elements	Fe	Cr	Mn	Mo	Si	V	C	Others
Min(wt.%)	Bal.	5.0	0	1.0	0.5	0.5	0.3	0
Max(wt.%)	Bal.	6.0	0.6	2.0	1.0	2.0	0.5	0.05

2.1.3.2 Experimental Methods

The samples were fabricated using the EOS M290 machine, which utilized a single continuous wave (CW) ytterbium-fiber (Yb-fiber) laser with an operating wavelength of

approximately 1µm and a maximum power output of 400W. Argon (Ar) gas was employed to prevent oxidation during the process. Printing was conducted on a steel substrate, with a rotation strategy of 67° per layer and a consistent layer thickness of 50 µm. Notably, no preheating was applied in this process. Subsequent to printing, the samples underwent stress-relieving heat treatment at 650 °C for 8 hours, followed by a furnace cooling process to eliminate residual stress, as recommended by literature [28, 30]. The samples were printed in accordance with ASTM standards for tensile testing. The primary variables under investigation included laser power (P), scanning speed (V), and hatching distance (H). Detailed experimental setups, along with the calculated volumetric energy density (VED) determined using Eq.3, are provided in Table 8.

$$\mathbf{VED} = \frac{\mathbf{P}}{\mathbf{VHt}} \qquad \text{Eq.3}$$

Table 8. Design of the experiment

Sample code	Printing strategy (°)	Laser power (W)	Laser Speed (mm/s)	Hatch distance (mm)	VED (J/mm^3)
S1	67	250	750	0.10	67
S2	67	250	800	0.12	52
S3	67	250	850	0.14	42
S4	67	275	750	0.12	61
S5	67	275	800	0.14	49
S6	67	275	850	0.10	65
S7	67	300	750	0.14	57
S8	67	300	800	0.10	75
S9	67	300	850	0.12	59
SV1	67	275	800	0.12	57

The samples were subjected to a thorough preparation process, which included precise cutting, polishing, and etching using Carpenter etchant for approximately 10-45 seconds. Before and after etching, the samples were closely examined using optical microscopy and scanning electron microscopy (SEM) to understand their porosity, microstructure, and oxide size. Vickers microhardness (HV200) was assessed by applying a 200-gf load at 225 points arranged in a 15x15 square pattern, with each point spaced approximately 250 µm apart. To understand the mechanical properties, a series of tensile tests were conducted following

ASTM E8 standards for subsize samples. These tests were performed on the MTS810 machine at room temperature, applying a controlled strain rate of 0.0025 1/s. Throughout the tests, the samples were ensured to be subjected to tension perpendicular to their building direction. Surface roughness measurements were performed using the Mitutoyo SV-C3100 machine, capturing areal surface topography values. The roughness parameters Ra, Rq, Rp, and Rv were assessed for each surface. Ra, or average roughness, was utilized to analyze the arithmetic mean of height deviations from the mean line across the evaluation length. The reported values were derived from the average of five repetitions, ensuring accuracy and reliability in the analysis.

2.1.4 **Results and discussion**

2.1.4.1 Porosities characterization; size, quantity, and location

The samples' approximate relative density was determined through image analysis, revealing that all samples exhibited a relative density of approximately 99% or higher, with minor variations among them (Figure 17-a). Generally, the relative density increased from 42 to 75 J/mm³, with exceptions for samples 7 and 4 at VED values of 42 J/mm³ and 61 J/mm³, respectively. This phenomenon was further investigated through the characterization and analysis of common porosity types observed in PBF, including LOF, keyhole (elliptical form), and gas porosity (rounded). Figure 17-b and Figure 17-c systematically illustrate the changing trend of gas porosity size and number with increasing VED, while Figure 17-d and Figure 17-e depict the variations in keyhole porosity size and number with increasing VED, respectively. The characterization revealed that as the VED value increased up to 57 J/mm³, both the size and number of porosities, particularly keyhole and gas porosities, increased. In contrast, LOF was eliminated at this threshold. Consequently, for VED values below 57 J/mm³, the main factor driving the increase in relative density was the reduction in LOF, despite the notable rise in the number and size of keyhole and gas porosities.

For VED values greater than 57 J/mm³, the occurrence of LOF ceased, and there were no consistent changes observed in the size and number of gas and keyhole pores as VED increased. However, at a specific VED value of 59 J/mm³, a significant finding emerged: the absence of keyhole pores and the presence of smaller, evenly distributed gas pores throughout the sample, typically measuring around 13 µm. This discovery is in line with the concept proposed by Rezaeifar et al. [128], suggesting the existence of a "safe zone" during the PBF process for each material. When the VED fell below this safe zone, there's a risk of LOF formation. Conversely, when the VED exceeded this range, there was a possibility of keyhole formation. With this information, VED of 59 J/mm³ fell into safe zone. It is noteworthy that this categorization of VED for porosity formation near the surface may not have held true for the middle of the samples, as illustrated in Figure 17-e. For VED values less than 57 J/mm³, LOF occurs. In the range of 57-59 J/mm³, small gas porosities are possible due to gas entrapment or small keyholes at each laser track, resulting in small pores throughout the samples. Finally, for VED values exceeding 59 J/mm³, laser tracks overlap well with minimal effect from keyholes and gas in the middle of the samples. However, it's important to consider the evolution of porosity both in the middle and at the edges of the samples for a comprehensive understanding.

The results of this study were aligned with those reported by Narvan et al. [71] concerning PBF-ed H13. It has been observed that increasing the VED value up to a certain threshold, approximately 60 J/mm³, resulted in a notable increase in relative density. But, beyond this threshold, further increases in VED did not significantly impact relative density. In our study, it was revealed that at VED values as high as 80 J/mm³, there was a reduction in relative density. Specifically, VED values above 59 J/mm³, particularly in the range of 61-67 J/mm³, led to the formation of large keyholes ranging from 70-100 µm in considerable quantities, which is the main contributor to reduction in relative density.

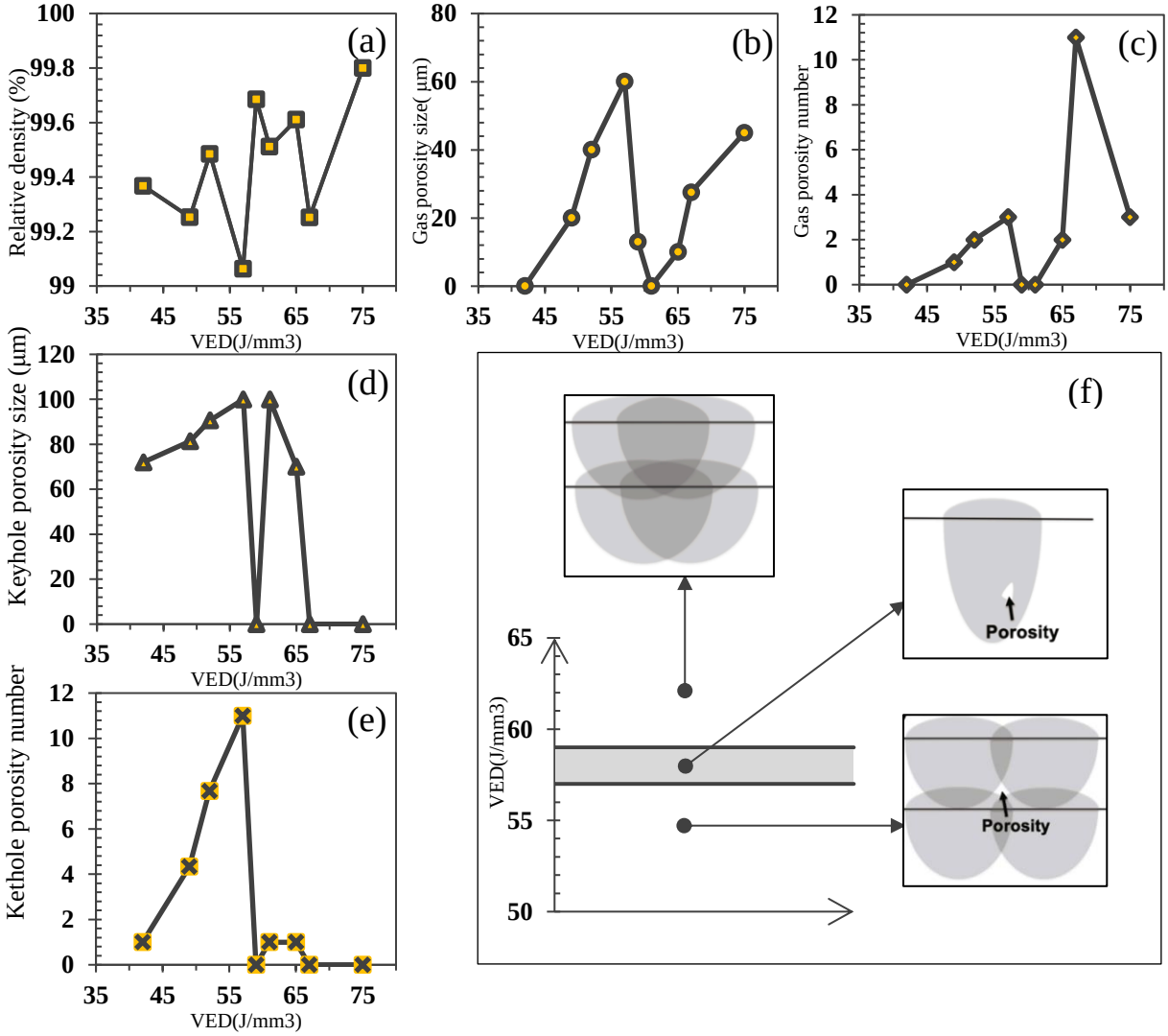

Figure 17. Porosity evolution trend with increasing the VED for samples S1-S9 (schematics are adopted from reference [129])

Previous studies haven't paid much attention to the concentration of porosities near the surface of PBF-ed metals [130-133]. This study, however, observed porosities mainly near the edges, particularly in the final printed layers and corners. The presence of gas porosities at the top of PBF-ed H13 has been attributed to the printing strategy [28]. However, in this study, all samples were fabricated using the same printing strategy. Despite this consistency, the size and number of near-surface porosities varied significantly with changes in processing

parameters. This observation suggests that printing strategy is not the sole reason for the observed edge porosity.

The concentration of pores observed near the edge of PBF-ed H13 samples is likely linked to residual stress formation. Several factors contribute to residual stress in PBF parts, particularly H13 tool steel. A key factor is the temperature gradient mechanism (TGM) inherent in the PBF process. TGM introduces a combination of compressive and tensile stress due to the high thermal gradients and shrinkage of newly added layers. The interplay between these phenomena determines the final residual stress distribution [134]. Unlike other iron alloys, which typically experience tensile stress, PBF-ed H13 exhibits a unique pattern. Its residual stress transitions from tensile to compressive stress along the building direction. Notably, the final layers experience a significant volume of compressive residual stress [135-137]. Yan et al. [138] and Narvan et al. [139] reported substantial compressive stress in PBF-ed H13, ranging from 940 to 1420 MPa and around 1000 MPa, respectively. This compressive stress originates from the martensite phase transformation during rapid cooling, causing a 4% volume expansion and subsequent compressive stress [140]. The presence of this high-volume compressive residual stress in near-surface layers creates favorable conditions for gas expansion. This, in turn, could hinder gas entrapment and formation within the interlayer regions, potentially explaining the observed concentration of pores near the edge. In addition to residual stress, other factors also facilitate gas porosity formation and expansion. First, thermal heat accumulation at the last layers provides ample opportunities for gas expansion. Additionally, the higher thermal gradient between the center and the melt pool boundary, particularly at the corners of the last layers, affects Marangoni convection flow, which can promote porosity formation in general. This Marangoni flow might also be linked to the creation of keyhole porosities specifically. This phenomenon suggests a complex interplay between the processing parameters and material properties in generating gas and keyhole porosities during the printing of PBF-ed H13 parts.

2.1.4.2 Microstructural observation

Microscopic examination of samples etched for short durations (aligned with the build direction) revealed consistent features. Notably, the grains displayed a preferred orientation towards the heat source (build direction). This aligns with established knowledge of directional solidification during additive manufacturing processes. As shown in Figure 18-a, this directional alignment extends from the center of the melt pool towards its boundary, or "laser track." Furthermore, SEM images (Figure 18-b and Figure 18-c) revealed a partially distorted, cellular austenitic microstructure. The cellular walls exhibited evidence of microsegregation, indicating higher concentrations of alloying elements in these regions [141]. Importantly, the heat treatment process did not significantly alter these microsegregation patterns, indicating that the cellular austenitic microstructure remains largely unchanged. This aligns with findings reported in the literature for PBF-ed steels, where the rapid cooling inherent in the process typically results in a cellular microstructure as the initial (as-built) condition [138].

In contrast, samples etched for longer durations revealed the presence of non-metallic inclusions primarily at the melt pool boundary within the laser track (Figure 18-d). In some instances, these inclusions originated at grain boundaries within the laser track, as shown in Figure 18-e. These inclusions varied in size and distribution across all samples.

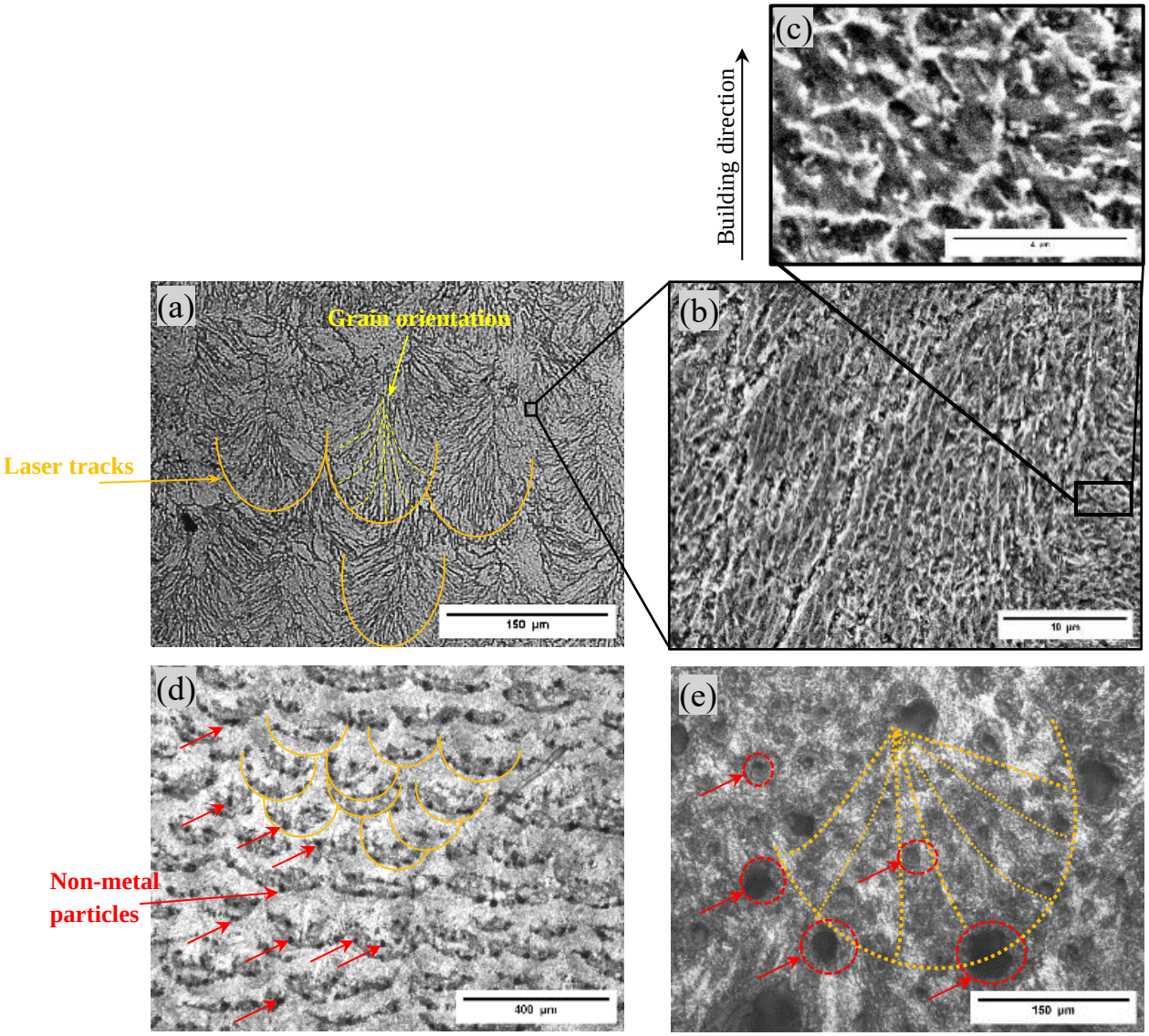

Figure 18. Microstructural characterization of PBF-ed H13 samples: (a) OP image at low magnification with 10s etching, (b) SEM image with 10s etching, (c) higher magnification of SEM image with 10s etching, and (d) OP image magnification with 30s etching, and (e) OP image at higher magnification with 30s etching (carpenter etchant)

The analysis of particle size and shape focused on samples with VED exceeding 57 J/mm^3. Samples with lower VED values, typically exhibiting LOF defects, were excluded to optimize processing parameters without the influence of LOF. The examination of particle size revealed no clear trend, suggesting a complex relationship between particle size and

VED (Figure 19). Interestingly, the observed particle sizes varied across the samples, ranging from a minimum of approximately 1.5 μm observed in sample S7 (57 J/mm^3 Figure 19-a) to a maximum of around 50 μm observed in sample S9 (59 J/mm^3 Figure 19-e).

Furthermore, samples with VED below 67 J/mm³ displayed a relatively uniform particle distribution within the matrix. However, samples exceeding this threshold exhibited a shift towards non-uniform oxide formation. This was evident as clustered particle distributions, particularly in sample S8 (Figure 19-c) with the highest VED (75 J/mm³). This finding aligns with previous research [94] that documented unstable melt pool behavior at VED levels nearing 80 J/mm³. This instability likely contributes to the observed non-uniform oxide distribution at higher VED, suggesting a potential correlation between elevated VED and a non-uniform microstructure.

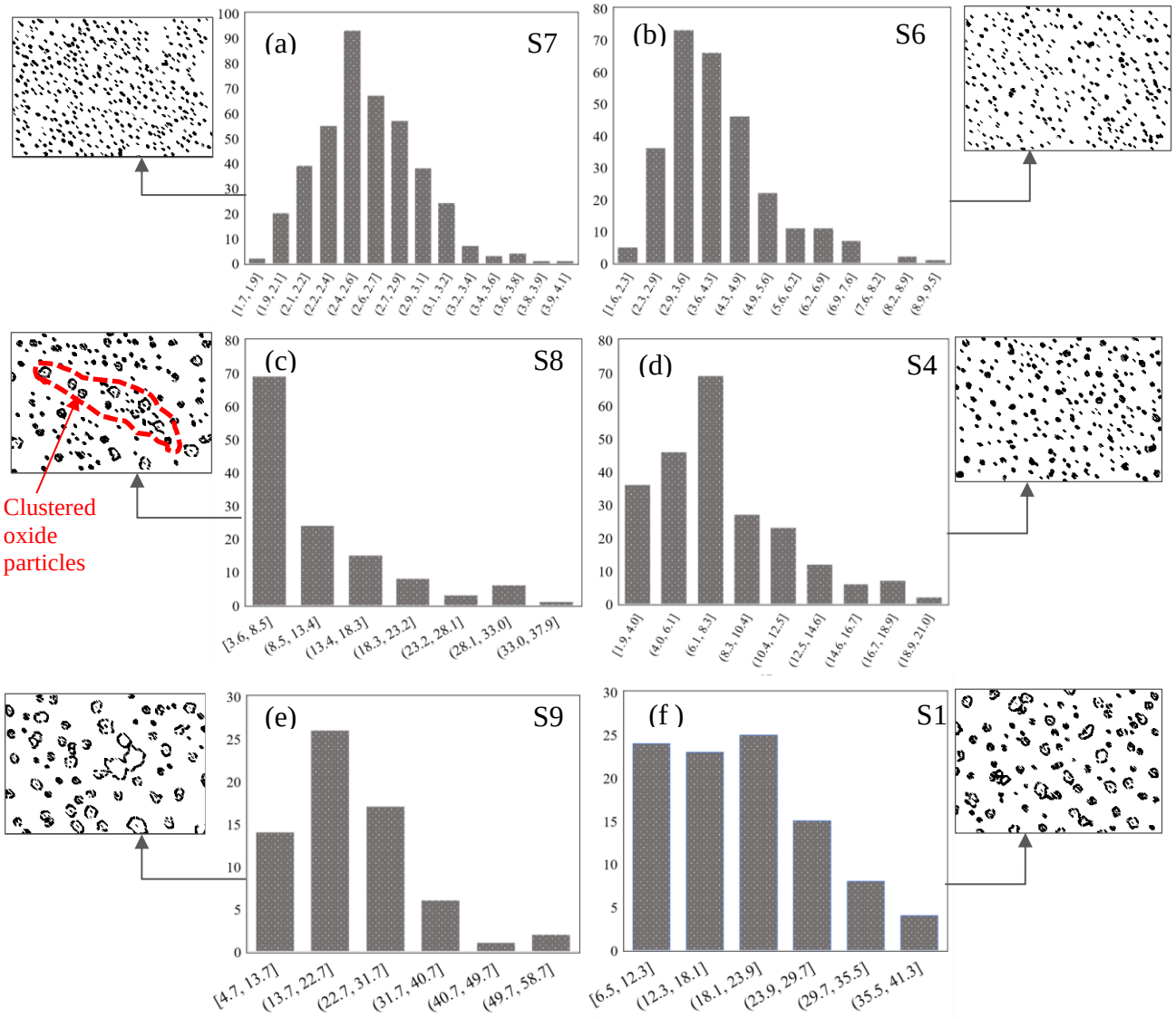

Figure 19. Particle size distribution and shape analysis

Figure 21, presents SEM images of three samples showcasing particles with varying sizes: one with a mid-range size (Figure 21-a), another with the minimum size (Figure 21-b), and the third with the maximum size (Figure 21-c). These samples correspond to VED values of 42 J/mm³, 57 J/mm³, and 59 J/mm³, respectively. SEM-EDS elemental mapping of the samples at a VED of 59 J/mm^3 indicated that these particles were oxides (Figure 21-d), with the highest oxygen concentration found in regions of the particles (as depicted by the green

oxygen elemental map in Figure 21-d. Interestingly, the chromium concentration in the area where the oxide particles were separated (Figure 21-e) suggests that these particles are likely not chromium oxides. Subsequently, XRD mapping of the sample at a VED of 59 J/mm^3 confirmed that these particles primarily consist of molybdenum oxide, manganese oxide and small peaks of silicon oxide (MnO_2, Mo_9O_{26}, and SiO_2). According to the Ellingham diagram at a temperature of 650 °C, Si, Mn has a strong affinity for oxygen compared to chromium's affinity for oxygen. Furthermore, the XRD revealed the presence of silicon carbide (Si_5C_3), which corresponded to the findings in the elemental map. The XRD pattern of all samples exhibited negligible differences at different VED values with the ferrite phase remaining as the dominant phase identified in all the samples, with no presence of austenite or martensite. This aligns with the findings by previous research, which proved that after a heat treatment at this temperature, the material primarily consists of ferrite phase [142]. The minor variations in XRD patterns are attributed to the type of oxides and carbides presented in the material. For instance, in samples with VED values of 59 J/mm^3 and 75 J/mm^3, where the maximum oxide particles were observed, the XRD pattern (Figure 21-e) indicated the same types of oxides for both materials (MnO_2, Mo_9O_{26}). Additionally, upon inspection of the sample with VED 59 J/mm^3, small peaks of SiO2 were detected, which were not present in the sample possessing a VED of 75 J/mm^3. In the remaining samples, the oxide particles identified were mainly MnO_2, SiO_2, and molybdenum oxide with similar stoichiometric ratios such as Mo_8O_{23}, and Mo_9O_{26}. The carbides present included chromium carbides and silicon carbides, each with varying formulas, such as Si_5C_3 and $Cr_{23}C_6$, and Cr_7C_3. In certain samples, the presence of vanadium carbide peaks was also detected, consistent with prior research [48].

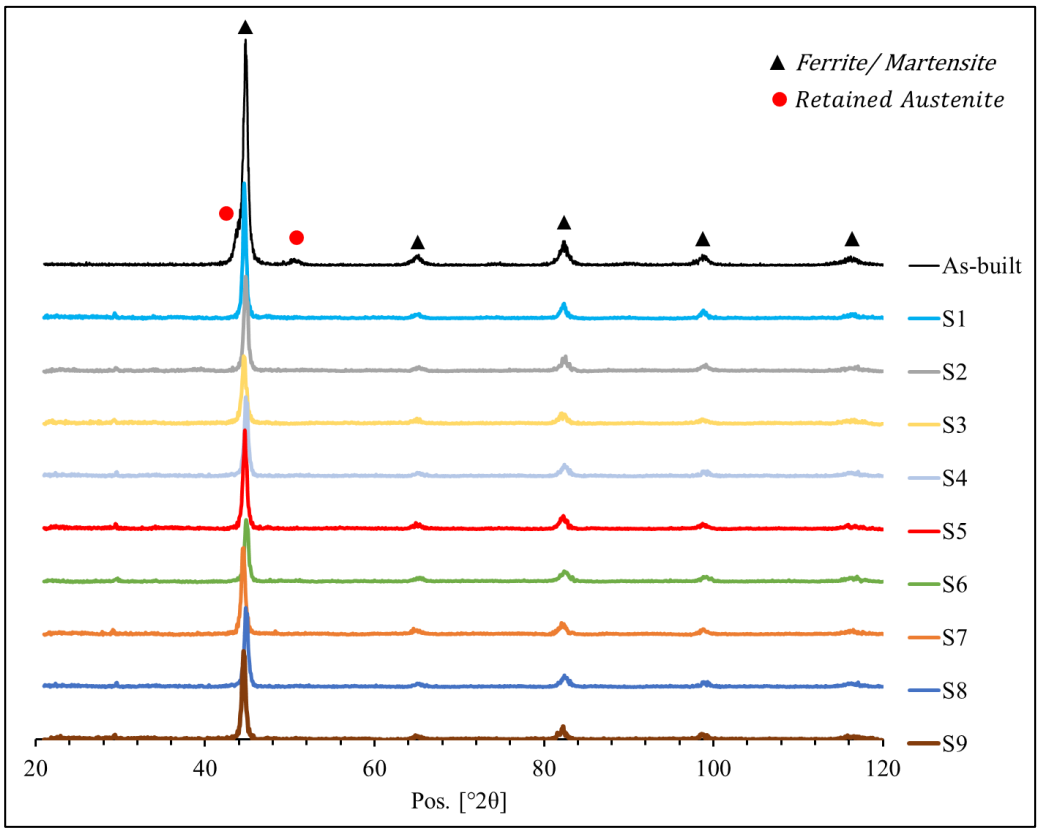

Figure 20. XRD results

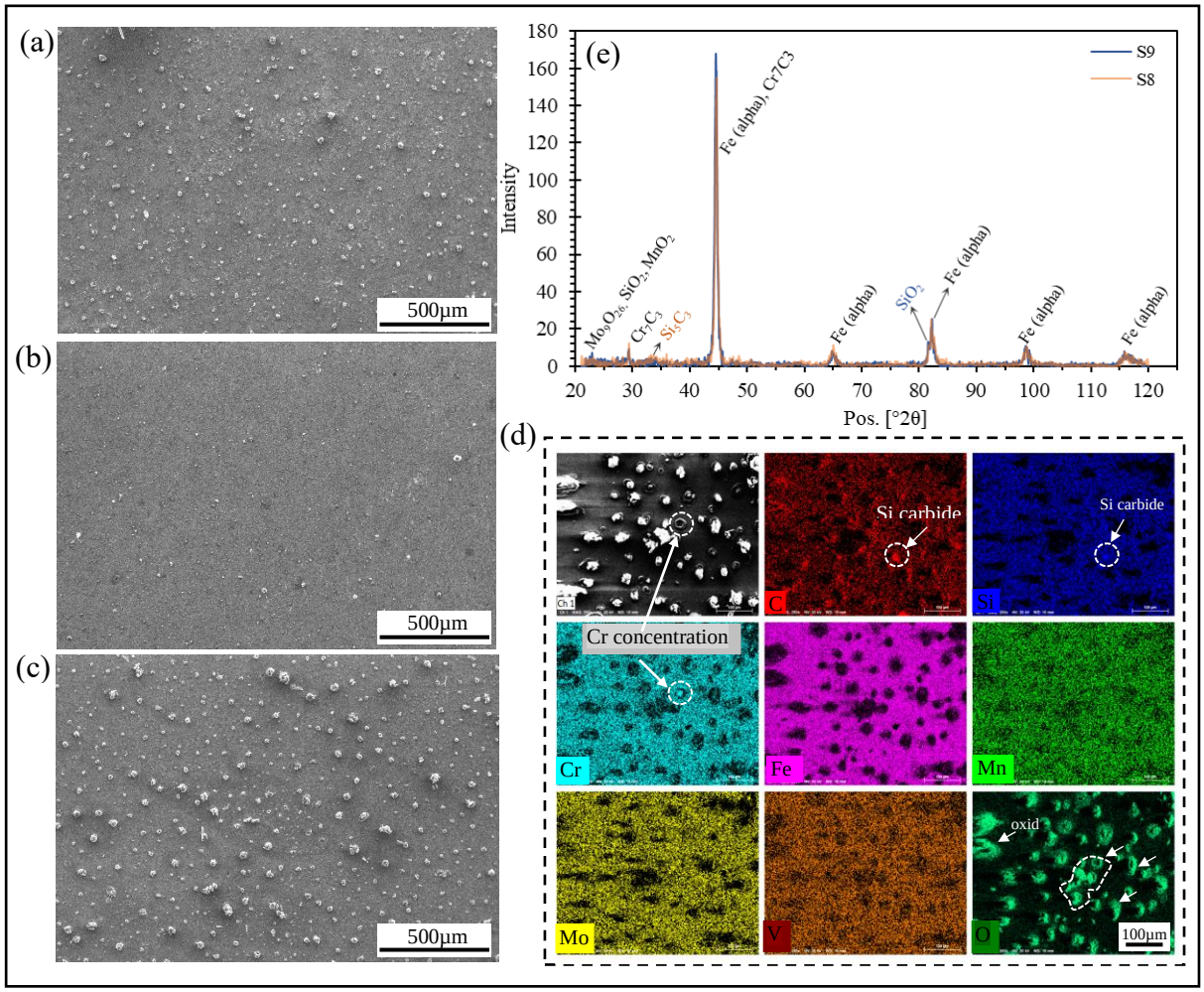

Figure 21. Characterization of the observed particles at different VEDs for samples containing (a) mid-size range, (b) smallest observed size, (c) the largest observed size, alongside (d) their elemental EDS analysis and (e) the XRD pattern analysis

The existence of oxide particles following heat treatment is a topic that has not been studied extensively. This lack of observation is likely due to the hiddenness of these oxide particles when samples are subjected to a shorter etching time. As it has been shown in Figure 18-e these oxide particles predominantly form at the end of the laser track. The presence and pattern of oxide formation can be explained by a recent research conducted by Xie et al. [120]. The study focused on laser surface remelting of H13 steel under an argon atmosphere and demonstrated the formation of an oxide layer with varying thickness, reaching up to 60 µm on top of the melt pool in the laser track. Furthermore, mesoscopic segregation of

alloying elements within the laser track was observed, with the alloying elements tending to accumulate at the boundary of the melt pool. Therefore, the oxide particle observation can be explained in two ways. Firstly, the oxide formation on top of the laser track in each layer could be one source of oxide particle presence. Secondly, the oxide particles at the end of laser track can be attributed to mesoscopic segregation, where alloying elements that are more prone to oxidation exhibit higher concentrations. This phenomenon may not prominent for as-built sample, but when the material is subjected to elevated temperatures for a long time, the oxide particles find enough time to grow. As such, it could be concluded that the presence of these oxide particles is an indicator of elemental segregation, which indicates microstructural inhomogeneity within PBF-ed H13. Larger oxide sizes are indicative of more pronounced segregation and less microstructural homogeneity.

2.1.4.3 Balling formation

Optical microscopy revealed balling effect formation on different sample surfaces, such as the side surface and the last printed layer. Notably, the formation on the surface around the building direction (in contact with the powder bed) differed significantly from that on the last printed layer in all samples Figure 21 illustrates these formations.

Figure 22-a shows the surface along the building direction, with small balls attached to the surface, similar in size to the initial powder particles. This attachment is likely due to particle melting in the powder bed and subsequent attachment to the surface. Additionally, Figure 22-a displays balling formations resulting from the dynamics of the melting pool (such as Marangoni flow or surface tension effects). Figure 22-b depicts the last printed layer with no adhering powder but still small balls on top. This could be due to splashing of the melting pool during the process, along with balling formation from the melting pool dynamics, similar to the side surface. Figure 22-c and Figure 22-d provide a closer look at the edges of the printed samples, showing varying degrees of balling, from severe to minimal, and emphasizing the effect of balling formation on surface roughness. Higher roughness is

observed in samples with severe balling formation, characterized by the presence of larger balls on the surface.

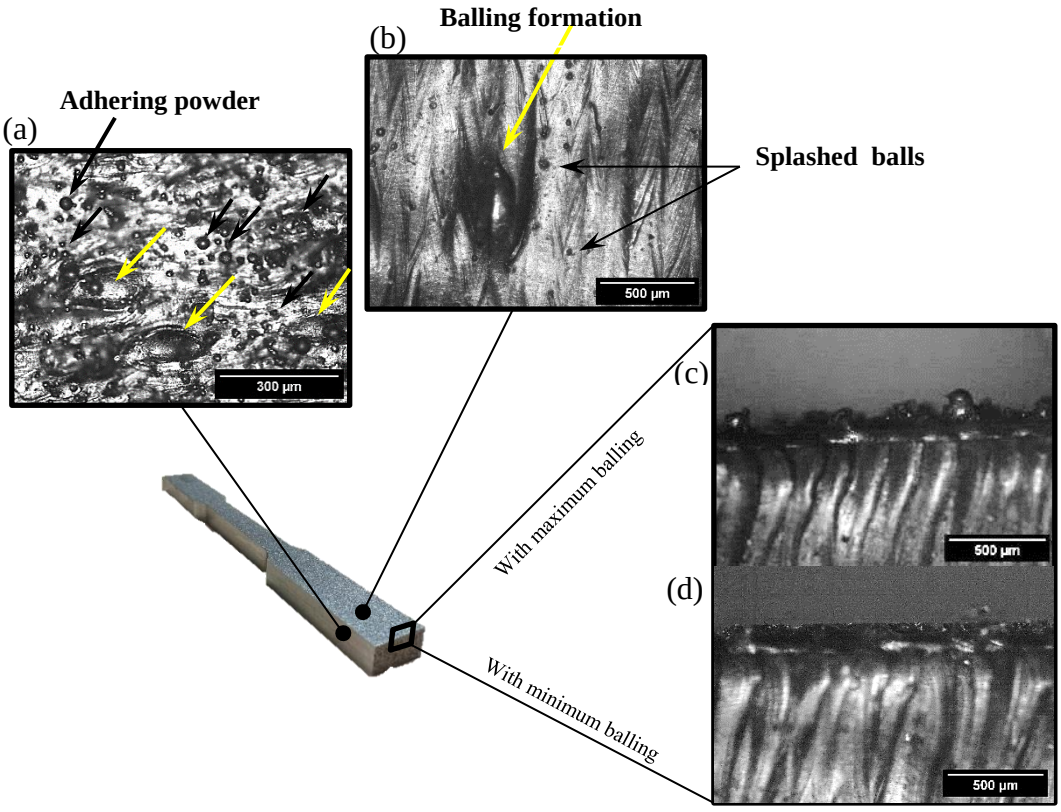

Figure 22. Optical microscopy of the effect of big balling effect phenomenon in different surfaces of the samples including (a) around surface, (b) last layer, and (c), (d) edge of the samples. Yellow arrows noticing the balling effect, and black arrows notcing the splash balls and adhering powder

The presence of balling formation is consistently observed across all samples. However, it's essential to recognize that the size and pattern of this phenomenon are significantly influenced by the selected processing parameters. Three distinct types of balling effects have been identified. Firstly, material splashing results in particles measuring less than 13 µm, visible across all samples and resembling small, rounded pores (Figure 22-b). These splashed particles may contribute to the overall porosity of the samples. Secondly, a continuous laser track represents the second type of balling effect (Figure 23-a), while the third type is characterized by disrupted laser tracks and the formation of larger balls (Figure

23-c). These distinct balling effects have minimal impact on overall sample porosity. However, it's noteworthy that the third type, prevalent at higher VED levels (75 J/mm³), significantly increases surface roughness, warranting further investigation.

Regarding the influence of VED on balling formation, existing literature suggests a relationship between VED and the balling effect within the laser track. Increased VED leads to higher temperature and viscosity, typically reducing the occurrence of balling phenomena. This study's findings support this relationship, as balling formation decreases when VED is increased from 42 J/mm³ to 57 J/mm³. Specifically, Figure 23-a illustrates uniform balling formation for a sample built with a VED of 49 J/mm³, which is eliminated by increasing VED to 57 J/mm³, as shown in Figure 23-b. Notably, Figure 23-b depicts minimal balling formation, indicating a reduction in this phenomenon at a VED of 57 J/mm³. However, beyond this threshold, the correlation between VED and balling becomes more complex, with no specific trend. Overall, minimal balling formation is observed at a VED of 57 J/mm³. Conversely, severe balling formation occurs at a VED of 75 J/mm³, where samples exhibit the formation of powder particle islands and notably larger balls (Figure 23-c).

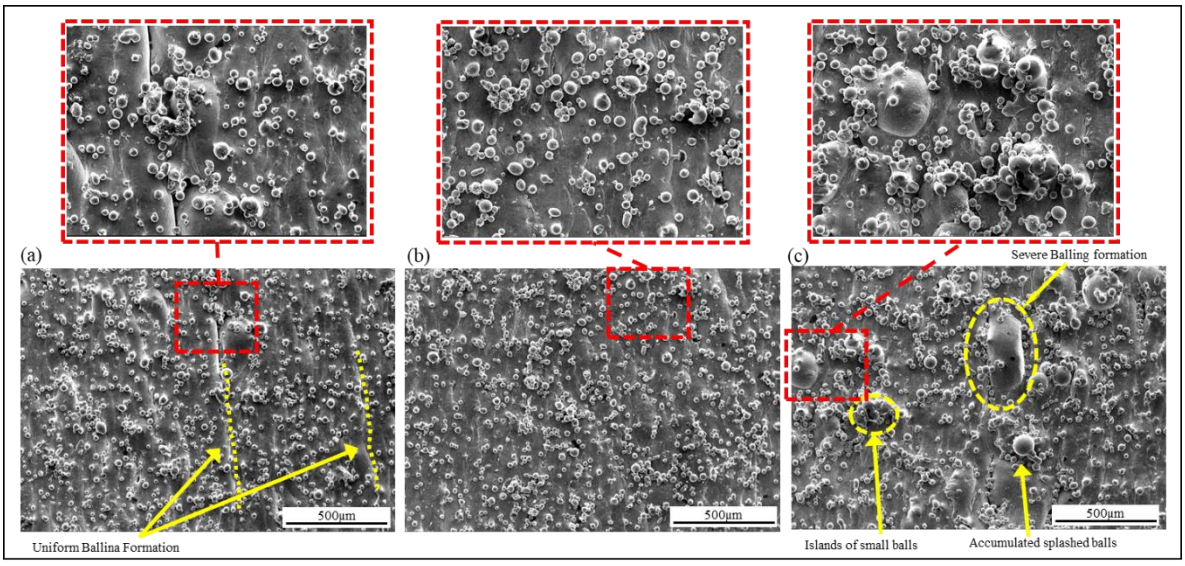

Figure 23. SEM image of the samples indicating different types of the balling formation on the samples at (a) low VED of 49 J/mm^3, (b) mid VED of 57 J/mm^3, and (c) high VED of 75 J/mm^3

For better comprehension of how various balling formations affect the final surface quality, areal surface topography values are provided in Table 9. These values offer insights into surface characteristics both around the surface (referred to by the building direction, depicted in the XZ-z) and on the last printed layer (shown in the XY plane). Remarkably, the changing trends in values exhibit similarity between these two surfaces. Figure 24 illustrates the changing trend of surface roughness (Ra) measurements with varying VED.

As the VED increases, changing in the Ra values, indicating a non-linear relationship between VED and Ra. Specifically, as VED rises from 42 J/mm³ to 52 J/mm³, there is a noticeable decline in Ra, suggesting a smoothing effect on the surface. This trend is further exemplified by the minimum Ra value of 1.75 µm observed at VED 52 J/mm³. However, as VED continues to increase beyond this threshold, the Ra values fluctuate, with occasional spikes observed. Notably, at VED 59 J/mm³, we observe a substantial increase in Ra to 3.66 µm, marking the highest surface roughness among the data points. This elevated Ra value suggests a deviation from the previously observed smoothing effect.

Upon comparing the Ra values at building direction and last printed layer (Figure 24-b, and Figure 24-c) with the observed balling formations in the samples, a clear relationship emerges, particularly in case of severe balling formation. Notably, at VED values where severe balling is prevalent, we also observe maximum roughness on the surface. For instance, at VED 75 J/mm³, where severe balling formation is prominent, the corresponding Ra value reaches its highest point in the dataset, measuring 2.90 µm. This indicates a direct correlation between the extent of balling formation and surface roughness, suggesting that increased balling leads to rougher surface textures. Conversely, at VED values associated with minimal balling, such as VED 52 J/mm³, the Ra value decreases significantly to 1.75 µm, indicating smoother surface characteristics.

Table 9. Areal surface topography values

Set	Xz-z				XY			
	R_a (µm)	R_q (µm)	R_p (µm)	R_v (µm)	R_a (µm)	R_q (µm)	R_p (µm)	R_v (µm)
1	1.75	2.27	5.09	5.35	1.19	1.46	2.88	3.06
2	1.75	2.18	4.58	4.62	1.13	1.42	3.67	2.39
3	2.51	3.05	5.57	5.98	2.34	3.10	6.61	4.34
4	2.09	2.61	5.49	5.24	1.52	1.86	3.52	3.04
5	2.28	2.80	5.62	5.91	1.76	2.11	4.86	3.29
6	2.30	2.94	5.52	6.08	1.84	2.29	5.17	3.33
7	2.23	2.72	5.04	5.72	1.50	2.19	4.29	3.09
8	2.90	3.57	7.00	6.67	2.95	3.48	5.90	5.01
9	3.66	4.58	8.73	9.14	2.78	3.33	5.35	5.13

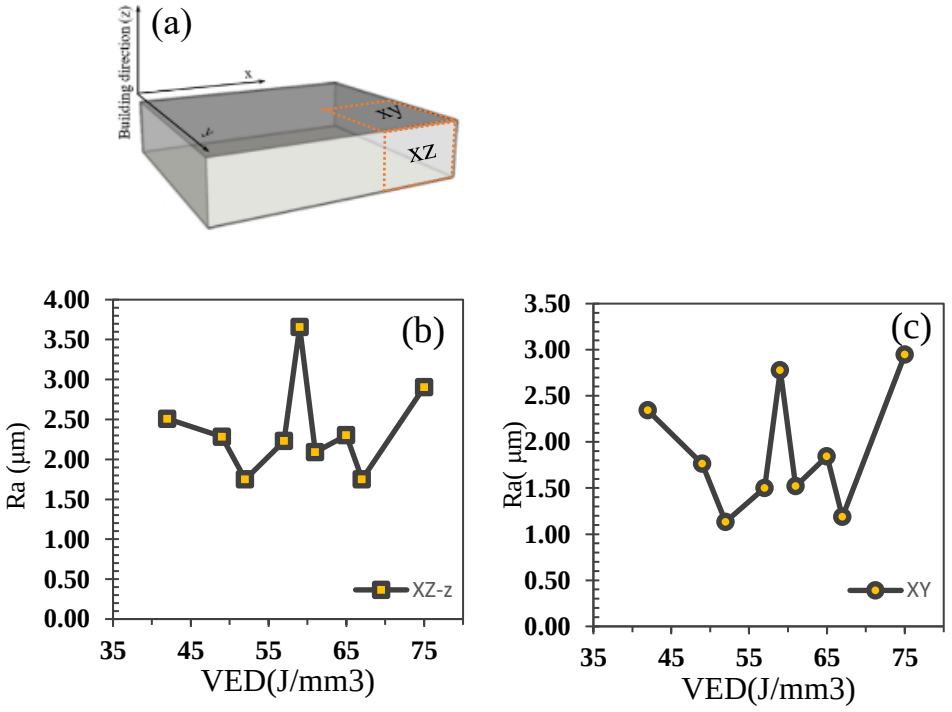

Figure 24. Surface roughness analysis (a) direction, (b) variation of Ra with respect to VED for surface around, and (c)the last printed layer

While a direct correlation between the VED and the balling formation remains obscure, SEM observations reveal a notable relationship between oxide particle size, which reflects the pattern of segregation, and balling formation, as depicted in Figure 25. For instance, S7, exhibiting minimal balling effects, displays the smallest oxide particles, uniformly

distributed at sizes under 3 µm (Figure 25-a and Figure 25-d). In contrast, S9, characterized by severe, yet uniform balling formation (Figure 25-b), shows uniformly distributed significantly large oxide particles less than 60 µm (Figure 25-e). In the case of S8, with severe and non-uniform balling formation (Figure 25-c), the large and elongated balls on the surface correspond to a similar pattern of clustered oxide formation (Figure 25-f and Figure 25-g). Overall, the data highlights that at significantly high VED (75 J/mm³), the material experiences an increased level of inhomogeneity in elemental segregation. This non-uniform segregation results in a non-uniform distribution of oxides. Furthermore, the clustered carbides at VED of 75 J/mm³ indicate an unstable melting pool.

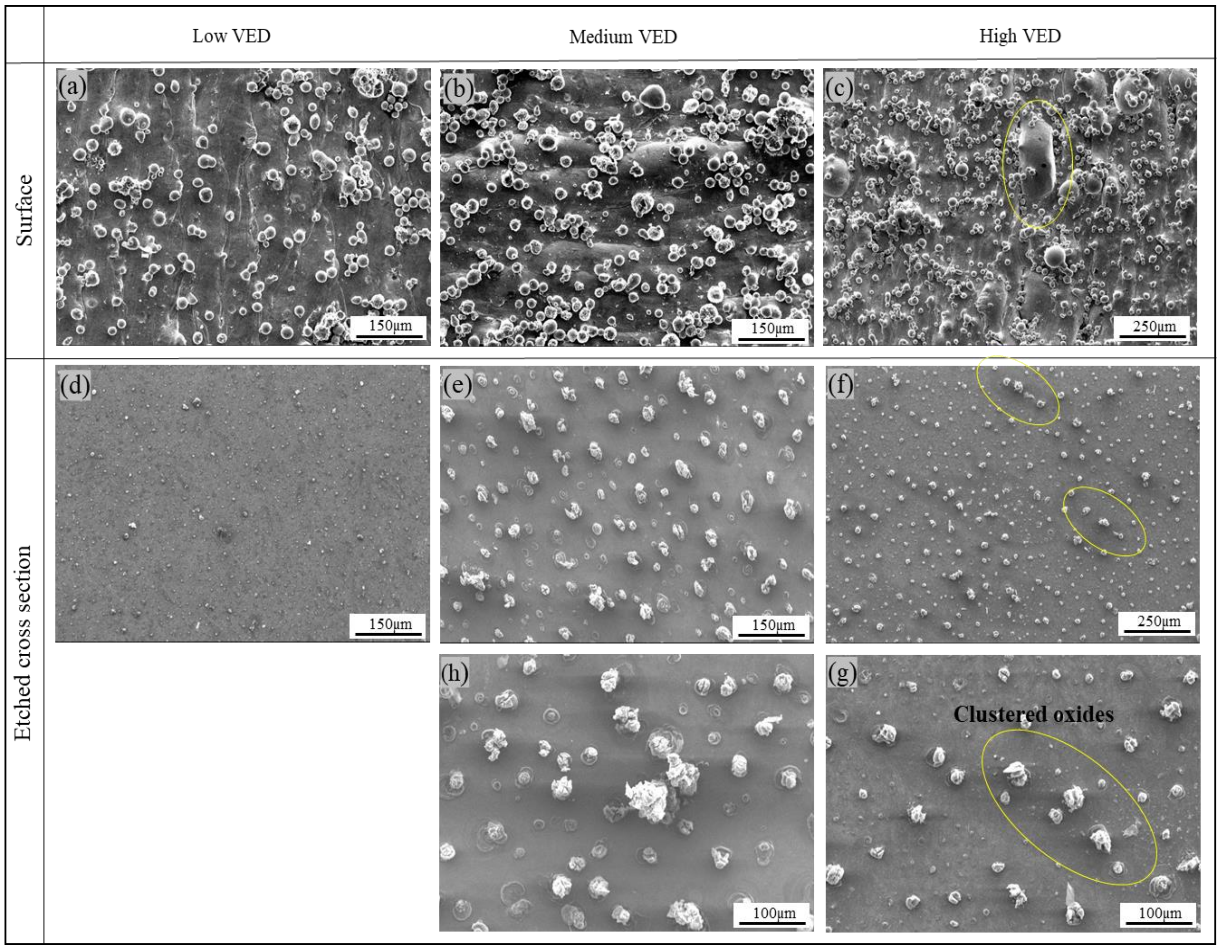

Figure 25. SEM images illustrating balling and associated oxide formation in samples with Varying VEDs: (a) and (d) VED of 57 J/mm^3, (b),(e) and (h) VED of 59 J/mm^3, and (c), (f), and (g) VED of J/mm^3

2.1.4.4 Tensile behavior

The mechanical strength of PBF-ed H13 in this study was influenced by residual stress, Oxide particles, and porosity defects. Assuming all the compressive residual stress is removed during the heat treatment process, the mechanical properties of the samples are mainly attributed to the oxide size and porosity type and locations.

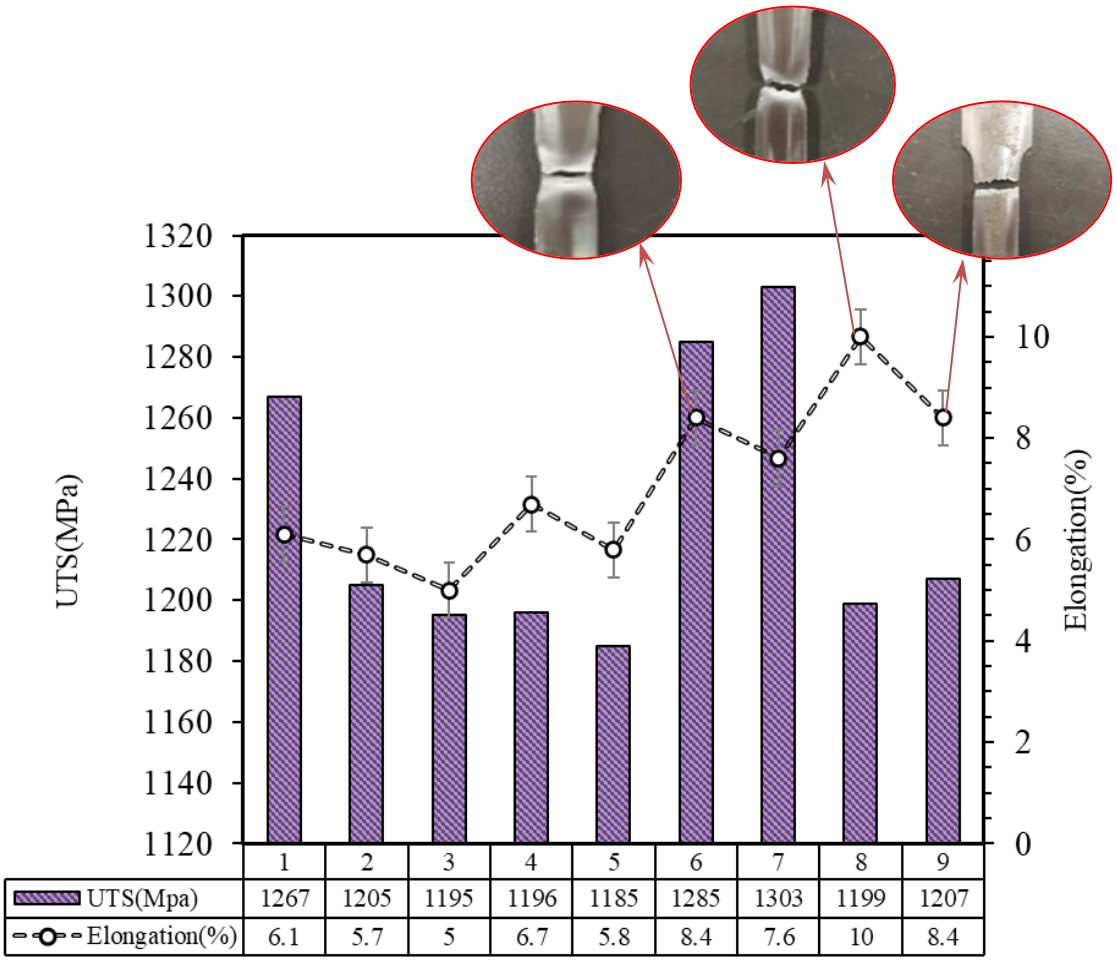

	1	2	3	4	5	6	7	8	9
UTS(Mpa)	1267	1205	1195	1196	1185	1285	1303	1199	1207
Elongation(%)	6.1	5.7	5	6.7	5.8	8.4	7.6	10	8.4

Figure 26. Tensile test result of the samples S1 to S9

Tensile test results, presented in Figure 26, reveal an interesting deviation from established understanding. While previous literature often associates maximum density with optimal mechanical properties through VED optimization, the current study suggests that for

H13 steel, this might not be the sole determinant of achieving peak mechanical performance. The results highlight the significant impact of segregation and oxide formation due to marangoni flow during the laser track solidification, as well as near-surface defects, for specific VED values. Increasing the VED up to a certain value, due to which LOF is eliminated, proves to be a suitable criterion for enhancing the mechanical properties of PBF-ed H13. However, for VED values exceeding this threshold (49 J/mm^3 in this study), the phenomenon becomes more complex, with the mechanical properties resulting from the combined effects of surface defects and segregation of alloying elements during solidification, which has been shown to be correlated with the balling phenomenon at higher VED (Figure 25).

A comparison of samples S9 and S8 revealed the presence of defects near the surface of S8. Despite having a higher relative density compared to S9, S9 exhibited a higher ultimate tensile strength (UTS) due to the absence of these near-surface defects. However, S9 also contained significantly larger carbides compared to the average size in S8, potentially making it more susceptible to fracture. In this case, the detrimental effect of the near-surface porosity in S8 outweighed the strengthening effect of its higher relative density and smaller oxide size. These observations highlighted the importance of the size of near-surface defects. Notably, the keyhole size played a key role in material destructibility. For instance, S4, with a single keyhole measuring around 100 µm, showed increased susceptibility to fracture compared to S6, where defect porosities were less than 70 µm. Any near-surface defects exceeding this size made the material more prone to fracture.

The results revealed that a delicate balance between oxide size and near-surface defects was crucial for achieving desirable mechanical behavior in the samples. Sample S6, with a VED of 65 J/mm³ and a relatively high volume of defects (10 µm of gas porosity and 70 µm keyholes), exhibited a higher UTS compared to samples with fewer defects, like S8. This seemingly counterintuitive observation can be attributed to the small volume and size of S6's carbides (uniformly distributed, less than 9.5 µm). Notably, S6 achieved the maximum UTS (1285 MPa) and displayed ductile fracture, likely due solely to the very small oxide size

observed. Interestingly, S8, with a lower volume of defects, exhibited a UTS of only 1199 MPa.

The study revealed a significant influence of oxide size on UTS, independent of elongation. Small oxides at grain boundaries restricted dislocation movement, leading to increased UTS. This was evident in the high UTS observed for samples S7 and S6, which possessed minimal oxide sizes. Interestingly, S7, despite exhibiting the highest level of surface defects, achieved the highest UTS, surpassing even S1 with fewer defects. These findings highlight the importance of segregation during solidification, which requires careful consideration in the PBF process for H13 steel to achieve the desired mechanical properties. These observations align with previous research on conventional H13 surface laser melting.

2.1.4.5 Microhardness

Figure 27 presents the results of the micro indentation test. According to previous literature, the average microhardness value for near-fully dense structures after similar post-treatment is approximately 425 HV [28] . In this study, samples with minimal porosity, such as S8, achieved an average microhardness of 410 HV200. The remaining samples exhibited slightly higher microhardness values, ranging from 420 HV200 to 443 HV200.

Microhardness values are influenced by various factors, including phase distribution, near-surface porosities, grain size and oxide particles, as investigated in this study. Since XRD patterns revealed a consistent presence of the ferrite phase in all samples, and microhardness measurements were taken from the middle, the first two factors likely had negligible influence. The remaining factors, grain size and oxide particle size, will be discussed further. Before examining the influence of oxide size and distribution on microhardness, it's important to note the similar trends observed between average microhardness, UTS, and porosity formation. For VED values below 52 J/mm³, increasing VED led to higher microhardness, possibly due to a corresponding increase in oxide size. This trend peaked at a microhardness of 440 HV200 for a VED of 52 J/mm³. However, beyond this point, a clear correlation between VED and microhardness became elusive.

An analysis of both average microhardness values and microhardness maps revealed that the maps provided more nuanced information about the material compared to average values alone, particularly for PBF-processed samples. Samples S1 and S2 exhibited the highest average microhardness (around 439-443 HV200) and contained oxides ranging from approximately 12-25 μm scattered within a matrix of smaller oxides (less than 6 μm). Similarly, Samples S3 and S5 displayed a similar oxide distribution pattern, but with smaller oxide sizes (3-13 μm). This corresponded to their closely matched average microhardness values (417-420 HV200). Samples S6 and S7, with minimal oxide sizes (less than 4 μm), also showed similar microhardness values (430-433 HV200).

However, the limitations of average microhardness became evident when comparing S8 and S4. Despite having notably different oxide sizes and distributions, both samples exhibited the same average microhardness (411-416 HV200). This similarity can be attributed to the presence of a wider range of oxide particle sizes in S8. This broader distribution resulted in a wider range of microhardness values that averaged out to a value close to S4, which exhibited less variation in oxide size. S8, with oxide particles ranging from 3.6 μm to 37.9 μm and clustered oxides, displayed non-uniform segregation patterns. In contrast, S4 possessed a more uniform distribution of oxide particles, ranging from 1.9 μm to 21 μm. This significant difference in segregation patterns, and consequently, microstructure, highlights the importance of studying microhardness maps for a more comprehensive assessment of microstructural homogeneity in PBF-processed samples.

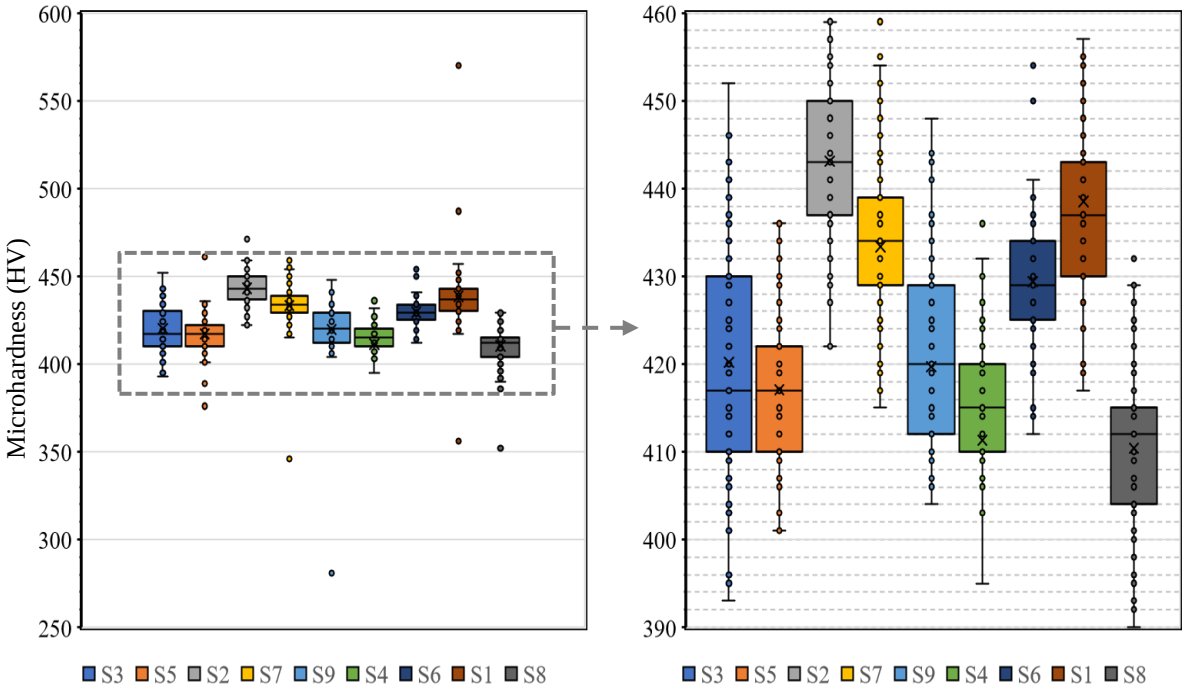

Figure 27. Micro indentation test results

The key observation from the microhardness map is the identification of a 5 µm threshold for oxide particle size for which microstructural changes are considered uniform, and material failure due to microstructural inhomogeneity is less pronounced. As expected, the observations within the microhardness map reveal a robust correlation between microhardness map uniformity and mechanical resistance. As previously explained, materials with smaller oxide particles are less susceptible to failure, a characteristic reflected in the microhardness map of the samples. Notably, S4, S7, and S6 exhibit more uniform microhardness maps compared to S9, which displays considerable variation, as illustrated in Figure 28. This relationship between microhardness variation and mechanical resistance can be explained as follows: Oxides within the material act as obstacles hindering dislocation movement. When the material is subjected to tensile forces, strain rates in different areas vary. In regions with higher resistance, strain concentration occurs, rendering the material susceptible to fractures in those areas. Samples S6 and S9 are examples of the negligible and negative effects of the presence of small and very large oxide particles, respectively. Even in the presence of near-surface porosities, S6 exhibits ductile fracture, highlighting the

negligible contribution of small oxides in materials failure. In contrast, S9, with no near-surface defects but experiencing strain variations, exhibits mechanical properties remarkably similar to those of S6, which shows the negative effect of presence of big oxides.

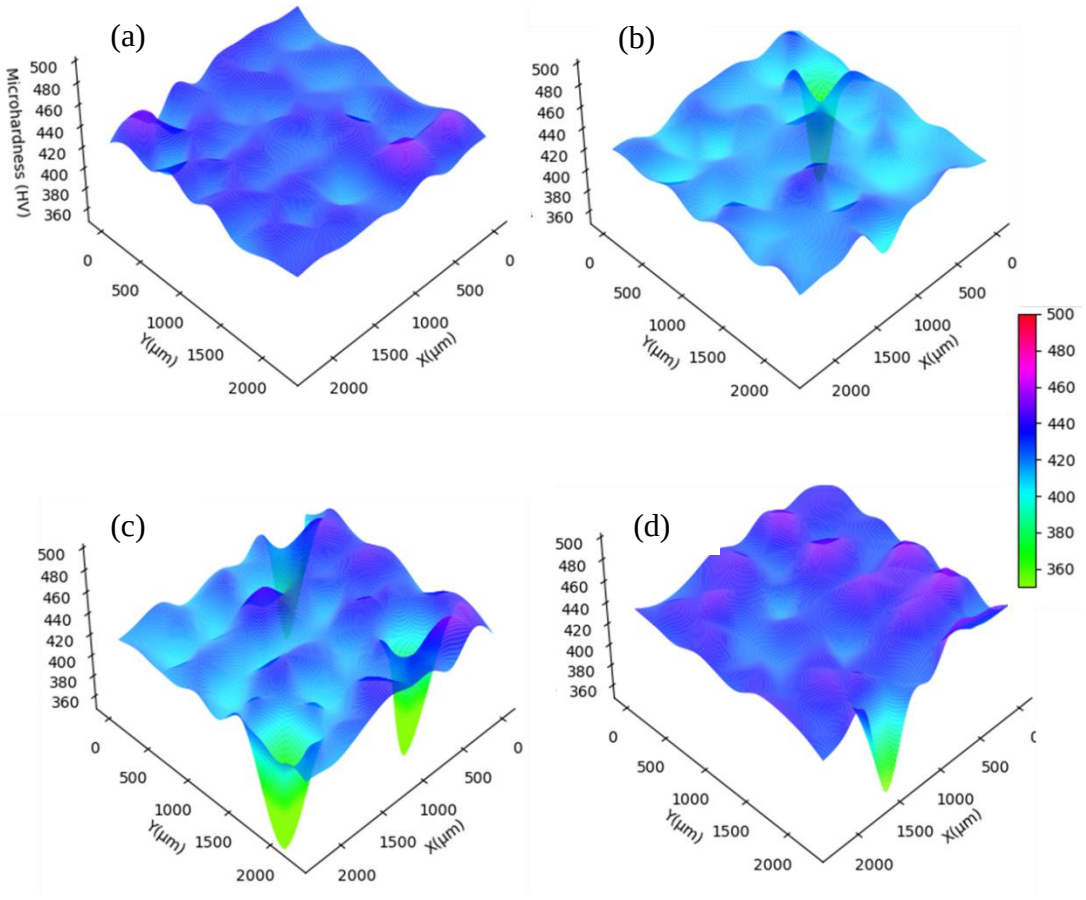

Figure 28. Microhardness map of the samples (a) Sample S6, (b) Sample S4, (c) Sample S9, (d) Sample S7

2.1.4.6 Critical VED Range and Mechanical Performance

The study identified a critical VED range of 57 J/mm³ to 59 J/mm³, where both oxide size and proximity to surface defects reached their minimum values. This minimization can be attributed to the marangoni flow and thermal gradients within the laser track at this VED. These conditions were unsuitable for segregation of alloying elements, leading to a more uniform chemical composition throughout samples. Similarly, the marangoni flow at this

VED did not support keyhole formation, resulting in conduction mode melting and reducing the thermal gradient, thereby minimizing gas expansion and near-surface defects. To achieve optimal processing parameters that minimized both alloying element segregation and near-surface defects caused by different factors, it was essential to reduce the balling effect and ensure conduction mode melting. A set of parameters were fabricated as sample SV1 to achieve this goal. The laser power was fixed at 250 W to avoid inhomogeneous balling and microstructure. A hatch distance of 0.12 μm was chosen to prevent lack-of-fusion defects, and the speed parameter was set to 800 mm/s to maintain the VED within the critical range.

Tensile test results, illustrated in Figure 28, showed that SV1 exhibited superior mechanical properties compared to samples fabricated within the critical VED range (S7 and S9), reaching a high UTS of 1590 MPa. This remarkable increase in strength is primarily attributed to the absence of near-surface defects in SV1. While gas porosities in SV1 were similar to those observed in S9, they were found to have less impact on strength compared to near-surface defects. Additionally, the oxide sizes in SV1 were all less than 16 μm (referring to the histogram in Figure 29), and the microhardness value fell within the range indicative of high mechanical strength samples. Furthermore, the uniformity of the microhardness distribution served as another indicator of the uniform microstructure within SV1. Based on these findings, the microhardness pattern and observation of near-surface porosities can be considered valuable criteria for optimizing the PBF process of H13 steel.

Remarkably, despite achieving a maximum relative density at a VED of 75 J/mm^3, SV1 outperformed S8 in terms of mechanical strength. This can be attributed to the more uniform microstructure and absence of near-surface defects in SV1. These findings emphasize the importance of achieving a uniform microstructure in the PBF process of H13, rather than solely focusing on maximizing relative density achievable at higher VED values.

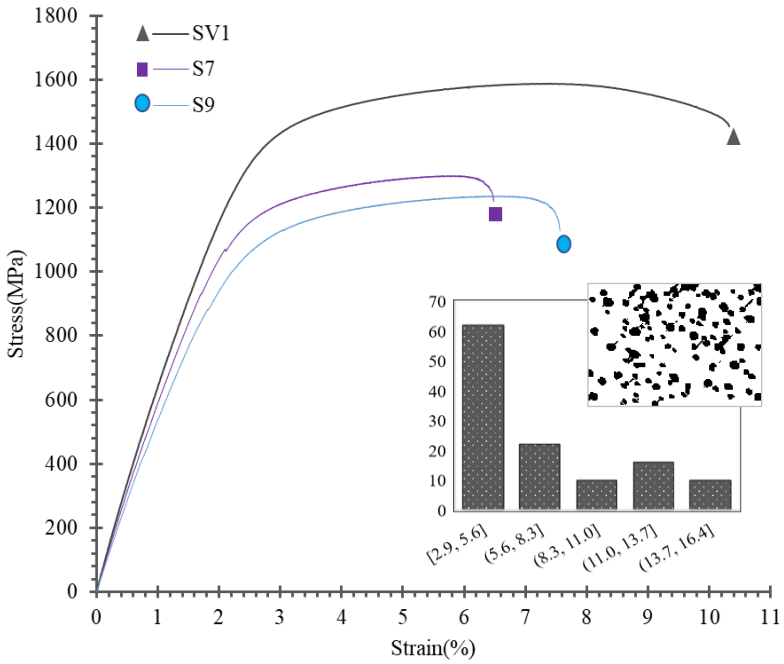

Figure 29. Tensile test result of the samples S7, S9, and SV1, with additional information about the histogram and of oxide particle size, and particle distribution analysis of SV1

2.1.5 **Conclusion**

This study unveils the role of processing parameters on elemental segregation, near-surface porosity formation, and their combined effect on the mechanical behavior of PBF-processed H13 steel. The investigation reveals that two primary factors govern the mechanical properties of PBF-ed H13: microstructural homogeneity and the absence of near-surface defects. The following key findings are drawn from the results:

1. A VED value of at least 57 J/mm³ is required to prevent lack-of-fusion (LOF) formation. As VED increases to this threshold, there is a corresponding rise in relative density. However, exceeding this value up to 75 J/mm³ can result in a decrease in relative density and an increase in keyhole and gas porosities. The VED of 59 J/mm³ marks a turning point where the melting and cooling dynamics effectively prevent the formation of keyhole and gas porosities near the surface.

2. The presence of gas and keyhole porosities near the last printed layer was identified as a detriment to the mechanical strength of PBF-ed H13. Samples characterized by minimal porosity displayed a substantial improvement in ductility and mechanical performance.

3. In the PBF process of H13, balling formation contributes to elemental segregation and, consequently, microstructural inhomogeneity. The microstructural pattern closely reflected the balling formation pattern. When there's a uniform and small balling formation, elemental segregation is minimal, and a more uniform pattern emerges. This is achievable at a VED of 57 J/mm^3. However, when the VED is elevated, such as at 75 J/mm^3, it leads to severe balling formation and disrupted balls, and the microstructural pattern becomes less uniform, consequently. This microstructural inhomogeneity can be assessed using the microhardness pattern. Oxide particle sizes below 6 micrometers indicate minimal segregation with negligible impact on mechanical strength.

4. The occurrence of balling formation in PBF-ed H13 is of significant importance, particularly at elevated VED levels, as it is a major contributor to poor surface roughness. This aspect is detrimental to both fatigue resistance and dimensional accuracy in precision manufacturing processes.

5. VED values in the range of 57-59 J/mm^3 are identified as critical for achieving several key outcomes, including minimal segregation, reduced balling effect resulting in a more uniform microstructure, and a lower probability of near-surface porosities. By carefully adjusting the processing parameters to maintain VED within this specific range, a favorable balance between these critical factors can be attained. In this study, superior mechanical properties were achieved by utilizing a laser power of 250W, a hatch space of 0.12 µm, and a laser speed of 800 mm/s. This parameter combination resulted in the absence of near-surface defects and oxide particles smaller than 17 micrometers.

6. In the context of PBF of steel alloys where elemental segregation plays a pivotal role, the microhardness pattern offers valuable insights into microstructural homogeneity, balling formation, and elemental segregation. Therefore, future studies should prioritize the examination of microhardness patterns over average values.

CHAPITRE 3

AMÉLIORATION DES PROPRIÉTÉS MÉCANIQUES DE L'ACIER H13 FABRIQUE PAR FUSION SUR LIT DE POUDRE (PBF) : UNE APPROCHE EN DEUX ÉTAPES INTÉGRANT L'OPTIMISATION DES PARAMÈTRES DU TRAITEMENT THERMIQUE

Narges Omidi[1], Asim Iltaf[1], Manel Houria[2], Mohammad Jahazi[2] Noureddine Barka[1], Claude Belzile[3]

[1]Department of Mathematics, Computer Science and Engineering, Université du Québec à Rimouski, Québec, Canada

[2]Department of Mechanical Engineering, École de technologie supérieure, Montréal, Québec, Canada

[3] Institute of Marine Sciences of Rimouski, Université du Québec à Rimouski, Québec, Canada

RÉSUMÉ EN FRANÇAIS DU TROISIÈME ARTICLE

La solidification rapide dans la fusion sur lit de poudre (PBF) de l'acier H13 provoque la ségrégation mésoscopique des éléments d'alliage qui ont une forte affinité pour l'oxydation lorsque le matériau est exposé à un traitement en four. La présence de particules d'oxyde réduit la résistance à la traction de l'acier H13 fabriqué par PBF. La taille et la distribution des oxydes dépendent à la fois des paramètres de traitement PBF et des paramètres de traitement en four. Le but de cet article est de maximiser la résistance à la traction de l'acier H13 fabriqué par PBF, le rendant comparable à l'acier H13 conventionnel, ce qui a été réalisé en deux étapes. Dans la première étape, les paramètres de traitement PBF, y compris la puissance du laser, la vitesse du laser, l'espacement des tracés, la stratégie d'impression et la température de préchauffage, sont optimisés pour les échantillons présentant le moins de défauts de fabrication (porosité et ségrégation d'éléments), et donc la résistance mécanique maximale. Ces paramètres de traitement optimisés sont ensuite utilisés pour l'étude du

traitement thermique. Dans la deuxième étape, un traitement thermique adapté pour l'acier H13 fabriqué par PBF est proposé en étudiant les effets des traitements de recuit, de trempe et de revenu sur la taille des particules d'oxyde, la microstructure et les propriétés mécaniques. Les résultats indiquent que le recuit joue un rôle clé dans l'élimination des contraintes résiduelles de l'acier H13 fabriqué par PBF, mais est insuffisant pour obtenir un allongement désirable. La trempe et le revenu sont nécessaires pour obtenir un allongement suffisant. Un traitement combiné de recuit avant trempe et revenu élimine les contraintes résiduelles avant la trempe et améliore encore la résistance à la traction.

Cet article, intitulé « Enhancing mechanical properties of PBF-ed H13: A two-step approach integrating processing parameter optimization and a tailored heat treatment», a été accepté pour publication dans la revue Metals and Materials International. En tant que premier auteur, ma contribution inclut la réalisation de recherches de pointe, la réalisation de tests expérimentaux, l'interprétation des résultats et la rédaction du manuscrit. Asim Iltaf, le deuxième auteur, a contribué à l'analyse de fractographie et à la partie expérimentale, y compris l'attaque chimique et l'imagerie par microscopie électronique à balayage (SEM). Manel Houria, le troisième auteur, a contribué à la révision de l'article dans l'analyse microstructurale. Le professeur Mohammad Jahazi, le quatrième auteur, contribue au développement de la méthodologie et aux aspects métallurgiques de cet article en tant que mon co-superviseur. Le professeur Noureddine Barka, le cinquième auteur, a fourni l'idée originale, développé la méthodologie et révisé l'article. Claude Belzile, le sixième auteur, a contribué à l'analyse EDS (spectrométrie de dispersion d'énergie) et à l'imagerie par SEM

3.1 Enhancing mechanical properties of PBF-ed H13: A two-step approach integrating processing parameter optimization and a tailored heat treatment

3.1.1 Abstract

Rapid solidification during Additive Manufacturing (AM) of H13 steel causes mesoscopic segregation of alloying elements which have high affinity for oxidation when the material is exposed to post AM heat treatment process. The presence of oxide particles reduces the tensile strength of the powder bed fusion-ed (PBF-ed) H13. The size and distribution of the oxides depend on the selection of both PBF and heat treatment parameters. The purpose of this paper is to maximize the tensile strength of PBF-ed H13, making it comparable to conventional forged and heat treated H13. The work was conducted in two steps: In the initial step, PBF processing parameters, including laser power, laser speed, hatching space, printing strategy, and preheating temperature, were optimized to achieve maximum mechanical strength by minimizing manufacturing defects. In the second step, a tailored heat treatment for PBF-ed H13 is proposed by investigating the effects of annealing, quenching, and tempering treatments on oxides characteristics and their impact on the microstructure and mechanical properties of PBF-ed H13. Results indicate that annealing plays a key role in removing residual stress from the material but is insufficient for achieving desirable elongation. Quenching and tempering are necessary to obtain sufficient elongation. A combined treatment of annealing before quenching and tempering removes residual stresses further improving tensile strength.

Keywords: H13 steel, Powder bed fusion, Tempering, Annealing, Post-treatment

3.1.2 Introduction

H13 tool steel stands out in high-performance applications like die casting molds due to its excellent resistance to deformation at high temperatures. This is attributed to the presence of carbide-forming elements, such as Cr, V, and Mo, which contribute to higher toughness, high hardenability, and fatigue resistance [143, 144].

In the last 20 years, the introduction of conformal cooling channels (CCCs) has addressed the limitations of conventional cooling channels, by providing improved access to critical hot points in the injection mold. CCCs enhance the heat conductivity of the mold, accelerating the cooling step, which constitutes 70% of the entire injection process, therefore a great improve in productivity of the process [145]. Numerical studies consistently show the superior efficiency of CCCs compared to traditional cooling channels [146]. Industrial case studies further support this, demonstrating increased productivity in the molding process by incorporating additively manufactured inserts of CCCs within an existing mold, containing traditional cooling channels [2, 6, 147-149].

Powder bed fusion (PBF) is a reliable method for the production of high-precision metal additive manufactured parts [150]. PBF involves melting and rapidly cooling layers of metal powder, one on top of the other, to form the final shape. In alloy steel, rapid cooling introduces complexity in the microstructure of the material, affecting the mechanical performance of PBF-ed specimens when compared to their conventional forged counterparts. While some additively manufactured metals, such as austenitic steels, demonstrate superior performance [151], others such as H13 tool steel, exhibit lower-than-expected mechanical performance [83] and frequently do not meet the material requirements for resistance to cyclic loading at high temperatures; as encountered in moulding processes. The reduced performance of PBF-ed H13 is attributed to the presence of: porosity [71], elemental alloy segregation [120], a high level of compressive residual stresses [139], and a fully martensitic structure alongside retained austenite, in the as AM material, due to the inherent nature of the PBF process [138]. Regarding the porosity, it has been thoroughly studied and effectively addressed by optimizing processing parameters with resulting porosity levels of less than 1% [27, 51, 69, 71, 152, 153]. In contrast, elemental alloy segregation in PBF-ed H13 has been rarely studied. Overall, the high level of residual stresses and the martensitic structure result in highly brittle as-built specimens, making them unsuitable for direct use in industrial applications. The inherent brittleness of PBF-ed H13 necessitates post-treatment. A proper heat treatment of PBF-ed H13 can alter the material's microstructure by reducing elemental

segregation, relaxing the residual stresses, and increasing ductility. Few publications are also available on optimizing the heat treatment process of PBF-ed H13 alloy.

The microstructure of PBF-ed H13 differs from conventional H13, primarily due to the rapid cooling, approximately ~1.83 $\times 10^4$ K/s [138]. The microstructure of the as built material mainly consists of martensite and a high content of retained austenite (16.5%-29.7%), which is destructive to dimensional stability [51, 71, 76, 77]. The rapid cooling also results in the formation of cellular structures with a higher content of V, Si, Mo, and Cr segregated in the cellular walls. Along the building direction, these cellular walls exhibit a mixture of rounded and elongated structures oriented toward the heat flux [51] . Rapid cooling also leads to precipitated MC,M_3C, and M_7C_3 (M=V, Cr, Mo) carbides inside the cellular walls [76]. Additionally, mesoscopic segregation of the main alloying elements occurs within the scale of one laser track, as reported by Xie et al. [120]. The structural changes during PBF, alter the $\gamma \rightarrow \alpha$ phase transformation temperatures (which is between 1133 K (AC1) and 1188 K (AC3)) [143], implying that the typical heat treatments applied to conventional H13 may not be suitable for PBF-ed H13.

While heat treatments for conventional H13 steel, including annealing and tempering, have been extensively investigated, a notable gap exists in the literature regarding PBF-ed H13. Previous studies have thoroughly examined the microstructure of conventional H13, focusing on the evolution of carbides such as Cr-rich, Mo-rich, and V-rich carbides, including MC, M_7C_3, $M_{23}C_6$, M_2C, and M_6C, at different annealing and tempering temperatures [43, 143, 144, 154, 155]. Subsequently, the effect of microstructure on mechanical properties has been reported, summarized in Table 10. Results exhibit, higher tempering temperatures generally result in decreased UTS and yield stress but increased elongation. The optimized treatment parameters recommended by Wang et al. [156] is quenching at 1040°C followed by tempering at 570°C. Despite the wealth of knowledge on conventional H13 steel, comprehensive studies on the effects of heat treatments on PBF-ed H13 remain scarce. Some research has been conducted, aiming to achieve a holistic understanding of how these treatments impact the microstructure and mechanical properties of PBF-ed H13, as

summarized in Table 11. However, several gaps in this area are evident. Firstly, compared with Table 10, there is an absence of sensitivity analysis regarding the mechanical properties of PBF-ed H13 to tempering temperature variations. This aspect has only been investigated at temperatures from 585°C to 620°C. Secondly, the mechanical properties of PBF-ed H13 are mainly reported after annealing treatment, respectively at 650°C in references [30] and [28], and at 600°C and 700°C in reference [49]. Even for tempered material, an annealing treatment was performed beforehand, lasting 5-8 hours at 650°C, as previously described in references [30], and [28]. This highlights the effect of stress-relieving annealing in PBF-ed H13. Despite this importance, the effect of annealing temperature variation before tempering has not been reported yet.

Table 10. Mechanical properties of conventional H13 steel following tempering treatment, based on the literature

Ref.	Austenitizing& Quenching			Tempering			Tensile behavior		
	Temp (°C)	*Time (min)*	*cooling condition*	*Temp (°C)*	*Time (hour)*	*cooling condition*	σ *(MPa)*	σ_y *(MPa)*	Elongation (%)
[143]	~1030	20	oil	~500	4	air	~2000	~1500	~1.25
				~590			~1600	~1250	~11
				~650			~1000	~760	~13
				~700			~950	~750	~17.5
[154]	1050			500	4	air	~2500	*	*
				580			~1800	*	*
				600			~1600	*	*
				640			~1100	*	*
[156]	1040	30	oil	570	2	air	~1840	~1670	~2.1
				590			~1750	~1550	~2.8
				610			~1600	~1390	~5.9

Table 11. Mechanical Properties of PBF-ed H13 steel following different furnace treatment

	Stress Reliving		Tempering		Tensile behavior			
Ref.	*Temp (°C)*	*Time (hour)*	*Temp (°C)*	*Time (hour)*	UTS *(MPa)*	*Elastic modulus (GPa)*	σ_y *(MPa)*	*Elongation (%)*
[30]	650	5	*	*	1289 ± 6	204.5 ± 1.4	1142 ± 4	10.6 ± 1.1
	650		610	2	1473 ± 13	205.3 ± 0.7	1313 ± 9	7.4 ± 3.8
[28]	650	8	*	*	1297	199±	1155	4.2 ± 3.0

						1.5		
	650		585	2.25 – 3	1640	190± 1.9	1447	3.3 ± 1.6
[49]	*	*	600[1]	2	1938 ± 62	*	1483 ± 48	5.8± 0.61
			700[1]	2	1076 ± 21		877 ± 18	10.95±1.68
[157]	*	*	620	2	1457	*	1230	6.50

[1]In ref [49] the tempering has been conducted without pre-quenching

The aim of this paper is to fill the gaps in the field by exploring a customized heat treatment for PBF-ed H13. Step one involved optimizing processing parameters to achieve maximum mechanical strength. Step two explored the sensitivity of the material's mechanical properties to annealing and tempering time and temperature. Step three studied the effect of annealing treatment before tempering to provide a comprehensive understanding of the heat treatment process and its impact on the mechanical behavior of PBF-ed H13.

3.1.3 **Materials and methods**

3.1.3.1 Materials and mechanical tests

The materials used in this study was gas atomized H13 powder with the chemical composition outlined in Table 12. The powder particles were spherical shape with a size range between 15-55 μm. Figure 30 provides an illustrative example of the shape and size of the as received powder. The image showing a collection of spherical particles. The scale bar at the bottom right indicates that the field of view is 50 μm wide. The particles vary in size, and their surfaces appear textured and rough. Some particles have smaller satellite particles attached to their surfaces. The specimens were manufactured using the EOS M290 machine.

Table 12. Chemical composition of the powder

Elements	Fe	Cr	Mn	Mo	Si	V	C	Others
MIN(WT.%)	Bal.	5.0	0	1.0	0.5	0.5	0.3	0
MAX(WT.%)	Bal.	6.0	0.6	2.0	1.0	2.0	0.5	0.05

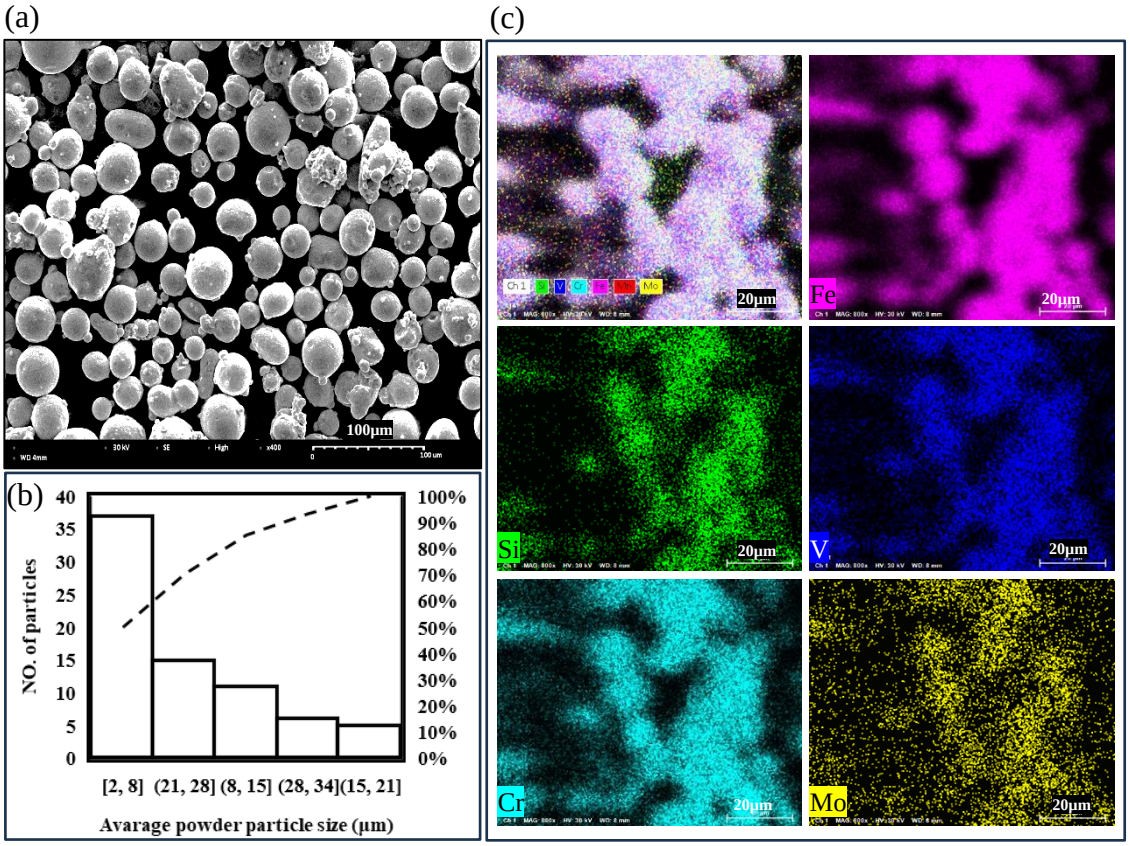

Figure 30. H13 powder characteristics: (a) SEM image of the as supplied powder, (b) powder particle size distribution, and (c) EDS elemental map

For the microstructural observations, the samples were cut in the building direction, mounted, and ground using abrasive papers with grit numbers 180, 240, and 320. Subsequently, two different etching solutions were employed: Vilella's reagent (comprising ethanol, hydrochloric acid 5-8%, isopropanol 3-5%, methanol 3-5%, picric acid 1-2%) and Carpenter reagent (ferric chloride 8.5 g, Cupric chloride 2.4 g, alcohol 122 ml, hydrochloric acid 122 ml, nitric acid 6 ml). Vilela's reagent was utilized for microstructural observations, while Carpenter's etchant was employed specifically for oxide particle examinations. In the microstructural examination, samples were immersed in the solution for 30 seconds and, for oxide particle observations, samples were exposed to the etching solutions for 15-45 seconds, depending on the size of the particles, until the oxide particles were fully revealed. A Nikon Eclipse MA100 optical microscope and Hitachi SNE-3000MS scanning electron microscope

(SEM) SEC SNE-4500M equipped with the energy dispersive spectroscopy (EDS) were used were used for the fractography, imaging, and observations and analysis of the chemical composition. Optical microscopy images were captured at similar zoom levels across all samples. The OM images were captured at similar zoom levels for all specimens. The projected area of each particle in the images was then calculated using image analysing software. The particles were assumed to be rounded in shape, and with this assumption, the average diameter was calculated based on the projected area. The particle size distribution was illustrated with histograms and box plots to visualize the data and identify trends. The room temperature tensile properties were assessed using an MTS810 machine at a strain rate of 0.004 s^{-1}, following the ASTM E8 standard for sub sized samples [158].

3.1.3.2 Design of the experiments

In the first step of the work, the processing parameters of the PBF process were optimized for maximum strength. Then, the optimized setup was used to investigate the effects of time and temperature of the heat treatment on the evolution of tensile strength. Figure 31 depicts the flow chart of the experiments, where two main steps are shown in by white rectangles: The horizontal line of the flow chart outlines the procedure followed in step1, consisting of four steps, indicated by grey rectangles. For example, Step 1, dimensional stability optimization, samples S1-S9 (refer to Table 13 for PBF processing conditions) to determine a suitable range for the volumetric energy density (VED) that would result in samples with dimensional stability. The determined range of VED in this step (9 to 104 J/mm^3) is then used for the next step, which is mechanical properties optimization. In this step, samples S10-S19 (refer to Table 13) were utilized to optimize laser power (P), laser speed (V), and hatching distance (H) for maximum mechanical strength and minimum porosity. The optimized P, V, and H are then used in steps 3 and 4 to optimize preheating temperature (S20) and printing strategy (S21). The applied printing strategies are shown in Figure 32.

The optimized processing parameters through these four steps were then used for Step 2 of the study which involved a series of different treatments, comprising 14 different batches of samples, as shown in Table 14. The effects of annealing (temperature range of 400-650 °C, time range of 2 to 6 hours), quenching and tempering (temperature range of 500-750 °C, time range of 2 to 6 hours), and annealing (temperature range of 500-600 °C) prior to quenching and tempering at 550 °C were investigated. The samples in step 2 underwent microstructural observation, fractography, and to the obtained results are correlated with the mechanical properties.

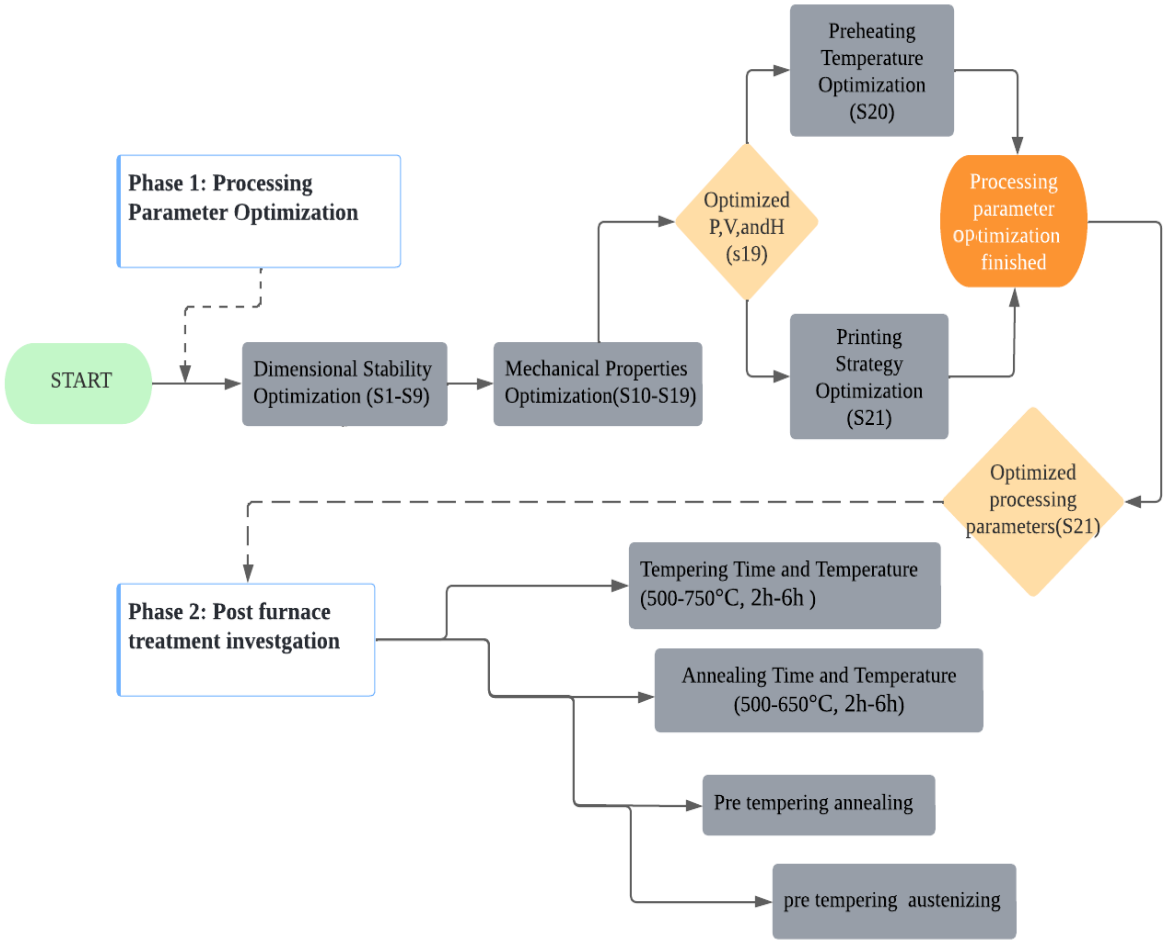

Figure 31. Flowchart of the experimental procedure

Table 13. Processing parameters in the step 1

Code	Laser power (W)	Laser Speed (mm/s)	Hatch distance (mm)	Printing strategy	Preheating temperature (°C)	VED (J/mm^3)
S1	150	400	0.8	67-Simple	80	9
S2	150	600	0.1	67-Simple	80	50
S3	150	800	0.12	67-Simple	80	31
S4	200	400	0.8	67-Simple	80	13
S5	200	600	0.12	67-Simple	80	56
S6	200	800	0.8	67-Simple	80	6
S7	250	400	0.12	67-Simple	80	104
S8	250	600	0.8	67-Simple	80	10
S9	250	800	0.1	67-Simple	80	63
S10	250	750	0.10	67-Simple	80	67
S11	250	800	0.12	67-Simple	80	52
S12	250	850	0.14	67-Simple	80	42
S13	275	750	0.12	67-Simple	80	61
S14	275	800	0.14	67-Simple	80	49
S15	275	850	0.10	67-Simple	80	65
S16	300	750	0.14	67-Simple	80	57
S17	300	800	0.10	67-Simple	80	75
S18	300	850	0.12	67-Simple	80	59
S19	275	800	0.12	67-Simple	80	57
S20	275	800	0.12	45-strip	80	57
S21	275	800	0.12	45-strip	150	57

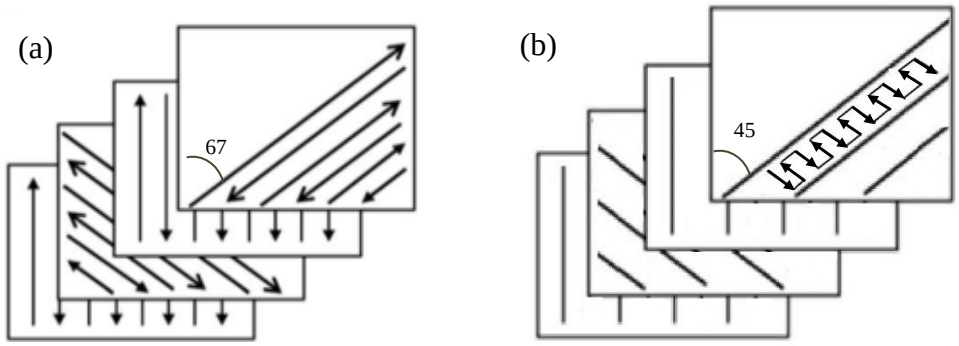

Figure 32. Applied printing strategies (a) 67° Rotation and (b) 45° rotation (Rectangular-Filled Pattern with 45° Rotating Stripes) (adopted from refrence [159])

Table 14. Furnace treatment condition in step 2

Code	Annealing			Austenitizing			Double tempering		
	Temp (°C)	Time (h)	cooling condition	Temp (°C)	Time (min)	cooling condition	Temp (°C)	Time (h)	cooling condition
ST1	*						550	2	air
ST2				1020	60	oil	500	2	air
ST3				1020	60	oil	550	2	air
ST4				1020	60	oil	600	2	air
ST5				1020	60	oil	650	2	air
ST6				1020	60	oil	750	2	air
ST7				1020	60	oil	600	6	air
SAT1	500	2	furnace	1020	60	oil	550	2	air
SAT2	600	2	furnace	1020	60	oil	550	2	air
SA1	400	2	furnace	*					
SA2	500	2	furnace						
SA3	550	2	furnace						
SA4	550	6	furnace						
SA5	650	6	furnace						

3.1.4 **Results and discussions**

3.1.4.1 PBF processing parameters optimization

S1-S9 samples were manufactured to be dimensionally stable. According to the results, if the VED is below a certain value (40 J/mm^3), the samples may collapse at the edge or exhibit excessive porosities, leading to concave surface. Conversely, for VED values above a certain threshold 75 J/mm^3, the samples exhibit excessive melting, which result in a very rough printing surface. The appropriate range to avoid dimensional instability is around 50-80 J/mm^3. Therefore, the laser power, laser speed, and hatching distance in the second step were chosen in a way to keep the VED within this range (S10-S18). Samples fabricated under these conditions indeed showed good dimensional stability. Microstructural observation, oxide formation, and porosity observation have been explored in previous works. It has been demonstrated that keyhole and gas porosities formed near the last printed layer are determining factors for mechanical strength. Additionally, elemental segregation in H13 is inevitable, and it has a direct relationship with oxide formation. The study has shown

that the maximum mechanical strength with optimized P, V, and H is around 1300 MPa, and elongation is near to 8.4% (after stress relieving, including heating samples up to 650°C, holding for 6 hours, followed by cooling in furnace).

In the third step, a preheating temperature of 150 °C was applied. It was previously shown that a minimum preheating temperature of 400 °C (above martensite transformation) is required to observe a considerable improvement in mechanical properties [26]. However, in the application of a preheating temperature of 150°C brought a clear increase in UTS, bringing it from 1300 MPa to approximately 1500 MPa. This improvement could be attributed to the change in thermal history of the sample, which reduces its residual stressed [26]. In the last step of processing parameters optimization, the 45-degree rotation strategy brought further improvement by increasing the UTS from 1400 MPa to 1590 MPa. This improvement is again attributed to the reduction in residual stress due to the change in thermal history of the samples [159]. Based on the above results, Sample S21, was identified as the representative sample with optimized processing parameters produced with a laser power of 275W, laser speed of 800 mm/s, hatching space of 0.12 mm, printing strategy of 45-degree rotation, and a preheating temperature of 150°C.

3.1.4.2 Microstructure characterization

The optimized as-built material demonstrates a relative density exceeding 99.80%, with porosity primarily observed at sizes below 3 µm. These pores are predominantly rounded gas porosities, which are generally less detrimental to the mechanical strength of the material. The morphology of these rounded pores reduces their effectiveness as crack propagation paths, particularly in H13 steel, which is known to be susceptible to hot cracking due to phase transformations during processing, such as the approximately 5% volumetric expansion [140] associated with the austenite to martensite transformation.

The optical microscopy image of the as-built material is shown in Figure 33-a, depicting the laser tracks in the building direction, highlighted by white dashed lines. The higher magnification image provided in Figure 33-b reveals that the microstructure consists

of elongated grains in the fusion zone (FZ) of the laser track, which is a result of the directional solidification occurring during the PBF process. This rapid cooling, typically at a rate of approximately 1.83×104 K/s [119, 138]. In the heat-affected zone (HAZ), the microstructure shows rounded cellular structures, a typical feature of localized re-melting and solidification driven by thermal gradients during the PBF process [157]. The cellular structure in the as-built H13 steel exhibits sizes of less than 1 μm, which is characteristic of the fine microstructure produced during the rapid solidification in additive manufacturing processes [71]. The as-built material's microstructure is nearly fully martensitic with retained austenite (16.5-29.7% [71, 77, 160]), and some carbide precipitates [108], as expected due to the rapid cooling rates involved in PBF, which suppress the diffusion necessary for the formation of equilibrium phases such as ferrite [138]. The presence of martensite generally results in high hardness, typically around 650 to 689 HV 0.2 [71], but also introduces brittleness [161].The presence of retained austenite is a consequence of rapid cooling, during which carbide precipitation and growth are suppressed, allowing more alloying elements to remain dissolved in the austenite. This leads to a reduction in the martensite start transformation temperature, which in turn contributes to the retention of austenite in the final microstructure [48, 142]. Retained austenite, on the other hand, may influence the mechanical properties by providing some toughness, although it can also transform into martensite under applied stress, potentially affecting the material’s performance under cyclic loading[28]. Furthermore, the retained austenite films, particularly those enriched in carbon, exhibit low mechanical stability within the martensitic matrix. This instability can cause these films to transform into high-carbon martensite when subjected to stress during plastic deformation, leading to a higher susceptibility to cracking. Due to the directional solidification inherent in the SLM process, most of these retained austenite films align with the building direction. This alignment significantly impairs the ductility of the steel, especially under transverse loading conditions where the load is perpendicular to these films, further exacerbating the material's brittleness [162].

The optical microscopy of the annealed material at different temperatures, ranging from 400°C to 550°C, did not show significant differences compared to the as-built material.

This stability in microstructure is attributed to the fact that annealing within this temperature range is insufficient to initiate significant phase transformations in the martensitic structure, as the temperature remains below the critical temperature for austenite formation (AC1), which for carbon steel including H13 steel is approximately 723°C [163].Figure 33-c shows the microstructure of a specimen annealed at 550°C (sample code SA4). In this image, the black dashed lines indicate the laser tracks. The fusion zone retained the elongated grains aligned in the heat flux direction, while the heat-affected zone continued to exhibit the rounded cellular morphology. indicating that the thermal exposure was not sufficient to cause significant grain growth or phase transformation. The images suggested approximately no change or negligible change in the grain size and morphology compared to the as-built. This lack of microstructural change suggests that the martensitic structure remains largely intact, with only minor relief of residual stresses and possible minor tempering effects occurring at this temperature**.** Substantially high residual stresses in the range of 940–1420 MPa were detected in the as-built H13 material, as reported by Yan et al. [138]**,** and annealing at these temperatures likely provides only partial stress relief without significantly altering the overall microstructure**.** The higher magnification image of the specimen annealed at 650°C is displayed in Figure 33-d. This image shows significant changes compared to the annealing up to 550°C. The microstructure of the material after annealing at 650°C for 6 hours shows grain boundaries that have grown to sizes ranging from approximately 10 µm to 30 µm. This indicates that the material has undergone partial tempering, where martensite begins to decompose into ferrite and carbides, as suggested by M. Åsberg et al. [28]. These observations suggested that the annealing process, within the specified temperature range of 400°C to 550°C, did not markedly alter the microstructural features established during the PBF process. The cellular morphology and elongated grains in the fusion zone remained prominent, highlighting the stability of these microstructures under thermal treatment.

In terms of mechanical properties, in annealed material the retention of the martensitic structure and minimal microstructural changes up to 550°C suggest that the material would maintain its high hardness and strength, similar to the as-built condition, with only minor reductions due to the partial relief of residual stresses. However, the absence of significant

grain growth or phase transformations implies that there would be limited improvement in ductility or toughness at these temperatures. At 650°C, where martensite begins to decompose into ferrite and carbides, the mechanical properties would likely reflect a reduction in hardness and strength but an increase in ductility, as the material transitions from a predominantly martensitic structure to a more tempered microstructure with a mix of ferrite and carbides.

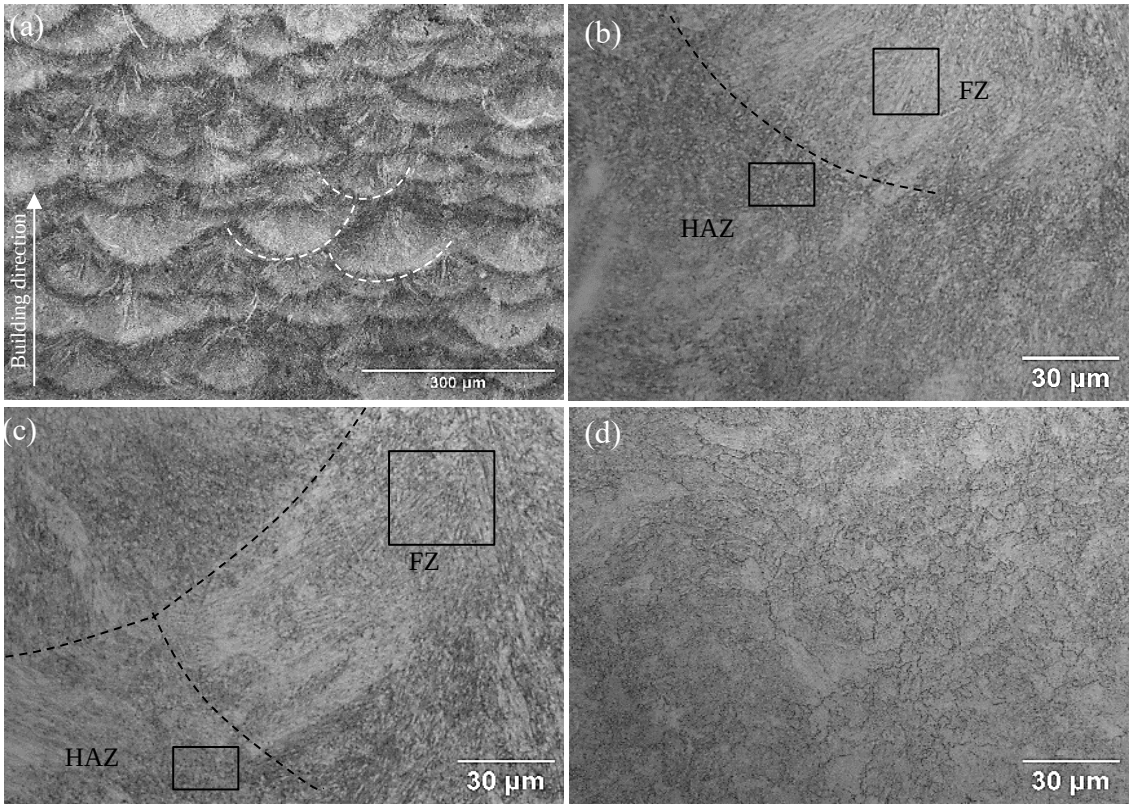

Figure 33. Optical microscopy image of: (a) as-built specimen at low magnification, (b) as-built specimen at higher magnification, (c) annealed specimen at 550°C with sample code SA4, and (d) annealed specimen at 650°C with sample code SA6

The optical microscopy images of the tempered specimens are shown in Figure 34, illustrating the microstructural changes at various tempering temperatures. Tempering is primarily aimed at reducing the brittleness of martensitic structures by allowing carbon atoms trapped in the martensite to diffuse out, forming carbides and stabilizing the structure [164].

Figure 34-a shows the microstructure of the tempered material at 550°C. The structure exhibited similar features at both the edge and the middle of the sample. At this temperature, the microstructure remains largely martensitic with tempered martensite (with martensitic grains stays less than 1 µm), indicating that the tempering process has begun to relieve some internal stresses and reduce hardness without fully decomposing the martensite. This microstructure is approximately similar to the as-built and annealed specimens at temperatures below 650°C, primarily retaining the martensitic structure with minimal changes.

For the specimens subjected to quenching before tempering (QT-ed), the microstructure is depicted in Figure 34-b to Figure 34-h. It is noticeable that the microstructure of these specimens shows differences between the edge and the middle likely due to varying cooling rates experienced during quenching. Figure 34-b shows the microstructure at the edge of the specimen QT-ed at 500°C, and Figure 34-c shows the same specimen with higher magnification. The microstructure exhibits a coarse-grained structure with an average grain size of approximately 15 µm. Within these grains, a fine martensitic structure is observed, characterized by martensitic laths with widths of less than 1 µm. According to Jian Wang et al. [156], the microstructure consisted of tempered martensite in the middle where cooling rates were more uniform, leading to more consistent transformation to martensite. In contrast, the edge, which cooled more rapidly, retained some prior austenite grains that did not fully transform into martensite. However, this observation could also indicate the presence of ferrite cells, as the material has been reported to exhibit a ferritic-martensitic structure in previous studies [165, 166]. On the other hand, the microstructure image of the material is similar to a dual-phase steel structure, characterized by martensite distributed between ferrite grains [167]. This dual-phase morphology is evident near the edge of the specimen, particularly in the transition area (indicated in Figure 34-b) where the structure shifts from this dual-phase morphology to a predominantly tempered martensite structure towards the core. The formation of dual-phase structures, as discussed by Xue-Ling Cai et al. [168], is primarily influenced by the specific heat treatment and cooling processes, particularly intercritical annealing, where the material is heated to a temperature

within the two-phase region between the A1 and A3 temperatures. The steel discussed in the paper has a composition of 0.11% C, 1.60% Mn, 0.73% Si, and 0.21% Mo, with manganese (Mn) playing a critical role in stabilizing austenite and influencing the partitioning behavior during phase transformations. This Mn concentration is key in the formation of dual-phase microstructures, where austenite transforms into martensite upon cooling, while the redistribution of Mn during annealing affects the formation of retained austenite or other phases like bainite. In comparison, H13 tool steel, which typically contains 0.32-0.45% C, 0.20-0.50% Mn, 0.80-1.20% Si, 4.75-5.50% Cr, 1.10-1.75% Mo, and 0.80-1.20% V, has a more complex alloying system where chromium and vanadium also play significant roles in phase stability and transformation kinetics. While Mn still contributes to austenite stabilization in H13, the presence of chromium and vanadium influences the formation of carbides and other microstructural features that can affect the dual-phase structure. This transition suggests that the material experiences varying cooling rates across its cross-section, leading to a mixed microstructure that combines the strength of martensite with the ductility of ferrite in certain regions.

Figure 34-d to Figure 34-h illustrate the effect of tempering temperature on the microstructure in the middle of the specimens at different temperatures (500°C, 550°C, 600°C, 650°C, and 750°C, respectively) on the QT-ed specimens. With increasing tempering temperature, the microstructure gradually changes, showing an increase in lath or grain size as the martensitic laths begin to lose their distinct boundaries and coalesce into larger grains. These changes are indicative of the tempering process driving the decomposition of martensite into ferrite and carbides at higher temperatures [143]. At tempering temperatures of 500°C and 550°C, the microstructure is characterized by a very fine martensitic structure (less than a μm). However, as the tempering temperature increases, there is a significant coarsening of the martensite. By 600°C, larger martensitic laths begin to appear, with widths increasing up to approximately 10 μm. This trend continues at higher temperatures, with the number of coarse and larger martensitic structures 650°C and 750°C. Figure 34-d and Figure 34-e at 500°C and 550°C show fine tempered martensite structures that are relatively uniform, with well-defined lath boundaries. Figure 34-f to Figure 34-d-h show a transition

towards a more ferritic/binite structure with less distinct tempered martensite laths, indicating the beginning of martensite decomposition [143]. These observations suggested that lower tempering temperatures (500°C to 550°C) retained more of the martensitic structure, likely maintaining higher hardness and strength, but with some improvement in toughness and ductility due to the relief of residual stresses **.** In contrast, higher tempering temperatures (600°C to 750°C) lead to the decomposition of martensite into ferrite and bainite, resulting in a softer, more ductile material with possibly significantly reduced hardness**.**

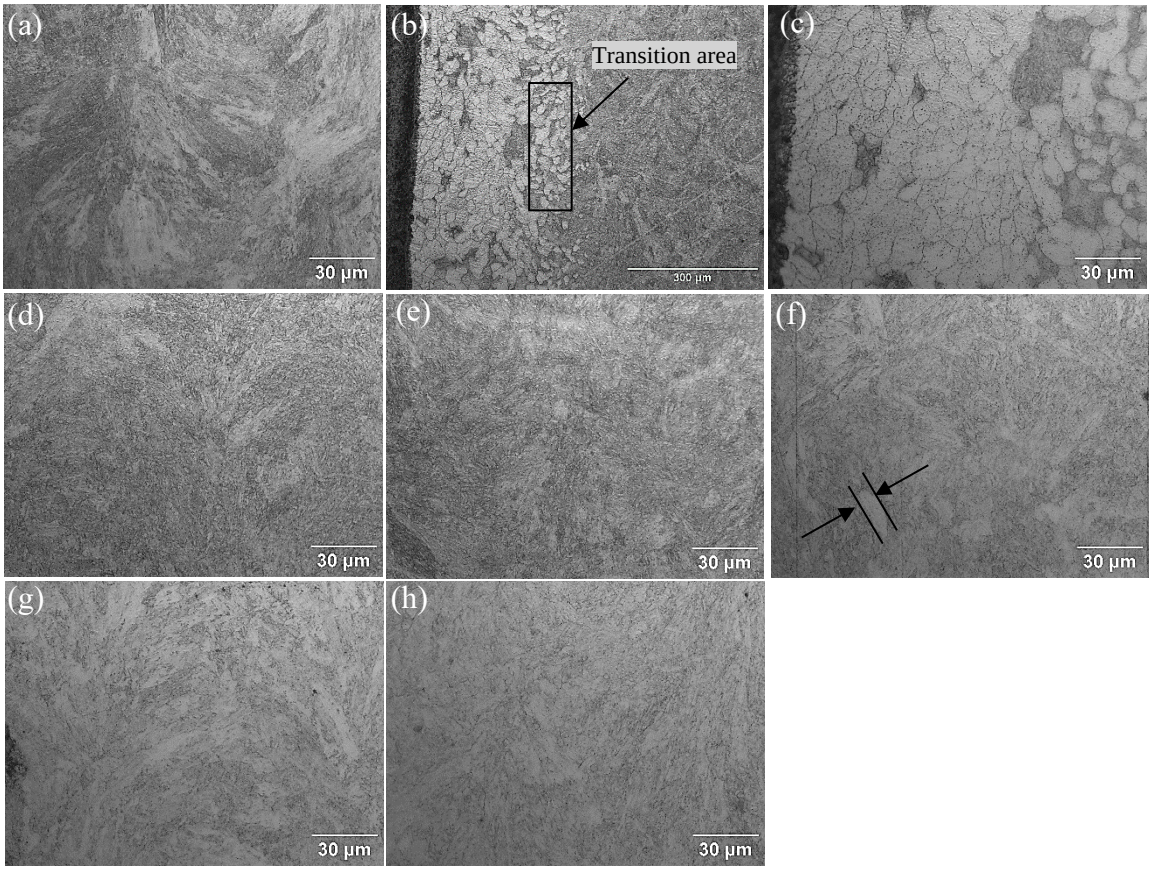

Figure 34. Optical microscopy image of: (a) tempered material at 550°C with sample code ST1, (b) edge of specimen QT-ed at 500°C with sample code ST2, (c) middle of specimen QT-ed at 500°C with sample code ST2, (d) QT-ed specimen at 500°C with sample code ST2, (e) QT-ed specimen at 550°C with sample code ST3, (f) QT-ed specimen at 600°C with sample code ST4, (g) QT-ed specimen at 650°C with sample code ST5, and (h) QT-ed specimen at 750°C with sample code ST6

The optical microscopy images of specimens that were first annealed and then subjected to QT are shown in Figure 36. Figure 36-a illustrates the microstructure of a specimen annealed at 500°C and then QT-ed at 550°C. Since annealing at 500°C did not show significant changes in the as-built material, the microstructure of the specimen annealed at 500°C was similar to that of the specimen only double tempered at 550°C. The microstructure was primarily martensitic(fine and , less than a few μm) , where the martensite laths could be seen clearly. This indicates that the initial annealing at 500°C retained much of the as-built microstructure, maintaining the martensitic structure. Figure 36-b presents the microstructure of a specimen annealed at 600°C and then QT-ed at 550°C. The microstructure showed a slight transition, likely due to the effect of the microstructure before quenching. It could be observed larger laths (lath width less than 6 μm) of martensite, suggested the beginning of martensite decomposition to ferrite or bainite. The higher annealing temperature at 600°C led to increased diffusion rates, which resulted in larger grain sizes. These observations suggested that annealing at a lower temperature (500°C) before quenching and tempering resulted in a finer, more uniform tempered martensitic structure, similar to the as-built material. In contrast, annealing at a higher temperature (600°C) led to coarser microstructural features, with evidence of martensite decomposition to ferrite or bainite. The combination of annealing and subsequent quenching and tempering effectively modified the microstructure, optimizing the balance between strength and ductility in the material.

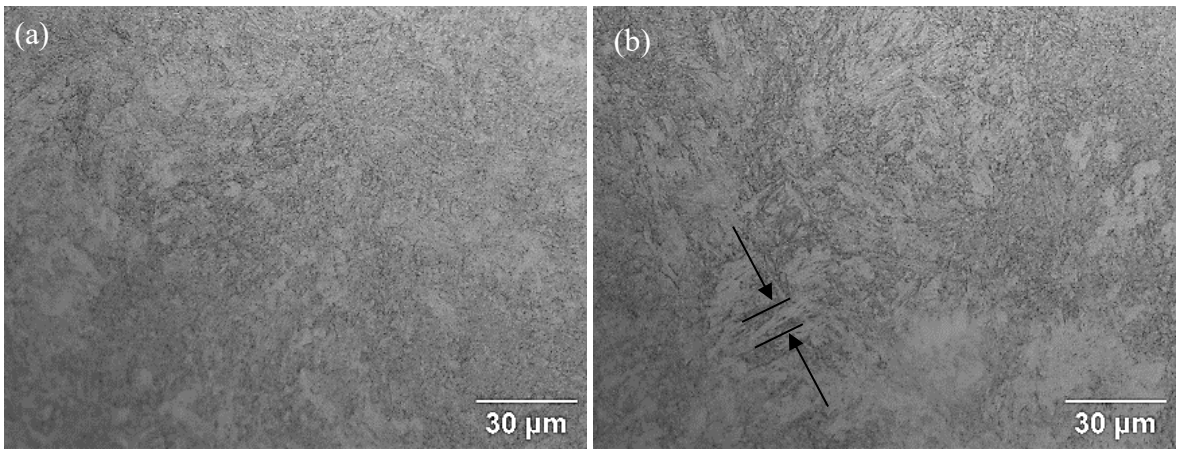

Figure 35. Optical microscopy images of specimens annealed at (a) 500°C and (b) 600°C, then QT-ed at 550°C

SEM imaging was conducted to observe the microstructure in detail and to examine the effect of these treatments on carbide formation. Lei et al. [138] and Karthik et al. [169] reported that, the microstructure of a rapidly cooled tool steel, like the PBF process, consists of fine martensite and retained austenite (austenite in the form of cellular colonies). This phenomenon has been attributed to the influence of rapid cooling on carbide formation, contrasting with cast material where sufficient time allows for carbide formation from alloying elements. In samples manufactured using the PBF technique, alloying elements remain dissolved in cellular colonies of austenite. This, in turn, lowers the martensite formation temperature, potentially resulting in the retention of some austenite in the final structure at room temperature [142].

In the present work, the microstructure of as-built specimens (Figure 36-a) revealed a cellular morphology. With increasing annealing temperature from 400°C to 650°C, there is a tendency for the austenitic cellular walls to dissolve. This transformation becomes evident at 650°C (Figure 36-c), where the walls appear considerably disrupted. However, such changes in the microstructure not observable at 550°C (Figure 36-b); the microstructure underwent minimal change compared to as built specimen in Figure 36-a.

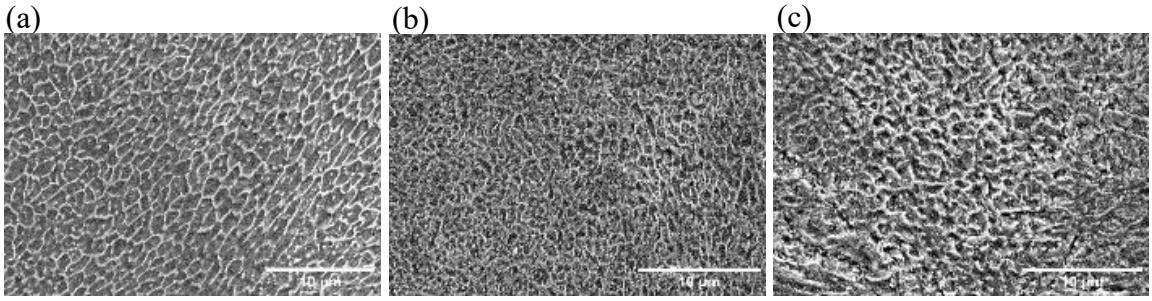

Figure 36. SEM micrographs illustrating the microstructure of: (a) as-built specimen, (b) annealed specimen at 550°C with sample code SA5, and (c) annealed specimen at 650°C with sample code SA6

The microstructure of the tempered samples is different from annealed ones. For example, as shown in Figure 37-b and 5-c, cellular walls no longer exist in tempered specimens. For tempering temperature in the 500-600 °C interval, the microstructure predominantly consists of tempered martensite, with rounded shape carbides along the boundaries of the martensitic structure (Figure 37-b). At 650°C, interconnected networks of carbides could be seen (Figure 37-c), in agreement with the findings of Deirmina et al. [89]. EDS map of alloying elements after tempering at 650°C (Figure 37-d) demonstrates a higher concentration of carbon and other alloying elements, such as Cr, V, and Mo. while we were not able to confirm, Åsberg et al. [28] suggest that these structures are likely networks of Cr- and Mo-rich. It is notable that in conventional H13, when increasing the tempering temperature the Cr_7C_3 phase is converted to a round granular $Cr_{23}C_6$ phase, and then, the $Cr_{23}C_6$ phase tends to coarsen, resulting in a decreased hardness with a high impact toughness and elongation [156].However, in the case of PBF-ed H13 the situation is reversed and until 600°C the carbides are rounded and dispersed, and at 650°C the networks of carbide emerge.

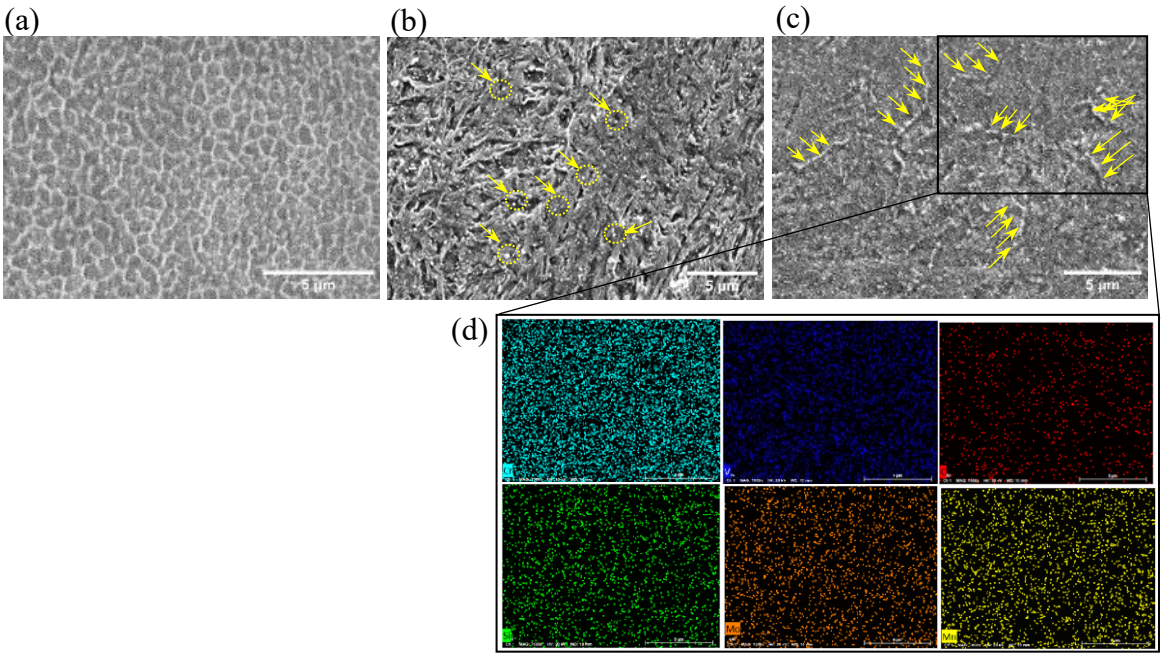

Figure 37. SEM micrographs illustrating the microstructure of: (a) as-built specimen, and tempered at (b) 600°C for 2 hours with sample code ST4, and (c) 650°C for 2 hours with sample code ST5. Yellow arrows indicating the rounded carbides in (b) and network of carbides in (c), and (d) EDS elemental map of specimen

3.1.4.3 Oxide formation

In this s study, the EDS mapping of the material, particularly where non-metallic particles were observed, clearly indicates the presence of oxide particles, as shown Figure 39-a, and Figure 39-b. Notably, these oxide particles were not present, or were only present in very small amounts. While the shielding gas used during the additive manufacturing process was argon, which is typically used to prevent oxidation, studies have shown that even with argon, there is a potential for oxide layer formation in additively manufactured materials. In fact, oxide layers up to 60 micrometers thick have been reported by Jichang Xie et al. [120]. However, the more pronounced presence of oxide particles in the heat-treated material highlights a stronger dependency of oxide formation on the heat treatment process, particularly when the heating environment is not fully isolated.

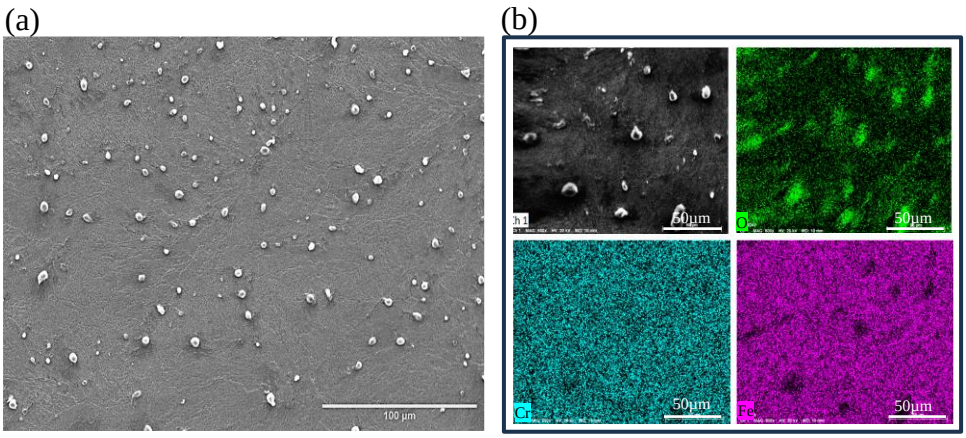

Figure 38. (a) SEM image of the nonmetal particles, and (b) EDS map of the particle

Additionally, the heat treatment process accelerates oxygen diffusion, particularly at elevated temperatures and with longer durations, as described by Fick's second law[170]. This study has shown after heat treatment, more oxide particles are observed compared to the as-built situation. This phenomenon is particularly more pronounced in regions corresponding to the laser tracks (or melt pool boundaries), what is clearly indicated in the optical microscopy structure of the as -built material in Figure 33-a. The easier passage of oxygen through melt pool boundaries in additively manufactured materials, which resemble grain boundaries, is due to the inherent characteristics of these regions. Grain boundaries and melt pool boundaries are less ordered and contain more defects compared to the well-aligned crystal structure within the grains. These defects lower the activation energy required for oxygen diffusion, allowing oxygen atoms to move more easily along these pathways during processes like heat treatment [171]. Additionally, during the rapid solidification process, alloying elements with a high affinity for oxidation tend to segregate towards the melt pool boundaries [120], further stimulating oxide formation. The high concentration of dislocations and thermal stresses at melt pool boundaries enhances this effect, making them preferential sites for oxygen diffusion. As a result, oxygen tends to accumulate and form oxides at these boundaries, which can weaken the material by acting as stress concentrators and crack initiation sites, ultimately compromising the mechanical integrity of the structure.

Microstructural analysis of the annealed samples revealed the presence of nonmetal particles, that has been shown to be oxide in a previous study of the authors. At 400°C, oxide particles appear sparsely, primarily at the end of the laser track, with sizes below 8µm (Figure 39-a). When the annealing temperature is raised to 550°C, more oxide particles appear (Figure 39-b). At 65°C, oxide nucleation and growth were observed at the grain boundaries, inside the laser track. Their average diameter was less than 8µm, as depicted in Figure 39-c. With an increase in time from 2 to 6 hours, there is a greater likelihood for oxide particle initiation or growth. Figure 40- a illustrates the SEM image of one oxide particle. Figure 40-c, and Figure 40-d illustrate the particle size distribution after annealing, at 550 °C and 650 °C after 6 hours, respectively. And in Figure 40-b, comparative box plot of oxide particles is given. At 650 °C, more but finer oxide particles with majority of them ranging from 2-6 µm were observed, compared to 550 °C where slightly larger particles ranging from 3-7 µm were present.

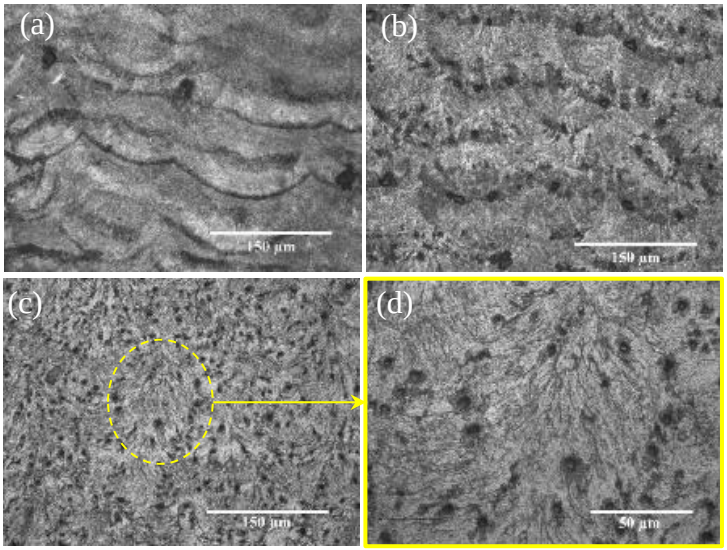

Figure 39. Optical microscopy image of the samples after annealing indicating oxide particles at (a) 400°C for 2 hours with sample code of SA1, (b) 550°C for 6 hours with sample code of SA4, (c) 650°C for 6 hours with sample code of SA5

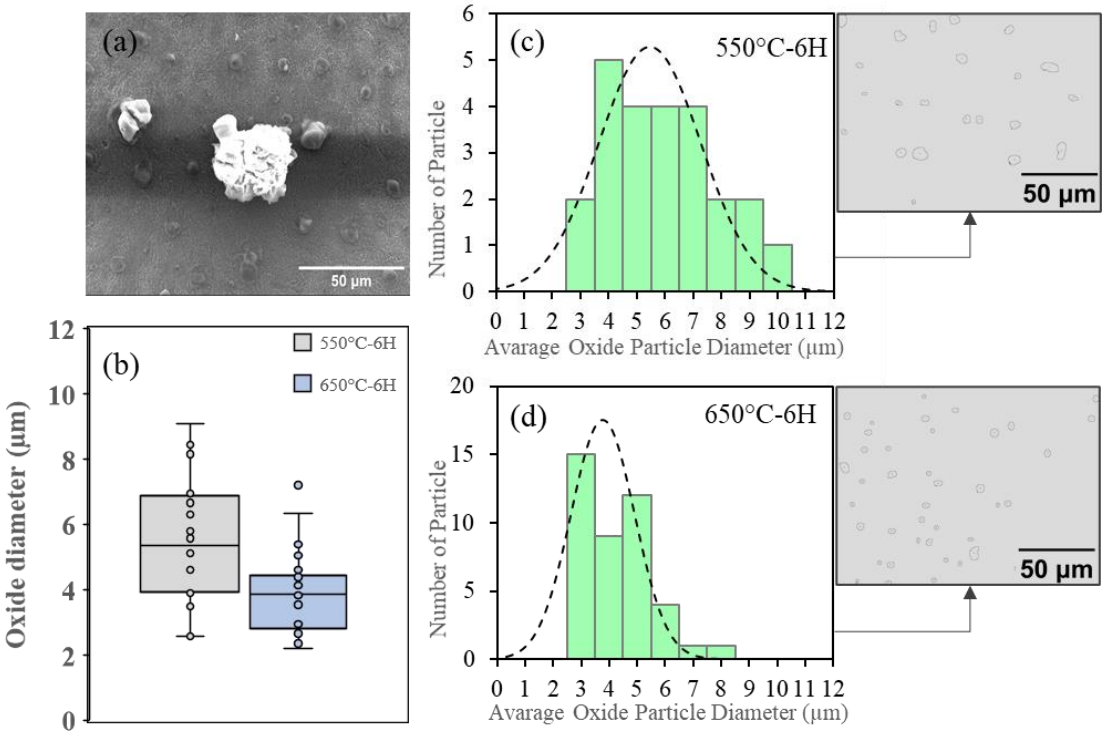

Figure 40. Oxide particle specifications including (a) high magnification SEM image (b) comparative box plot, and distribution in annealed specimens at (c) 550 °C for 6 hours with sample code of SA4, and (d) 650 °C for 6 hours with sample code of SA5

Figure 41-a illustrates the oxide particle size distribution in samples tempered for 2 hours at temperatures ranging between 500 °C and 650 °C. For all tempered samples, oxide particle sizes consistently remained below 12 µm. At 500 °C (Figure 41-b), the majority of particle sizes fell below 7 µm. At 550 °C (Figure 41-c), a substantial reduction in size was noted, with particles less than 4 µm and occasional outliers in the 11-12 µm range but the number of the particles increased. At 600 °C (Figure 41-d), the particle sizes exhibited an approximately normal distribution, ranging from 2-6 µm. At 650 °C (Figure 41-e), histogram of the particle size presents a matrix primarily composed of particles ranging from 3-8 µm, with a few outliers in the 9-11 µm range. Generally, the oxide particles in tempered specimens were smaller when compared to annealing at the same temperature, which is related to the lower cooling rate characteristics of the annealing process. thereby, allowing more time for the particles to grow.

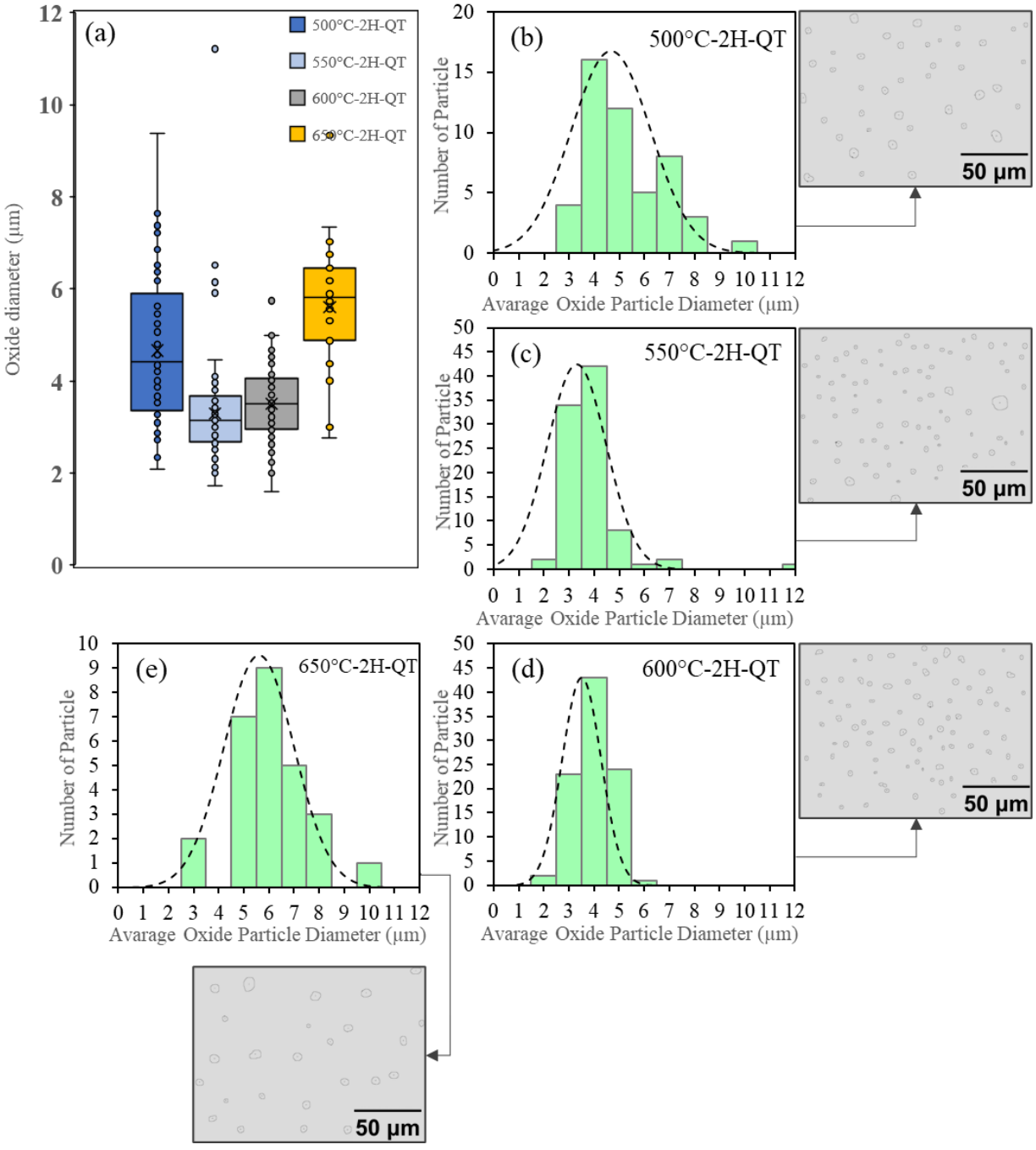

Figure 41. Oxide particle size distribution in tempered specimens during 2 hours at temperature of (a) 500°C with sample code of ST2, (b) 550°C with sample code of ST3, (c) 600°C with sample code of ST4, (d) 650°C with sample code of ST5

Figure 42 , shows the oxide particle size distribution for the samples that are subjected to both annealing and tempering with annealing at 500°C and 600°C for 2 hours, followed by (quenching and tempering) Q&T treatment at 550°C for 2 hours; Figure 42-b, Figure 42-c. The oxide particle size for annealing at 500°C is smaller than at 600°C respectively ranged between and 2-5 µm, 3-7 µm; Figure 42-a.

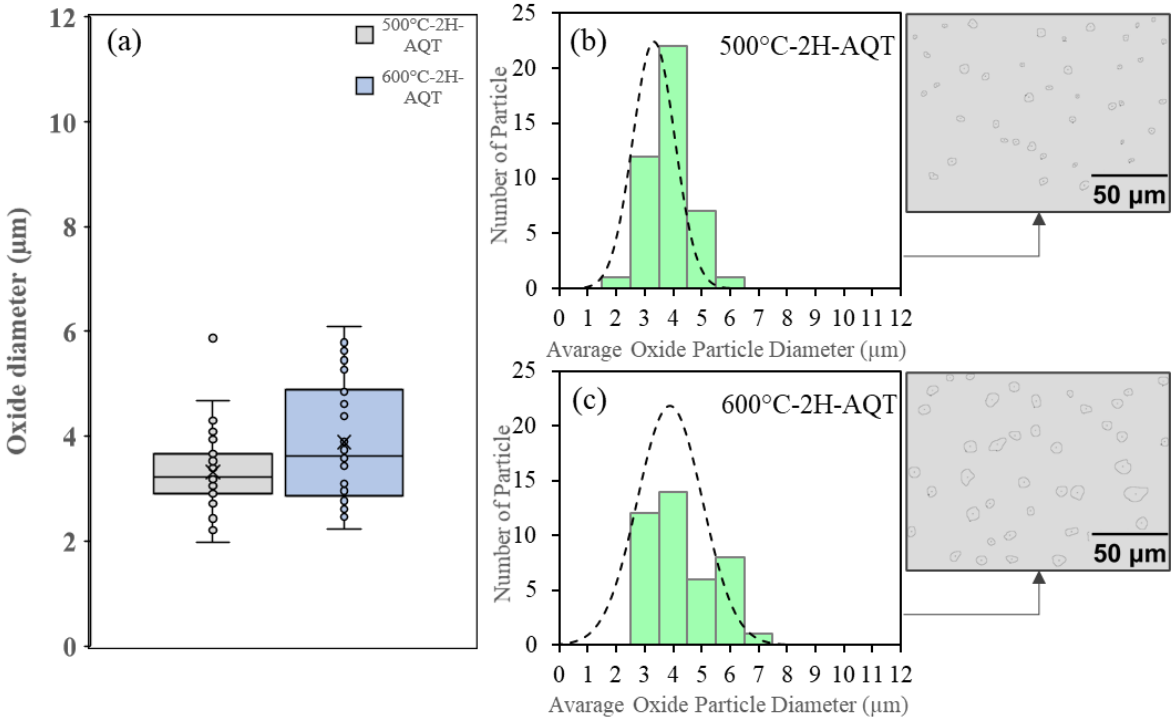

Figure 42. Oxide particle size distribution in annealed and QT-ed specimens with samples code of (a) SAT1, and (b) SAT2

Overall, the comparison between annealing and tempering processes revealed distinct differences in oxide particle formation. Annealing tends to produce fewer but larger oxide particles, whereas tempering, especially with quenching, resulted in a higher number of smaller oxides. For example, annealing at 550°C for 6 hours allows sufficient time for oxygen diffusion, led to a moderate number of oxide particles, typically ranging from 3 to 7 µm. This extended duration enabled more oxygen to penetrate the material, facilitating the formation of larger particles. On the other hand, quenching followed by tempering at 550°C for 2 hours led to a significantly higher number of oxide particles, although these are smaller, generally

less than 4 µm. The rapid cooling during quenching limited the time available for oxide particles to grow, resulted in a finer distribution. Notably, the number of oxides in this case was around 2 to 2.5 times greater compared to the 6-hour annealing, highlighting the different kinetics involved in each process.

Additionally, a comparison between materials that were annealed or tempered alone with those that undergone a combination of annealing followed by tempering reveals that pr-annealing altered the kinetics of oxide formation. Pre-annealing resulted in a lower number of oxide particles compared to tempering alone but a higher number than annealing alone. It is crucial to consider that the pre-annealing temperature played a key role in determining both the size and number of oxides. For example, pre-annealing at 500°C helped to reduce the oxide particle size compared to tempering alone, leading to smaller oxides. However, pre-annealing at 600°C promoted oxide formation, resulted in larger oxide particles than those formed through tempering alone. In summary, to minimize oxide formation in PBF-H13 steel, it is recommended to employ a heat treatment process that includes annealing at 500°C for 2 hours, followed by quenching and tempering at 550°C for 2 hours. This combination effectively could limit oxide particle growth, results in a fine distribution with minimal size, typically less than 4 µm, thereby potentially optimizing the material's mechanical properties and overall performance.

3.1.4.4 Sensitivity analysis of annealing treatment

As reported in Figure 43 annealing at 400°C resulted in minimal changes in UTS and elongation, compared to the as-built material. However, a significant increase in yield strength is observed, rising from 1029 MPa, for the as-built material, to 1244 MPa after annealing. Additionally, a slight increase in the elastic modulus is noted at this temperature, increasing from 189.3 GPa to 210 GPa. Despite minimal changes in the microstructure, the observed increase in Young’s modulus and yield strength under tensile loading signifies the material's increased ability to withstand elastic deformation, following annealing. This improvement can be attributed to the partial removal of compressive residual stresses as also

reported in previous studies [138, 139] .The result also is in alignment with the study of Qi Chao et al. [172] who reported that annealing at 400 °C effectively mitigates compressive residual stress in 316L austenitic stainless steel.

Within the temperature range of 400-550°C of annealing, a notable increase in UTS is observed compared to the as-built condition (Figure 43-b). It is interesting to note that, the cellular structure, carbides, and the oxide particles stay the same as observed in the as-built material. Thus, the increase in UTS can be attributed to the partial transformation of martensite into austenite, due to the temperature exceeding the martensite transformation point. Additionally, annealing in the 400-550°C range leads to a reduction in the Young's modulus and yield stress, compared to 400 °C (Figure 43-a, Figure 43-d). The negligible change in elongation is attributed to the constancy and oxide particles, along with minimal alterations in the microstructure (Figure 43-c). When increasing annealing time from 2 hours to 6 hours at 550°C, negligible change happens in cellular structure, accompanied by the emergence of slightly more oxide particles (Figure 39-b). These changes have a negligible impact on UTS, yield stress, and Young's modulus, and elongation, Figure 44-a to Figure 44-d.

For annealing temperature of 650 °C, changes in mechanical behaviour are more pronounced, characterized by a significant increase in elongation (3%) and a decrease in UTS (20 %), Figure 43-f, and Figure 43-g. These changes in UTS and elongation could be explained by the effect of carbide coarsening[173], similar to the one reported for wrought H13. Aa report by Ning et al. [174] and Lin et al.[175] , the refined carbides, which are evenly spread throughout the material's structure, could help restrict the movement of dislocations; thereby, improving the material's ability to deform plastically. Furthermore, comparing the oxide particles at 550 °C and 650 °C, the smaller oxide particles at 650 °C hinder crack initiation and propagation, and increase the elongation at this temperature .It

must be noted that the above microstructural changes have minimal effect on the yield stress and Young's modulus; as reported in Figure 43-e, and Figure 43-h.

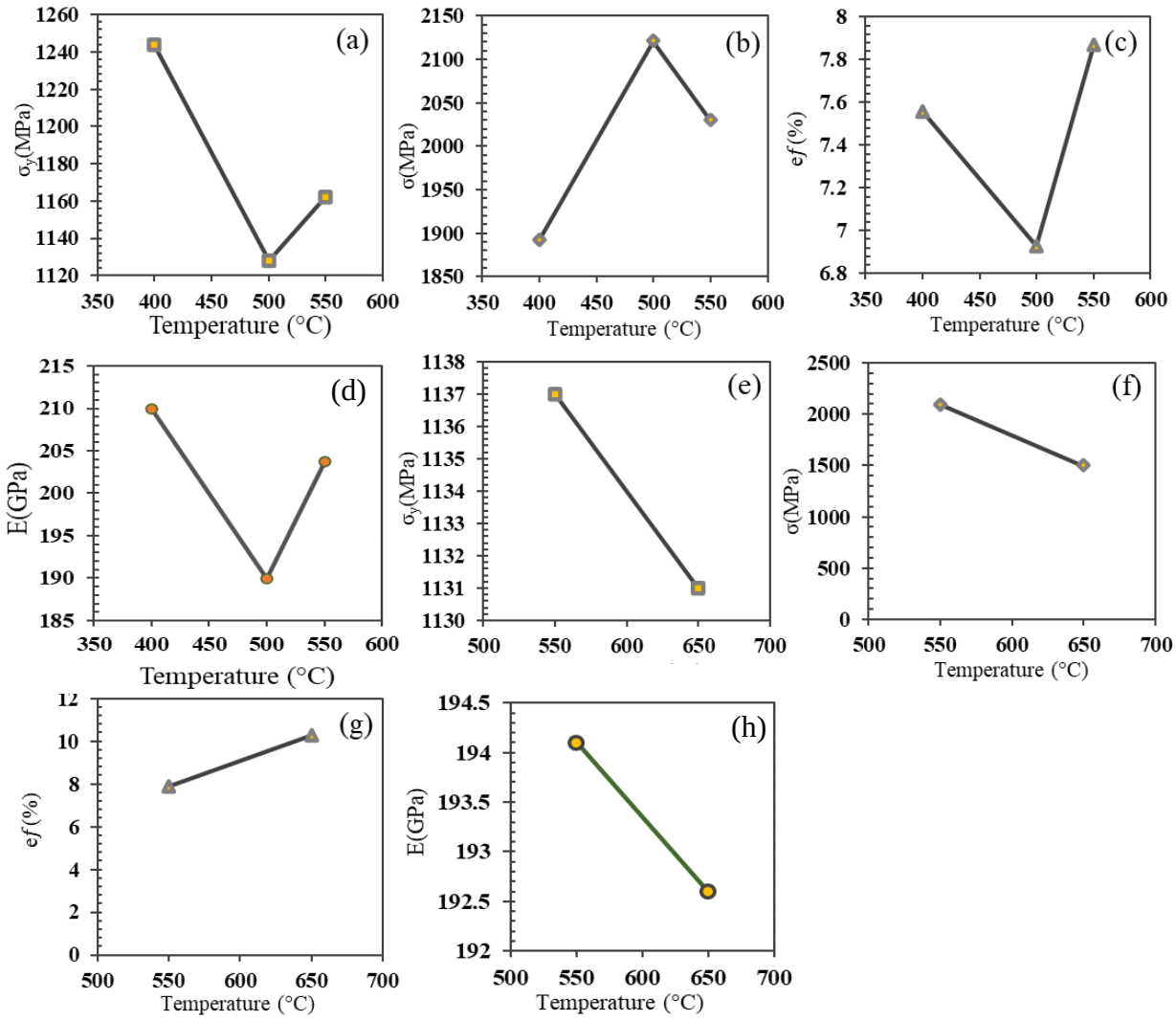

Figure 43. Sensitivity of mechanical properties to annealing temperature; (a)-(d) show the effects of temperature after 2 hours, and (e)-(h) show the effects after 6 hours

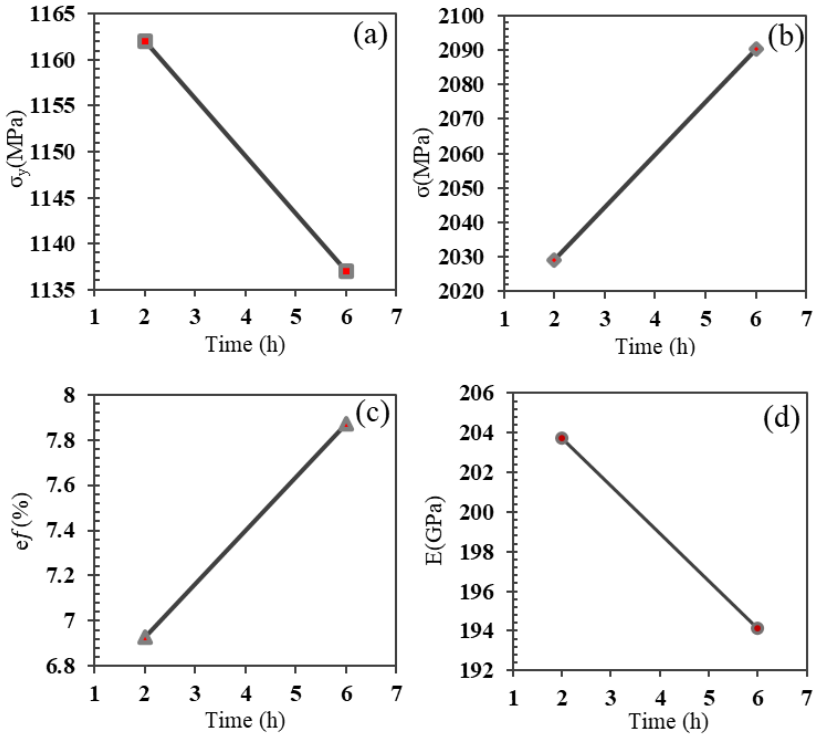

Figure 44. Sensitivity of mechanical properties to annealing time

3.1.4.5 Sensitivity analysis of tempering treatment

compared to Q&T-ed, specimens directly subjected to tempering at 550°C, exhibit a brittle behaviour, with a relatively low elongation of around 7% and a high UTS of approximately 2132 MPa. It has been reported [49] that the microstructure in non-quenched H13 samples for tempering at lower temperature, closely resembles that of annealed samples, featuring a cellular structure that causes also a high yield strength, 1260 MPa, but low elongation. In this scenario, the material's properties closely align with specimens subjected to annealing treatment, with a slight improvement, likely attributable to the smaller oxide particles, since air cooling offers limited opportunities for oxide particles to grow. The result shows the necessity of the quenching before tempering.

As presented in Figure 45-a when the tempering temperature increases from 550 °C to 750 °C, yield stress decreases from 1154.7 MPa to 621.2 MPa. This reduction can be

attributed to the transformation of martensite into softer microstructures, such as ferrite, pearlite, or retained austenite, at higher tempering temperatures.

In the temperature range of 550-750 °C, a gradual decrease in UTS is observed (Figure 45-b), while elongation shows minimal change except for 750°C (Figure 45-c), where the elongation significantly increased to 20.10%. Comparatively, the results of Yan Guanghua et al. [154] on forged H13 tempered within the same temperature ranges, reveal a gradual increase in elongation from approximately 5% to 18%, with UTS exhibiting a corresponding gradual decrease from 2200 to 1100 MPa. In their study, optimal mechanical properties, was obtained at 650°C, with an elongation of approximately 15% and a UTS of 1100 MPa. When comparing these results with those obtained in the present work for PBF-ed H13, it becomes evident that the elongation of PBF-ed samples exhibit less improvement by increasing tempering temperatures from 550-650 °C. The observed elongation ranges from 13-15% (showing negligible change), and UTS ranges from 939 to 1485 MPa. Meaning that the material is more sensitive to the failure. This higher sensitivity of UTS and elongation in PBF-ed H13 to the tempering temperature has also been reported by Juie Yan et al. [49]. This phenomenon can be attributed to the presence of oxide particles, acting as sites for crack initiation. At 550 °C, a good balance between UTS and elongation is achieved due to the minimum oxide particle size. However, as the temperature is increased to 650°C, the average particle size rises (majority 4-8 µm, Figure 41-d), hindering the increasing effects of precipitation of secondary phases elongation. Simultaneously, UTS decreases due to both the presence of secondary phases and crack initiation sites by oxide presence. This results in a UTS value of 939.82 MPa at 650°C, which falls below the desirable range when compared to conventional part.

As presented in Figure 45-c, at a tempering temperature of 500°C, a notable enhancement in elongation has occurred, which is doubled to 14%. This improvement could be attributed to significant microstructural changes that took place during the Q&T process. The elongation after tempering is facilitated by the precipitation of secondary phases and the transformation of retained austenite into more stable phases. Also, during tempering, the

diffusion of atoms within the martensitic structure is promoted. This leads to the formation of secondary phases, such as carbides. The carbides within martensite matrix contribute to overall strengthening of the material and help improve toughness by inhibiting crack propagation. However, the UTS reduces from 1859 MPa, for as-built material, to 1520 MPa. This finding could be due to both the presence of tempered martensite and the emergence of fine oxide particles, ranging between 2 to 10 µm (Figure 41-a). At 550°C (Figure 45-c), there is slight increase in elongation, attributed to the reduction in oxide particle sizes, compared to tempering at 500°C (Figure 41-a, Figure 41-b). It is noteworthy that at this temperature, there is a reduction in the size of oxide particles, while the overall number of oxides increases. This highlights the material's sensitivity to particle size rather than volume fraction. Within this range, with a majority of oxide particles measuring 2-4 µm, particularly obtained at 550°C, the material achieves an optimal balance between mechanical strength and elongation. from 550 °C to 750 °C the elongation increased significantly to 20%.

As presented in Figure 45-d, the variation observed in Young's modulus appears to be minor compared to the significant changes observed in other mechanical properties such as elongation and yield stress, and UTS.

As presented in Figure 46, With increasing the tempering time from 2 hours to 6 hours, there is decrease in UTS, elongation, and yield stress to respectively 1230 MPa, 14%, and 621 MPa (Figure 46-a to Figure 46-c). The governing mechanism in this case is similar to the one operating when increasing the tempering temperature. Six hours allows more time for oxide particle growth and more carbide formation, so favouring crack initiation, and decreasing the strength of the material.

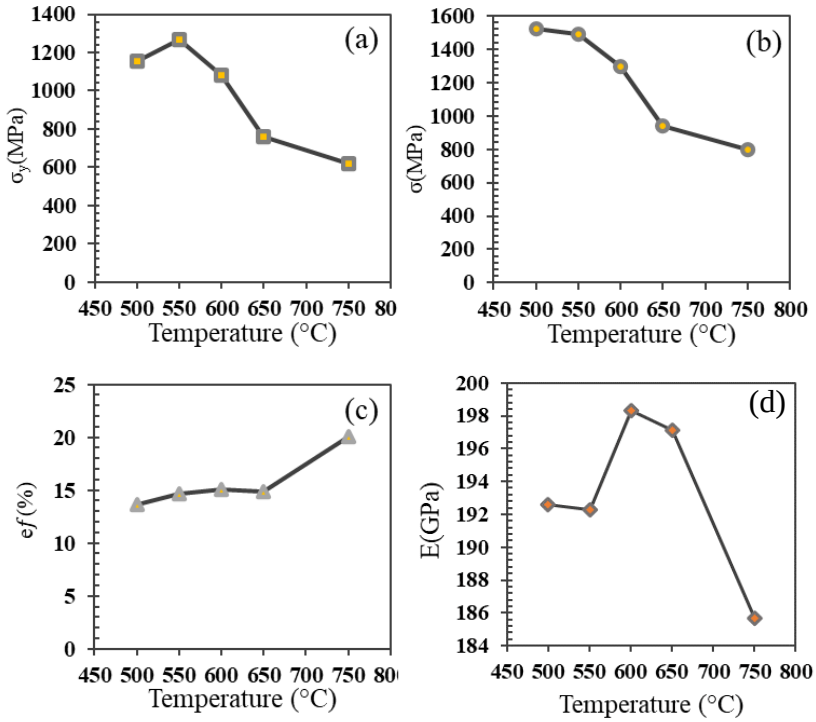

Figure 45 Sensitivity of mechanical properties to tempering temperature

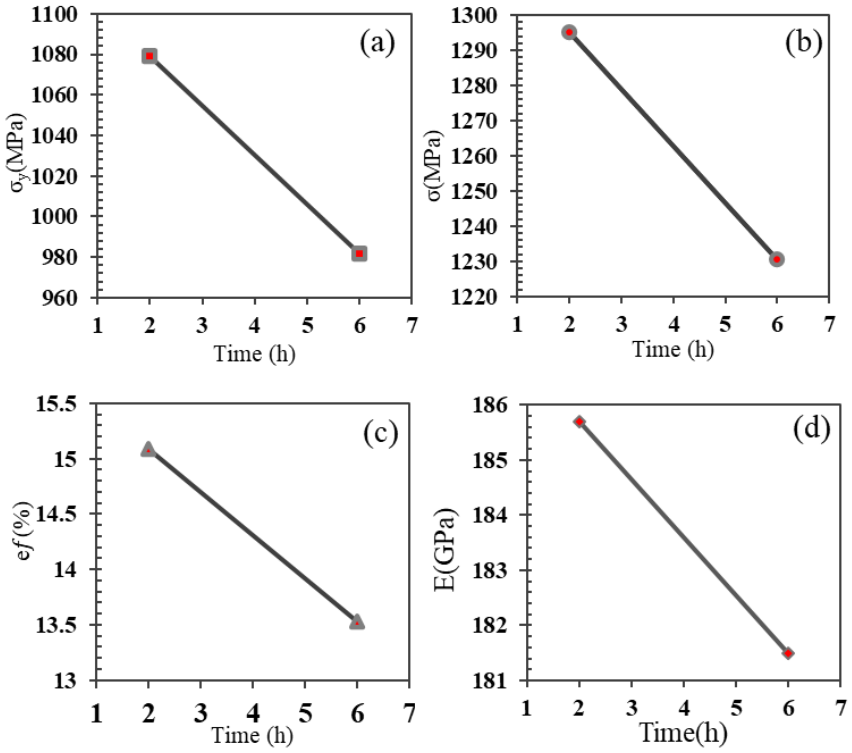

Figure 46 Sensitivity of mechanical properties to tempering time

3.1.4.6 Sensitivity analysis of the annealing treatment before tempering treatment

Comparing the results of annealed specimens with Q&T-ed specimens, annealing treatment alone may not provide sufficient ductility for the material. In the present work, it was found that by conducting annealing before Q&T is an effective method to further improve the mechanical strength of the PBF-ed material. To explain such improvement, the role of undissolved carbides in the metal matrix must be considered. In conventional H13, undissolved carbides can play crucial roles during austenitization. They can prevent grain coarsening, resulting in a fine microstructure after quenching and strengthen the material. Conversely, coarse undissolved carbides can act as crack nucleation sites and weaken the material [43, 176]. The effect of the annealing temperature before Q&T on the mechanical strength of conventional H13 was investigated by Jian Zhu et al. [177]. The authors reported that, annealing at 640°C for 10 minutes and subsequent tempering at 600°C for 30 minutes significantly improved the mechanical properties (by keeping the UTS and elongation above 83% of the initial material). In contrast, annealing at 700°C reduced the mechanical strength, due to increased sizes of Cr-rich and V-rich carbides as well as higher volume fraction of austenite. The authors also found that a higher pre-tempering treatment temperature (around 620-740°C) improved the mechanical properties of wrought H13 before tempering.

In the case of PBF-ed H13, the observed oxide particles during austenitization would be an additional damaging factor. Figure 47-a to Figure 47-a -d show a comparison of the tensile properties of the specimens with prior annealing at 500°C and 600°C plus subsequent tempering at 550°C, respectively. Annealing around 600°C, reversed the mechanical properties after subsequent quenching and tempering processes by reducing the UTS and elongation to 1429.86 MPa, and 14%, respectively. In contrast, annealing at 500°C, increased the UTS to 1517 MPa and the elongation to 15%. The above findings could be explained by considering the balance between three phenomena: residual stress removal, oxide particle size, and carbide size [138, 139] reported the presence of high compressive residual stresses in the as-built material. The stress distribution during quenching is therefore influenced by the presence of these residual stresses and could lead to crack formation [178]. By annealing

at 550°C, the residual stresses are removed, or at least significantly reduced, thereby, contributing to the mechanical strength improvement. At 600°C, more stress removal is

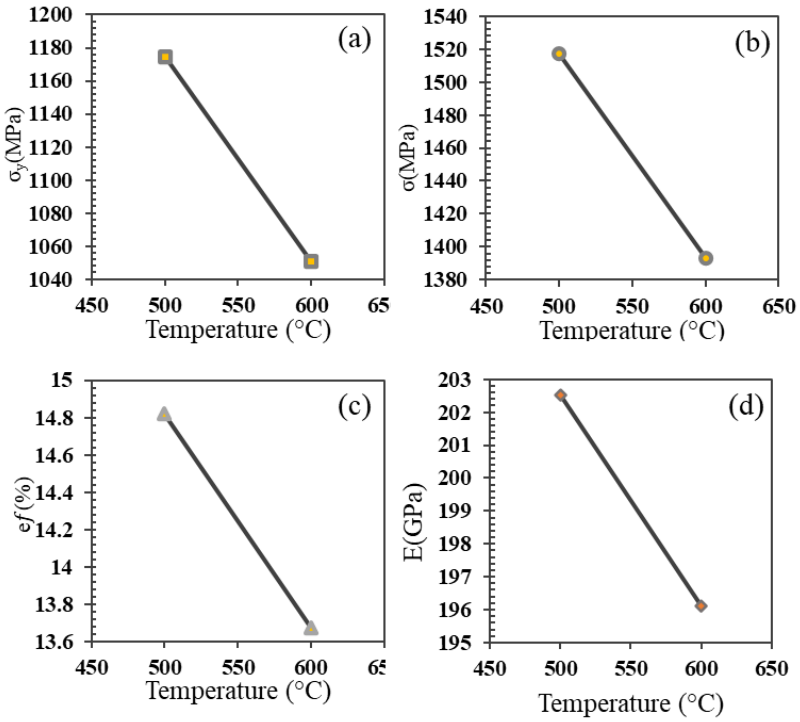

Figure 47. Sensitivity of mechanical properties of the specimens that are subjected to the annealing before QT at different annealing temperature

expected to take place, but the increased size of the oxide particles promotes crack nucleation and propagation during quenching, thus, reducing the overall mechanical strength. Although, the evolution of carbide size was not extensively studied in the present work; however, it appears that the negative effect of oxide particle size growth is destructive enough to the material and lead to significant damage and masks somehow, the effect of carbides. An additional factor that could have contributed to the observed reduction in UTS at this temperature is the dissolving of the cellular structure at around 600°C. Indeed, as reported by reference [179], these structures contribute to the strength of PBF-ed materials by a Hall-Petch type effect.

3.1.4.7 Fractography

The tempered sample without quenching (Figure 43-a), show a granular and featureless surface, which suggests a brittle fracture. Brittle fractures typically occur with little to no plastic deformation, and the surface often shows a flat and shiny appearance due to the sudden rupture of bonds along crystalline planes. This kind of fracture often propagates rapidly, with the crack following the path of least resistance, which is usually along the material's natural crystalline boundaries. The absence of significant plastic deformation, the presence of river patterns, and the granular texture are all indicative of a brittle material response to stress.

In contrast, the fracture surface of sample tempered with quenching (Figure 48-b), show a rougher feature which could imply a minute amount of ductility or, at least, a higher material toughness. This could be due to the material having a small amount of plastic deformation before fracturing or a tougher microstructure that required more energy for the crack to propagate. The surface doesn't display the same level of the granular, flat facets, suggesting that the material absorbed more energy during the fracture process. This can be attributed to the higher volume fraction of martensite and the potential presence of fine alloy carbides precipitated during tempering, which contribute to secondary hardening [154].

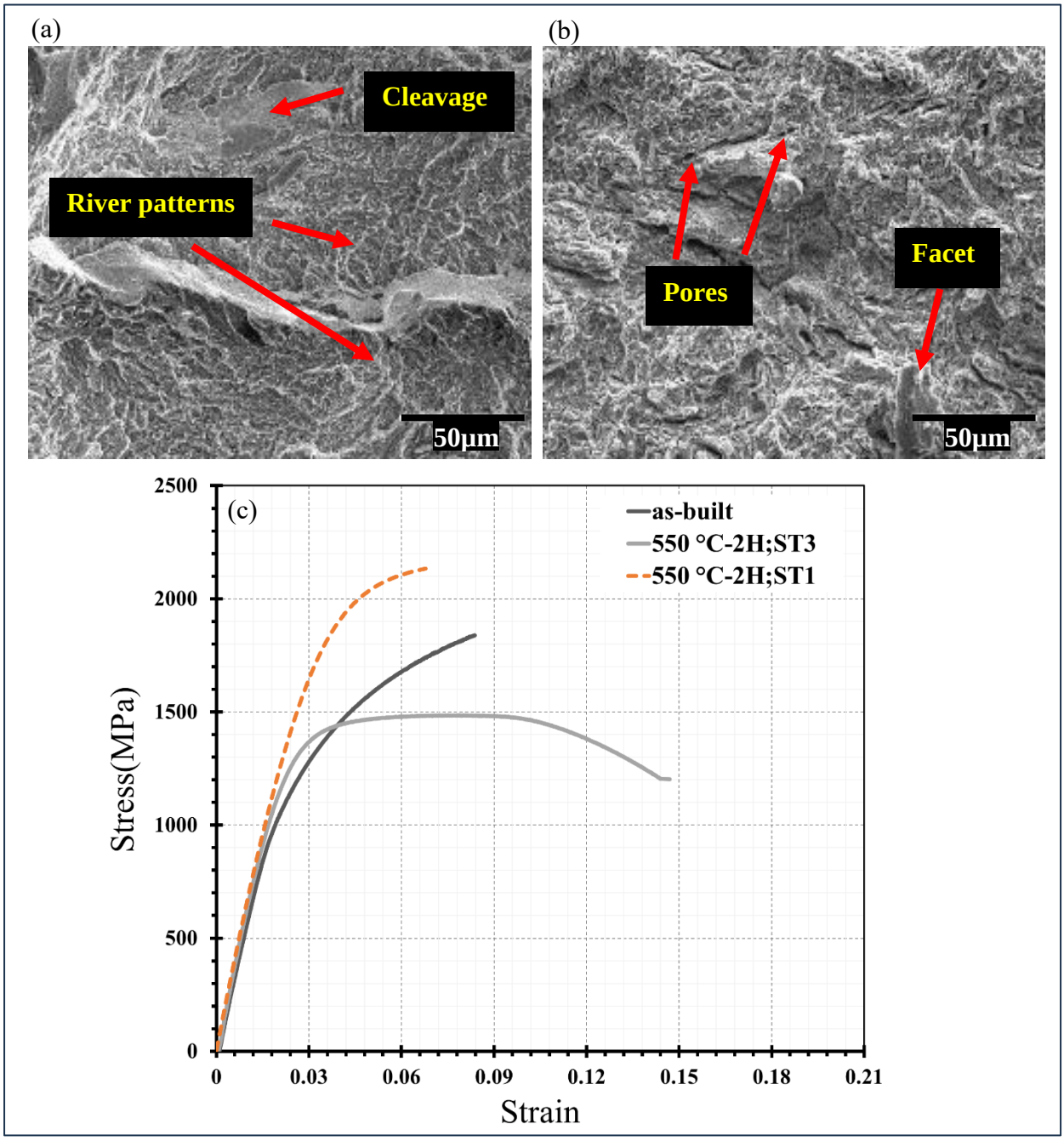

Figure 48. SEM fractography image of (a) tempered samples -with out quenching (ST1), and (b) quenched and tempered at 550°C (ST3)

Figure 49 shows the fractography image of the quenched and tempered samples for different tempering conditions (ST2, ST4, ST5, ST6, ST7). For the specimen tempered at 500°C for 2 hours (Figure 49-a), the fractured surface shows a network of fine dimples, typical of a ductile fracture. The uniformity of the dimples suggests that the sample has undergone a uniform transformation during tempering, likely resulting in tempered martensite or bainite [180]. The steel has likely retained a fair amount of toughness due to the tempering at a relatively low temperature for an extended period, which relieves stresses within the martensite and reduces its brittleness while still maintaining some of the hardness. In fractography image of the specimen tempered at 600°C for 2 hours (Figure 49-b), the structure appears to have larger, more pronounced dimples, with some areas showing tearing ridges. This indicates a more pronounced plastic deformation prior to fracture, which can be attributed to the higher tempering temperature that allows for the relaxation of more internal stresses and possibly the coarsening of carbides [181]. The tearing ridges suggest localized areas of intense plastic deformation, which may reflect inhomogeneities in the microstructure or the presence of residual stresses.

Fractography image of the specimen tempered at 600°C for 6 hours (Figure 49-c), shows a significant change in the fracture surface. The prolonged exposure to the tempering temperature has likely resulted in over-tempering, where the carbides coalesce and grow larger, reducing the toughness of the steel. The surface is characterized by a fibrous appearance, which is indicative of a decrease in ductility. The longer tempering time at this temperature probably led to the depletion of carbon in the matrix and growth of carbide particles, making the steel more brittle. For the specimen tempered at 650°C for 2 hours (Figure 49-d), the fracture surface has a mixture of ductile and brittle features. There are regions with dimpled rupture indicating ductile behavior, as well as areas that appear flat and featureless, which are typical of brittle fracture. This suggests that the tempering temperature and time have resulted in a microstructure that is at a transitional phase between high ductility and brittleness. The microstructure of the specimen tempered at 750°C for 2 hours (Figure 49-e), has transformed significantly, showing a more ductile fracture surface. The presence

of larger and more irregular features suggests that the primary mechanism of fracture may have shifted toward a more ductile mode, with more plastic deformation occurring before failure. This can be a result of the tempering temperature being close to the secondary hardening peak, resulting in a harder yet more brittle microstructure.

The sample subjected to annealing before QT at 500°C (Figure 50-a) reveals a predominantly ductile fracture surface, characterized by a dense population of small, uniformly distributed dimples. These dimples are indicative of microvoids coalescence, a process where voids form around stress concentrators like carbides or inclusions and grow under tensile stress until the material ultimately fails. The uniform size and shape of the dimples suggest that the material was subjected to a uniform stress state with good toughness and plastic deformation before the fracture occurred. The absence of any significant secondary features, such as river patterns or flat facets, also reinforces the ductile nature of the failure. At 500 °C, the tempering would be expected to relieve internal stresses and result in a tempered martensite structure with fine carbides [182], which enhance the toughness of the steel. In contrast, the fractography of the sample tempered at 600°C (Figure 50-b) shows a more rugged and coarser dimpled texture. The decreased size and depth of the dimples, as well as the presence of more pronounced tearing ridges, point towards a lower degree of plasticity and energy absorption before fracture. This suggests that tempering at the higher temperature provided the steel with greater toughness, as the higher tempering temperature allows for more complete stress relief and the growth or coalescence of carbides. However, the coarser dimples and tearing ridges could also indicate the beginning of over-tempering, where the secondary hardening effect diminishes and some of the alloy carbides may dissolve into the matrix, potentially reducing the yield strength but increasing ductility. The fracture surface does not exhibit signs of intergranular failure or brittle features, which would be expected if the tempering temperature had led to significant embrittlement or if the steel had been subject to thermal fatigue. In both images, the evidence of ductile fracture is an indication of the material's ability to withstand significant deformation prior to failure, which is an important characteristic in many of the high-temperature applications where H13 tool steel is used.

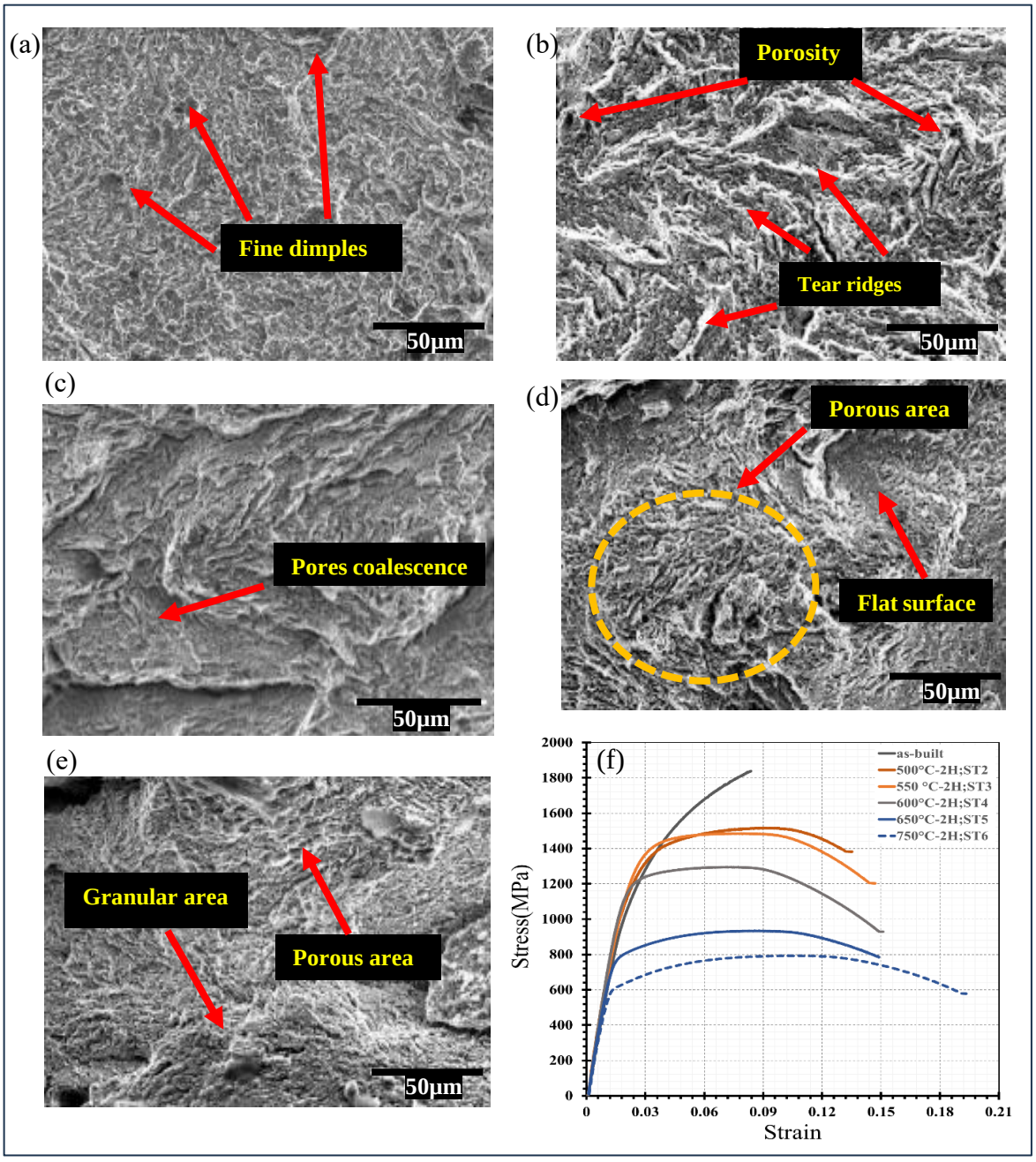

Figure 49. SEM fractography image of the samples at different temperature and time (a) 500°C for 2 hours (ST2), (b) 600°C for 2 hours (ST4), (c) 600°C for 6 hours (ST7), (d) 650°C for 2hours (ST5), (e) 750°C for 2 hours (ST6)

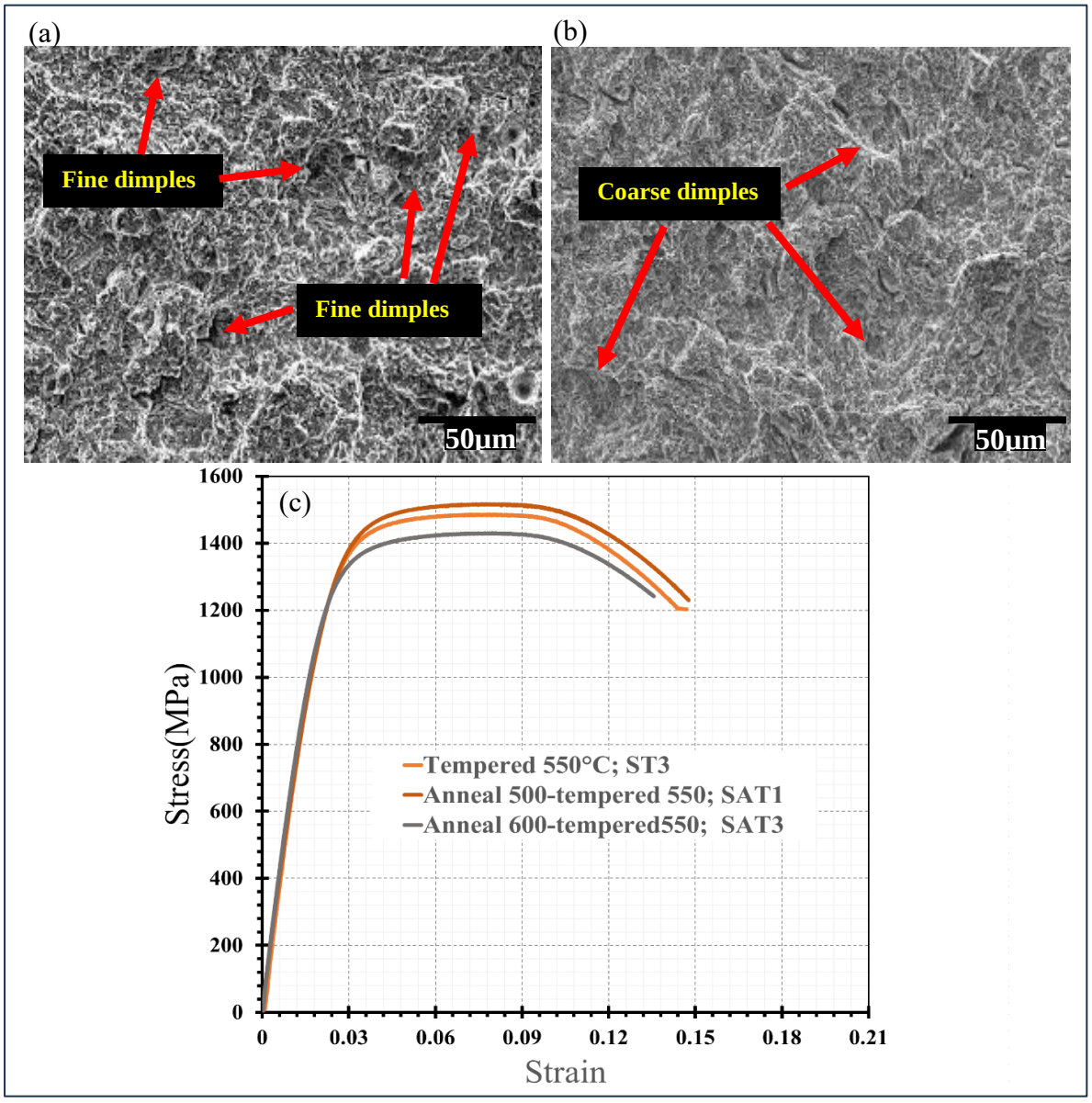

Figure 50. SEM fractography image of the samples subjected to annealing before QT at (a) 500°C for 2 hours, and (b) 600°C for 2 hours

3.1.5 **Conclusion**

In this study, the effect of annealing and tempering treatment on mechanical behaviour of PBF-ed H13 was thoroughly examined and compared to those of wrought H13.The following conclusions may be drawn:

1. A minimum annealing temperature of 500°C is necessary for a significant elimination of residual stresses. Temperatures exceeding this threshold may led to increase in toughness but reduction in UTS could occur.
2. Single annealing treatment is not recommended in cases the PBF-ed material is to undergo high plastic deformation.
3. Tempering treatment without prior quenching would not be sufficient to provide adequate ductility to the PBF-ed H13 material.
4. A post quench tempering treatment at 550°C for 2 hours is proposed to achieve the optimum balance between elongation and UTS.
5. An annealing treatment at 500°C, before Q&T, has proven to be a promising method for enhancing mechanical strength. Temperatures above this threshold lead local stresses and initiating cracks during quenching.

CONCLUSION GÉNÉRALE

Dans cette étude, l'objectif principal était d'optimiser les propriétés mécaniques de l'acier H13 fabriqué par des méthodes PBF. Pour atteindre cet objectif, trois objectifs ont été définis. Le but du premier objectif était d'effectuer une revue complète de la littérature sur le processus de PBF et le traitement postérieur applicable à l'acier H13 fabriqué par PBF. Le deuxième objectif était d'optimiser les paramètres de SLM pour maximiser les performances mécaniques du matériau. Enfin, le troisième objectif était d'améliorer les propriétés mécaniques avec des processus de traitement thermique postérieur. Ces objectifs ont été abordés respectivement dans la phase 1, la phase 2 et la phase 3. Les résultats sont résumés comme suit :

La première phase comprenait une revue exhaustive de la littérature visant à fournir des informations sur le potentiel de l'acier H13 fabriqué de manière additive dans l'industrie. De plus, une étude approfondie du processus de SLM, couvrant les défauts de fabrication, la densité relative, l'évolution microstructurale, le comportement mécanique et les post-traitements visant à améliorer les propriétés mécaniques. L'objectif principal était d'identifier les lacunes de recherche et les domaines inexplorés dans ce domaine. Les résultats de l'étude valident les conceptions innovantes des canaux de refroidissement conformes (CCC), démontrant leur efficacité pour améliorer la productivité des moules d'injection plastique fabriqués à partir de H13, mettant ainsi en évidence le fort potentiel de demande pour le H13 fabriqué par PBF. En ce qui concerne le processus de SLM lui-même, de nombreuses recherches se sont concentrées sur l'optimisation des paramètres de traitement pour obtenir une densité relative maximale et améliorer la résistance mécanique comparable à celle du H13 conventionnel. Cependant, malgré ces efforts, les performances mécaniques du H13 fabriqué tel quel restent inférieures à celles de son homologue conventionnel, caractérisées par la fragilité et la faible résilience dues à la forte fraction volumique de martensite résultant

du refroidissement rapide pendant le traitement. De plus, la présence d'austénite résiduelle dans le matériau tel que construit pose des défis, car elle se transforme en martensite sous charge dynamique, entraînant une instabilité dimensionnelle ou des fissures. De plus, des champs de contraintes résiduelles variables dans le matériau, depuis la plaque de base jusqu'à la dernière couche imprimée, ont eu lieu, passant d'une contrainte de traction élevée à une contrainte résiduelle compressive. Bien que le comportement mécanique du matériau sous des essais de traction uni-axiale puisse ne pas répondre aux exigences industrielles, sa résistance supérieure à la fatigue thermique par rapport au H13 forgé est remarquable, attribuée à la structure unique du H13 fabriqué par PBF. Les études de micro-dureté révèlent que le H13 fabriqué par SLM présente une dureté élevée, comme prévu en raison de la présence d'une teneur élevée en phase martensitique. Cependant, la microstructure diffère de celle du H13 conventionnel, modifiant la réponse du matériau aux traitements tels que la température de revenu. L'étude des différents traitements thermiques a montré, notamment, que le H13 conventionnel est plus sensible aux changements de température, tandis que l'allongement et la résistance à la traction ultime du H13 fabriqué par PBF montrent moins de sensibilité aux variations de température. Les résultats de la première phase mettent en évidence des lacunes significatives dans ce domaine, notamment le manque d'études sur les effets des paramètres de traitement sur l'évaluation de la porosité, la ségrégation des éléments, la formation de "balling", et l'homogénéité microstructurale, et leurs impacts ultérieurs sur les performances mécaniques du H13 fabriqué par PBF.

Dans la deuxième phase, qui vise à répondre au deuxième objectif et à optimiser les paramètres de traitement pour améliorer les propriétés mécaniques, la compréhension des corrélations entre les paramètres du processus PBF et les performances de l'acier à outils H13 a été approfondie. Cette phase s'est concentrée sur l'étude des effets des paramètres de traitement sur la porosité, la ségrégation des éléments, la formation d'oxydes, et leur relation avec le comportement mécanique du H13 fabriqué par PBF. L'étude a révélé la formation de pores en forme de trou de serrure, de porosités gazeuses, et de manque de fusion dans le H13 fabriqué par PBF, leur emplacement variant en fonction de l'EDV, notamment près de la surface. Ces défauts, en particulier le manque de fusion et la porosité gazeuse, ainsi que la

formation de pores en forme de trous de serrure près de la surface, ont influencé de manière significative la résistance mécanique. Une valeur critique de l'EDV de 57 J/mm³ a été identifiée, minimisant les trois défauts ; des valeurs plus faibles ont entraîné la formation de LOF, tandis que dépasser cette valeur a conduit à des porosités de trous de serrure et de gaz significatives. De plus, l'étude a souligné l'impact du phénomène de "balling" sur la ségrégation des éléments et l'inhomogénéité microstructurale. Une formation accrue de "balling" a facilité le mouvement des éléments d'alliage dans le bain de fusion, entraînant une homogénéité microstructurale accrue, en particulier à des valeurs élevées d'EDV. Il a été démontré qu'atteindre une résistance mécanique maximale, y compris une résistance à la traction ultime (UTS) et un allongement, est réalisable lorsque la ségrégation des éléments est minimisée, la taille des particules d'oxyde est réduite au minimum, et que les défauts près de la surface sont absents. Cet accomplissement a été réalisé dans la plage d'EDV de 57 à 59 J/mm³, incorporant des paramètres de traitement spécifiques tels qu'une puissance laser de 250W, un espacement des points de 0,12 µm, et une vitesse de laser de 800 mm/s. Ces paramètres ont démontré des propriétés mécaniques supérieures, caractérisées par des défauts minimaux près de la surface et une formation de "balling" réduite. De plus, l'étude a démontré que l'analyse cartographique de la micro-dureté constitue un indicateur fiable pour évaluer l'homogénéité microstructurale. En particulier, les zones avec une formation sévère de "balling" présentent des gradients plus importants dans le profil de micro-dureté, soulignant l'importance de la cartographie de la micro-dureté dans l'évaluation du matériau H13 fabriqué par PBF.

La troisième phase de cette étude visait à répondre au troisième objectif, qui était de concevoir un traitement thermique approprié pour l'H13 fabriqué par Fusion sur Lit de Poudre (FLP). Cette phase explore les effets des traitements de recuit et de revenu sur les propriétés mécaniques du H13 tel qu'il est fabriqué, visant à traiter la fragilité inhérente du matériau et à améliorer ses performances. L'étude met en évidence que le traitement de recuit réduit efficacement les contraintes résiduelles compressives dans le H13 fabriqué par FLP, avec des températures commençant à 500°C et plus. Cependant, des températures plus élevées éliminent davantage de contraintes résiduelles, mais augmentent le risque de

croissance des particules d'oxyde, réduisant ainsi la résistance mécanique. En outre, le traitement de revenu sans trempe préalable s'avère insuffisant pour améliorer la ductilité, car la température et le temps ne sont pas suffisants pour entraîner des changements significatifs dans la microstructure. La trempe suivie d'un traitement de revenu modifie radicalement la microstructure du matériau, le transformant en martensite revenue et améliorant l'allongement. Avec l'augmentation de la température de revenu, l'allongement augmente tandis que la résistance à la traction ultime diminue. Des conditions optimales sont observées à 550°C pendant 2 heures pour obtenir un équilibre modéré entre la résistance à la traction ultime et l'allongement. Le traitement de recuit avant trempe et revenu montre des promesses dans l'amélioration de la résistance mécanique, en particulier à 500°C, car la haute contrainte résiduelle du matériau tel qu'il est fabriqué est partiellement éliminée, empêchant la formation de microfissures pendant la trempe. Dans l'ensemble, l'étude souligne l'importance des traitements de recuit, de revenu et de trempe dans l'optimisation des propriétés mécaniques du H13 fabriqué par FLP, en mettant l'accent sur l'importance d'un contrôle précis de la température et du temps pour obtenir les propriétés mécaniques souhaitées tout en atténuant les inconvénients potentiels.

Basé sur les conclusions de cette étude et dans le but de favoriser les collaborations futures dans ce domaine, les recommandations suivantes sont proposées pour les prochaines recherches. Ces suggestions sont censées faciliter les progrès et contribuer de manière significative au corpus de connaissances existant.

Les perspectives sont présentées comme suit :

- Pour les études futures, il est impératif d’approfondir la relation entre la ségrégation des éléments et les champs de contraintes résiduelles, car cet aspect reste relativement peu exploré.
- De plus, des investigations supplémentaires sont nécessaires pour comprendre comment la ségrégation des éléments influence la résistance à la fatigue du matériau dans des conditions de température ambiante et élevée,

particulièrement pertinentes pour les conditions de travail des moules d'injection plastique.

- En outre, bien que l'impact de la formation de boules sur la finition de surface finale ait été identifié dans notre étude, une analyse quantitative de la rugosité de surface est encore nécessaire pour évaluer de manière exhaustive ses effets.
- De plus, étant donné la complexité de l'optimisation de ces phénomènes, il convient d'envisager d'imprimer de véritables canaux de refroidissement dans les recherches futures pour évaluer les performances du matériau dans des applications pratiques. Ces recommandations visent à combler les lacunes existantes dans les connaissances et à améliorer notre compréhension des interactions complexes au sein des processus de fabrication additive pour l'acier à outils H13.
- Une étude métallurgique plus détaillée axée sur les types et la morphologie des oxydes est essentielle, ainsi que l'exploration de leur relation avec la micro-dureté et les propriétés mécaniques.
- De plus, l'utilisation d'analyses de diffraction des rayons X (DRX) et de diffraction d'électrons rétrodiffusés (EBSD) pourrait fournir des informations précieuses sur les effets de ces paramètres sur les caractéristiques microstructurales, y compris la taille des grains et leur orientation. Cette technique avancée permet un examen détaillé des caractéristiques cristallographiques à l'intérieur du matériau.
- De même, l'évaluation de la distribution des carbures est nécessaire pour justifier les changements dans le comportement microstructural et mécanique. Quantifier et mesurer les contraintes résiduelles après ces traitements, en tenant compte notamment des effets du temps et de la température, renforcerait davantage la compréhension.
- En outre, l'étude de la combinaison du processus de pressage isostatique à chaud (HIP) avec le durcissement de surface pourrait conduire à des améliorations supplémentaires de la résistance mécanique.

- Enfin, l'intégration d'outils d'intelligence artificielle (IA) pour l'analyse des données dans les études futures peut aider à prédire la microstructure et les paramètres de traitement pour obtenir des propriétés mécaniques souhaitables. En utilisant des algorithmes d'IA et des techniques d'apprentissage automatique, il est possible d'analyser efficacement de grands ensembles de données pour identifier des modèles et des corrélations, améliorant ainsi notre capacité à optimiser les processus de fabrication pour l'acier à outils H13. En prévoyant les caractéristiques microstructurales et en sélectionnant les conditions de traitement optimales, l'IA peut contribuer au développement de matériaux haute performance en fabrication additive.
- Après avoir pris en compte tous les aspects, la prochaine étape cruciale consiste à étudier un cas réel de moule fabriqué en acier H13 par PBF, applicable dans l'industrie de l'injection.

RÉFÉRENCES BIBLIOGRAPHIQUES

[1] H. Rees, *Injection Mold Design*. Munich: Hanser Publishers, 2001.

[2] G. S. Phull, S. Kumar, and R. Walia, "Conformal cooling for molds produced by additive manufacturing: a review," *International Journal of Mechanical Engineering and Technology,* vol. 9, no. 1, pp. 1162-1172, 2018.

[3] X. Chen, Y. Lam, and D. Li, "Analysis of thermal residual stress in plastic injection molding," *Journal of Materials Processing Technology,* vol. 101, no. 1-3, pp. 275-280, 2000.

[4] https://news.ewmfg.com/blog/components-of-an-injection-mold (accessed.

[5] K. Altaf, A. M. A. Rani, and V. R. Raghavan, "Prototype production and experimental analysis for circular and profiled conformal cooling channels in aluminium filled epoxy injection mould tools," *Rapid Prototyping Journal,* vol. 19, no. 4, pp. 220-229, 2013.

[6] G. R. Berger, D. Zorn, W. Friesenbichler, F. Bevc, and C. J. Bodor, "Efficient cooling of hot spots in injection molding. A biomimetic cooling channel versus a heat-conductive mold material and a heat conductive plastics," *Polymer Engineering & Science,* vol. 59, no. s2, pp. E180-E188, 2019.

[7] C.-C. Kuo and Z.-F. Jiang, "Numerical and experimental investigations of a conformally cooled maraging steel injection molding tool fabricated by direct metal printing," *The International Journal of Advanced Manufacturing Technology,* vol. 104, no. 9, pp. 4169-4181, 2019.

[8] K. Chil-Chyuan, J. Zi-Fan, Y. Xin-Yi, C. Shao-Xuan, and W. Jia-Qi, "Characterization of a direct metal printed injection mold with different conformal cooling channels," *The International Journal of Advanced Manufacturing Technology,* vol. 107, no. 3-4, pp. 1223-1238, 2020.

[9] H.-S. Park, X.-P. Dang, D.-S. Nguyen, and S. Kumar, "Design of advanced injection mold to increase cooling efficiency," *International Journal of Precision Engineering and Manufacturing-Green Technology,* vol. 7, no. 2, pp. 319-328, 2020.

[10] J. M. Mercado-Colmenero, C. Martin-Doñate, M. Rodriguez-Santiago, F. Moral-Pulido, and M. A. Rubio-Paramio, "A new conformal cooling lattice design procedure for injection molding applications based on expert algorithms," *The International Journal of Advanced Manufacturing Technology,* vol. 102, no. 5, pp. 1719-1746, 2019.

[11] C. Tan *et al.*, "Design and additive manufacturing of novel conformal cooling molds," *Materials & Design,* vol. 196, p. 109147, 2020.

[12] P. A. Gruber and D. A. de Miranda, "Heat transfer simulation for decision making in plastic injection mold design," *Polímeros,* vol. 30, 2020.

[13] C.-C. Kuo and W.-C. Xu, "Effects of different cooling channels on the cooling efficiency in the wax injection molding process," *The International Journal of Advanced Manufacturing Technology,* vol. 98, no. 1, pp. 887-895, 2018.

[14] V. Brøtan, O. Å. Berg, and K. Sørby, "Additive manufacturing for enhanced performance of molds," *Procedia Cirp,* vol. 54, pp. 186-190, 2016.

[15] K. V. Wong and A. Hernandez, "A review of additive manufacturing," *International scholarly research notices*, vol. 2012, 2012.
[16] I. Gibson *et al.*, *Additive manufacturing technologies*. Springer, 2021.
[17] O. Abdulhameed, A. Al-Ahmari, W. Ameen, and S. H. Mian, "Additive manufacturing: Challenges, trends, and applications," *Advances in Mechanical Engineering*, vol. 11, no. 2, p. 1687814018822880, 2019.
[18] D. Herzog, V. Seyda, E. Wycisk, and C. Emmelmann, "Additive manufacturing of metals," *Acta Materialia*, vol. 117, pp. 371-392, 2016.
[19] R. A. Mesquita, *Tool steels: properties and performance*. CRC press, 2016.
[20] J. A. Szumera, *The tool steel guide*. Industrial Press Inc., 2003.
[21] P. Deng, M. Karadge, R. B. Rebak, V. K. Gupta, B. C. Prorok, and X. Lou, "The origin and formation of oxygen inclusions in austenitic stainless steels manufactured by laser powder bed fusion," *Additive Manufacturing*, vol. 35, p. 101334, 2020.
[22] T. Larimian, M. Kannan, D. Grzesiak, B. AlMangour, and T. Borkar, "Effect of energy density and scanning strategy on densification, microstructure and mechanical properties of 316L stainless steel processed via selective laser melting," *Materials Science and Engineering: A*, vol. 770, p. 138455, 2020.
[23] J. H. Tan, W. L. E. Wong, and K. W. Dalgarno, "An overview of powder granulometry on feedstock and part performance in the selective laser melting process," *Additive Manufacturing*, vol. 18, pp. 228-255, 2017.
[24] H.-Z. Jiang *et al.*, "Factor analysis of selective laser melting process parameters with normalised quantities and Taguchi method," *Optics & Laser Technology*, vol. 119, p. 105592, 2019.
[25] P. Wołosz, A. Baran, and M. Polański, "The influence of laser engineered net shaping (LENS™) technological parameters on the laser deposition efficiency and properties of H13 (AISI) steel," *Journal of Alloys and Compounds*, vol. 823, p. 153840, 2020.
[26] R. Mertens, B. Vrancken, N. Holmstock, Y. Kinds, J.-P. Kruth, and J. Van Humbeeck, "Influence of powder bed preheating on microstructure and mechanical properties of H13 tool steel SLM parts," *Physics Procedia*, vol. 83, pp. 882-890, 2016.
[27] J. Lee, J. Choe, J. Park, J.-H. Yu, S. Kim, and H. Sung, "Microstructural effects on the tensile and fracture behavior of selective laser melted H13 tool steel under varying conditions," *Materials Characterization*, vol. 155, p. 109817, 2019.
[28] M. Åsberg, G. Fredriksson, S. Hatami, W. Fredriksson, and P. Krakhmalev, "Influence of post treatment on microstructure, porosity and mechanical properties of additive manufactured H13 tool steel," *Materials Science and Engineering: A*, vol. 742, pp. 584-589, 2019.
[29] B. Ren, D. Lu, R. Zhou, Z. Li, and J. Guan, "Preparation and mechanical properties of selective laser melted H13 steel," *Journal of Materials Research*, vol. 34, no. 8, pp. 1415-1425, 2019.
[30] A. M. Vilardell *et al.*, "Evaluation of post-treatments of novel hot-work tool steel manufactured by laser powder bed fusion for aluminum die casting applications," *Materials Science and Engineering: A*, vol. 800, p. 140305, 2021.

[31] A. Bohlen, H. Freiße, M. Hunkel, and F. Vollertsen, "Additive manufacturing of tool steel by laser metal deposition," *Procedia Cirp,* vol. 74, pp. 192-195, 2018.
[32] Y.-a. Min *et al.*, "Influence of different surface treatments of H13 hot work die steel on its thermal fatigue behaviors," *Journal of Shanghai University (English Edition),* vol. 5, no. 4, pp. 326-330, 2001.
[33] M. Šebek, L. Falat, F. Kováč, I. Petryshynets, P. Horňak, and V. Girman, "The effects of laser surface hardening on microstructural characteristics and wear resistance of AISI H11 hot work tool steel," *Archives of Metallurgy and Materials,* 2017.
[34] J. Zhang *et al.*, "The effect of laser energy density on the microstructure, residual stress and phase composition of H13 steel treated by laser surface melting," *Journal of Alloys and Compounds,* vol. 856, p. 158168, 2021.
[35] I. Kabir, D. Yin, N. Tamanna, and S. Naher, "Thermomechanical modelling of laser surface glazing for H13 tool steel," *Applied Physics A,* vol. 124, no. 3, pp. 1-9, 2018.
[36] S. Paul, K. Thool, R. Singh, I. Samajdar, and W. Yan, "Experimental characterization of clad microstructure and its correlation with residual stresses," *Procedia Manufacturing,* vol. 10, pp. 804-818, 2017.
[37] B. Breidenstein, F. Brenne, L. Wu, T. Niendorf, and B. Denkena, "Effect of post-process machining on surface properties of additively manufactured H13 tool steel," *HTM Journal of Heat Treatment and Materials,* vol. 73, no. 4, pp. 173-186, 2018.
[38] T. Ermergen and F. Taylan, "Review on Surface Quality Improvement of Additively Manufactured Metals by Laser Polishing," *Arabian Journal for Science and Engineering,* vol. 46, no. 8, pp. 7125-7141, 2021.
[39] M. T. Chow, E. V. Bordatchev, and G. K. Knopf, "Experimental study on the effect of varying focal offset distance on laser micropolished surfaces," *The International Journal of Advanced Manufacturing Technology,* vol. 67, no. 9, pp. 2607-2617, 2013.
[40] M. Perez Dewey and D. Ulutan, "Development of laser polishing as an auxiliary post-process to improve surface quality in fused deposition modeling parts," in *International manufacturing science and engineering conference,* 2017, vol. 50732: American Society of Mechanical Engineers, p. V002T01A006.
[41] A. M. K. Hafiz, E. V. Bordatchev, and R. O. Tutunea-Fatan, "Influence of overlap between the laser beam tracks on surface quality in laser polishing of AISI H13 tool steel," *Journal of Manufacturing Processes,* vol. 14, no. 4, pp. 425-434, 2012.
[42] C. Nüsser, I. Wehrmann, and E. Willenborg, "Influence of intensity distribution and pulse duration on laser micro polishing," *Physics Procedia,* vol. 12, pp. 462-471, 2011.
[43] M. Kang, G. Park, J.-G. Jung, B.-H. Kim, and Y.-K. Lee, "The effects of annealing temperature and cooling rate on carbide precipitation behavior in H13 hot-work tool steel," *Journal of alloys and compounds,* vol. 627, pp. 359-366, 2015.
[44] G. Maistro, C. Oikonomou, S. B. Hosseini, and S. Brorson, "Quenching and hot isostatic pressing of additively manufactured tool steel," *Available at SSRN 3785874,* 2021.
[45] J. Wang, S. Liu, Y. Fang, and Z. He, "A short review on selective laser melting of H13 steel," *The International Journal of Advanced Manufacturing Technology,* vol. 108, no. 7, pp. 2453-2466, 2020.

[46] L. Wu, F. Xia, W. Gridin, S. Leuders, F. Brenne, and T. Niendorf, "Laser Beam Melting of H13 Tool Steel: From the Evolution of Microstructure to Process Simulation," *Euro PM Published in,* 2021.

[47] C. Chen *et al.*, "Effect of heat treatment on microstructure and mechanical properties of laser additively manufactured AISI H13 tool steel," *Journal of Materials Engineering and Performance,* vol. 26, no. 11, pp. 5577-5589, 2017.

[48] M. Katancik, S. Mirzababaei, M. Ghayoor, and S. Pasebani, "Selective laser melting and tempering of H13 tool steel for rapid tooling applications," *Journal of Alloys and Compounds,* vol. 849, p. 156319, 2020.

[49] J. Yan, H. Song, Y. Dong, W.-M. Quach, and M. Yan, "High strength (~ 2000 MPa) or highly ductile (~ 11%) additively manufactured H13 by tempering at different conditions," *Materials Science and Engineering: A,* vol. 773, p. 138845, 2020.

[50] F.-J. Shiou and C.-H. Chen, "Freeform surface finish of plastic injection mold by using ball-burnishing process," *Journal of materials processing technology,* vol. 140, no. 1-3, pp. 248-254, 2003.

[51] E. B. Fonseca, A. H. Gabriel, L. C. Araújo, P. L. Santos, K. N. Campo, and E. S. Lopes, "Assessment of laser power and scan speed influence on microstructural features and consolidation of AISI H13 tool steel processed by additive manufacturing," *Additive Manufacturing,* vol. 34, p. 101250, 2020.

[52] J. W. Zhihao Wei, Nan Shi, Lei Li, "Review of conformal cooling system design and additive manufacturing for " *Mathematical Biosciences and Engineering,* vol. 17, no. 5, pp. 5414-5431, 12 august 2020 2020, doi: 10.3934/mbe.2020292.

[53] G. Tosello *et al.*, "Value chain and production cost optimization by integrating additive manufacturing in injection molding process chain," *The International Journal of Advanced Manufacturing Technology,* vol. 100, no. 1-4, pp. 783-795, 2019.

[54] C. Achillas, D. Tzetzis, and M. O. Raimondo, "Alternative production strategies based on the comparison of additive and traditional manufacturing technologies," *International Journal of Production Research,* vol. 55, no. 12, pp. 3497-3509, 2017.

[55] C. Yan, L. Hao, A. Hussein, and D. Raymont, "Evaluations of cellular lattice structures manufactured using selective laser melting," *International Journal of Machine Tools and Manufacture,* vol. 62, pp. 32-38, 2012.

[56] N. Chantarapanich *et al.*, "Fabrication of three-dimensional honeycomb structure for aeronautical applications using selective laser melting: a preliminary investigation," *Rapid Prototyping Journal,* 2014.

[57] A. du Plessis *et al.*, "Beautiful and functional: a review of biomimetic design in additive manufacturing, Addit. Manuf. 27 (2019) 408–427," ed.

[58] D. Kang, S. Park, Y. Son, S. Yeon, S. H. Kim, and I. Kim, "Multi-lattice inner structures for high-strength and light-weight in metal selective laser melting process," *Materials & Design,* vol. 175, p. 107786, 2019.

[59] A. Seharing, A. H. Azman, and S. Abdullah, "A review on integration of lightweight gradient lattice structures in additive manufacturing parts," *Advances in Mechanical Engineering,* vol. 12, no. 6, p. 1687814020916951, 2020.

[60] C. Malca, C. Santos, M. Sena, and A. Mateus, "Development of SLM cellular structures for injection molds manufacturing," *Science and Technology of Materials*, vol. 30, no. 1, pp. 13-22, 2018.
[61] T. Wu and A. Tovar, "Multiscale, thermomechanical topology optimization of self-supporting cellular structures for porous injection molds," *Rapid Prototyping Journal*, 2019.
[62] F. Marin, J. R. de Miranda, and A. F. de Souza, "Study of the design of cooling channels for polymers injection molds," *Polymer Engineering & Science*, vol. 58, no. 4, pp. 552-559, 2018.
[63] Y. Wang, K.-M. Yu, and C. C. Wang, "Spiral and conformal cooling in plastic injection molding," *Computer-Aided Design*, vol. 63, pp. 1-11, 2015.
[64] S. Marques, A. F. d. Souza, J. Miranda, and I. Yadroitsau, "Design of conformal cooling for plastic injection moulding by heat transfer simulation," *Polímeros*, vol. 25, pp. 564-574, 2015.
[65] C.-C. Kuo, Z.-F. Jiang, and J.-H. Lee, "Effects of cooling time of molded parts on rapid injection molds with different layouts and surface roughness of conformal cooling channels," *The International Journal of Advanced Manufacturing Technology*, vol. 103, no. 5, pp. 2169-2182, 2019.
[66] B. Müller, R. Hund, R. Malek, and N. Gerth, "Laser beam melting for tooling applications–new perspectives for resource-efficient metal forming and die casting processes," in *IFIP International Conference on Digital Product and Process Development Systems*, 2013: Springer, pp. 124-137.
[67] M. Sony and S. Naik, "Key ingredients for evaluating Industry 4.0 readiness for organizations: a literature review," *Benchmarking: An International Journal*, 2019.
[68] X. Zhou, X. Liu, D. Zhang, Z. Shen, and W. Liu, "Balling phenomena in selective laser melted tungsten," *Journal of Materials Processing Technology*, vol. 222, pp. 33-42, 2015.
[69] P. Laakso *et al.*, "Optimization and simulation of SLM process for high density H13 tool steel parts," *Physics Procedia*, vol. 83, pp. 26-35, 2016.
[70] J. Yan *et al.*, "Selective laser melting of H13: microstructure and residual stress," *Journal of Materials Science*, vol. 52, no. 20, pp. 12476-12485, 2017.
[71] M. Narvan, K. S. Al-Rubaie, and M. Elbestawi, "Process-structure-property relationships of AISI H13 tool steel processed with selective laser melting," *Materials*, vol. 12, no. 14, p. 2284, 2019.
[72] M. Zhao, C. Duan, and X. Luo, "Metallurgical defect behavior, microstructure evolution, and underlying thermal mechanisms of metallic parts fabricated by selective laser melting additive manufacturing," *Journal of Laser Applications*, vol. 32, no. 2, p. 022012, 2020.
[73] T. Kurzynowski, W. Stopyra, K. Gruber, G. Ziółkowski, B. Kuźnicka, and E. Chlebus, "Effect of scanning and support strategies on relative density of SLM-ed H13 steel in relation to specimen size," *Materials*, vol. 12, no. 2, p. 239, 2019.
[74] M. Yonehara *et al.*, "Parameter optimization of the high-power laser powder bed fusion process for H13 tool steel," *The International Journal of Advanced Manufacturing Technology*, vol. 110, no. 1, pp. 427-437, 2020.

[75] I. Mutlu, E. Oktay, and S. Ekinci, "Characterization of microstructure of H13 tool steel using ultrasonic measurements," *Russian Journal of Nondestructive Testing*, vol. 49, no. 2, pp. 112-120, 2013.
[76] L. Xue, "Laser Consolidation—A rapid manufacturing process for making net-shape functional components," in *Advances in laser materials processing*: Elsevier, 2018, pp. 461-505.
[77] F. Lei *et al.*, "Microstructures and mechanical properties of H13 tool steel fabricated by selective laser melting," *Materials*, vol. 15, no. 7, p. 2686, 2022.
[78] S. Shakerin, M. Sanjari, B. S. Amirkhiz, and M. Mohammadi, "Interface engineering of additively manufactured maraging steel-H13 bimetallic structures," *Materials Characterization*, vol. 170, p. 110728, 2020.
[79] J. F. Garcias *et al.*, "Quasistatic and fatigue behavior of an AISI H13 steel obtained by additive manufacturing and conventional method," *Fatigue & Fracture of Engineering Materials & Structures*, 2021.
[80] M. Pellizzari, B. AlMangour, M. Benedetti, S. Furlani, D. Grzesiak, and F. Deirmina, "Effects of building direction and defect sensitivity on the fatigue behavior of additively manufactured H13 tool steel," *Theoretical and Applied Fracture Mechanics*, vol. 108, p. 102634, 2020.
[81] R. Dörfert, J. Zhang, B. Clausen, H. Freiße, J. Schumacher, and F. Vollertsen, "Comparison of the fatigue strength between additively and conventionally fabricated tool steel 1.2344," *Additive Manufacturing*, vol. 27, pp. 217-223, 2019.
[82] M. Mazur, P. Brincat, M. Leary, and M. Brandt, "Numerical and experimental evaluation of a conformally cooled H13 steel injection mould manufactured with selective laser melting," *The International Journal of Advanced Manufacturing Technology*, vol. 93, no. 1, pp. 881-900, 2017.
[83] M. Wang, Y. Wu, Q. Wei, and Y. Shi, "Thermal fatigue properties of H13 Hot-work tool steels processed by selective laser melting," *Metals*, vol. 10, no. 1, p. 116, 2020.
[84] J. Li, Y. Shi, and X. Wu, "Effect of initial hardness on the thermal fatigue behavior of AISI H13 steel by experimental sand numerical investigations," *Fatigue & Fracture of Engineering Materials & Structures*, vol. 41, no. 6, pp. 1260-1274, 2018.
[85] X. Tong, M.-j. Dai, and Z.-h. Zhang, "Thermal fatigue resistance of H13 steel treated by selective laser surface melting and CrNi alloying," *Applied Surface Science*, vol. 271, pp. 373-380, 2013.
[86] B. Liu, B. Wang, X. Yang, X. Zhao, M. Qin, and J. Gu, "Thermal fatigue evaluation of AISI H13 steels surface modified by gas nitriding with pre-and post-shot peening," *Applied Surface Science*, vol. 483, pp. 45-51, 2019.
[87] C. Meng *et al.*, "Effect of pulse current stimulation on wear and thermal fatigue behavior of biomimetic H13 steel processed by laser surface melting," *JOM*, vol. 70, no. 11, pp. 2611-2618, 2018.
[88] M. Sarwar, R. Priestner, and E. Ahmad, "Influence of martensite volume fraction on fatigue limit of a dual-phase steel," *Journal of materials engineering and performance*, vol. 11, no. 3, pp. 274-277, 2002.

[89] F. Deirmina, N. Peghini, B. AlMangour, D. Grzesiak, and M. Pellizzari, "Heat treatment and properties of a hot work tool steel fabricated by additive manufacturing," *Materials Science and Engineering: A*, vol. 753, pp. 109-121, 2019.
[90] E. Maleki, S. Bagherifard, M. Bandini, and M. Guagliano, "Surface post-treatments for metal additive manufacturing: Progress, challenges, and opportunities," *Additive Manufacturing*, vol. 37, p. 101619, 2021.
[91] L. Hackel, J. R. Rankin, A. Rubenchik, W. E. King, and M. Matthews, "Laser peening: A tool for additive manufacturing post-processing," *Additive Manufacturing*, vol. 24, pp. 67-75, 2018.
[92] M. Hofele, J. Schanz, B. Burzic, S. Lutz, M. Merkel, and H. Riegel, "Laser based post processing of additive manufactured metal parts," *Lasers in Manuf LIM*, 2017.
[93] M. Steinhauser, E. Sert, L. Hitzler, A. Öchsner, and M. Merkel, "Fatigue Behavior of the Additively Manufactured Tool Steel H13 after Surface Treatment using Different Post-Processing Methods," *Practical Metallography*, vol. 57, no. 3, pp. 140-167, 2020.
[94] M. Mazur, M. Leary, M. McMillan, J. Elambasseril, and M. Brandt, "SLM additive manufacture of H13 tool steel with conformal cooling and structural lattices," *Rapid Prototyping Journal*, vol. 22, no. 3, pp. 504-518, 2016.
[95] Z. C. Zhou, J. Du, Y.-J. Yan, and C.-L. Shen, "The recent development of study on H13 hot-work die steel," *Solid State Phenomena*, vol. 279, pp. 55-59, 2018.
[96] X. Xu, E. Sachs, and S. Allen, "The design of conformal cooling channels in injection molding tooling," *Polymer Engineering & Science*, vol. 41, no. 7, pp. 1265-1279, 2001.
[97] A. Saifullah and S. H. Masood, "Cycle time reduction in injection moulding with conformal cooling channels," in *Proceedings of the international conference on mechanical engineering*, 2007, pp. 29-31.
[98] A. Y. Al-Maharma, S. P. Patil, and B. Markert, "Effects of porosity on the mechanical properties of additively manufactured components: a critical review," *Materials Research Express*, vol. 7, no. 12, p. 122001, 2020.
[99] N. M. H. Alamri, M. Packianather, and S. Bigot, "Predicting the porosity in selective laser melting parts using hybrid regression convolutional neural network," *Applied Sciences*, vol. 12, no. 24, p. 12571, 2022.
[100] Q. Tan, Y. Liu, Z. Fan, J. Zhang, Y. Yin, and M.-X. Zhang, "Effect of processing parameters on the densification of an additively manufactured 2024 Al alloy," *Journal of Materials Science & Technology*, vol. 58, pp. 34-45, 2020.
[101] K. Darvish, Z. Chen, and T. Pasang, "Reducing lack of fusion during selective laser melting of CoCrMo alloy: Effect of laser power on geometrical features of tracks," *Materials & Design*, vol. 112, pp. 357-366, 2016.
[102] L. Mrňa, M. Šarbort, Š. Řeřucha, and P. Jedlička, "Correlation between the keyhole depth and the frequency characteristics of light emissions in laser welding," *Physics Procedia*, vol. 41, pp. 469-477, 2013.
[103] A. Sola and A. Nouri, "Microstructural porosity in additive manufacturing: The formation and detection of pores in metal parts fabricated by powder bed fusion," *Journal of Advanced Manufacturing and Processing*, vol. 1, no. 3, p. e10021, 2019.

[104] M. Narvan, K. Al-Rubaie, and M. Elbestawi, "Process-structureproperty relationships of AISI H13 tool steel processed with selective laser melting. Materials (Basel) 12: 2284," ed, 2019.
[105] S. Katayama, "Introduction: fundamentals of laser welding," in *Handbook of laser welding technologies*: Elsevier, 2013, pp. 3-16.
[106] Y. A. Mayi, M. Dal, P. Peyre, M. Bellet, and R. Fabbro, "Physical mechanisms of conduction-to-keyhole transition in laser welding and additive manufacturing processes," *Optics & Laser Technology,* vol. 158, p. 108811, 2023.
[107] S. Cooke, K. Ahmadi, S. Willerth, and R. Herring, "Metal additive manufacturing: Technology, metallurgy and modelling," *Journal of Manufacturing Processes,* vol. 57, pp. 978-1003, 2020.
[108] N. Omidi, P. Farhadipour, L. Baali, K. Bensalem, N. Barka, and M. Jahazi, "A comprehensive review of additively manufactured H13 tool steel applicable in the injection mold industry: Applications, designs, microstructure, mechanical properties," *Jom,* vol. 75, no. 11, pp. 4457-4469, 2023.
[109] T. Larimian, B. AlMangour, D. Grzesiak, G. Walunj, and T. Borkar, "Effect of laser spot size, scanning strategy, scanning speed, and laser power on microstructure and mechanical behavior of 316L stainless steel fabricated via selective laser melting," *Journal of Materials Engineering and Performance,* pp. 1-20, 2021.
[110] Y. Wang and J. Shi, "Influence of laser scan speed on micro-segregation in selective laser melting of an iron-carbon alloy: A multi-scale simulation study," *Procedia Manufacturing,* vol. 26, pp. 941-951, 2018.
[111] Y. Zhong, L. Liu, S. Wikman, D. Cui, and Z. Shen, "Intragranular cellular segregation network structure strengthening 316L stainless steel prepared by selective laser melting," *Journal of Nuclear Materials,* vol. 470, pp. 170-178, 2016.
[112] M. Yeganeh, Z. Shahryari, A. Talib Khanjar, Z. Hajizadeh, and F. Shabani, "Inclusions and segregations in the selective Laser-melted alloys: a review," *Coatings,* vol. 13, no. 7, p. 1295, 2023.
[113] S. Gao *et al.*, "Recrystallization-based grain boundary engineering of 316L stainless steel produced via selective laser melting," *Acta Materialia,* vol. 200, pp. 366-377, 2020.
[114] K. Prashanth and J. Eckert, "Formation of metastable cellular microstructures in selective laser melted alloys," *Journal of Alloys and Compounds,* vol. 707, pp. 27-34, 2017.
[115] M. Zhang *et al.*, "Laser additive manufacturing of M2 high-speed steel," *Materials Science and Technology,* vol. 34, no. 1, pp. 69-78, 2018.
[116] S. Ghosh, M. R. Stoudt, L. E. Levine, and J. E. Guyer, "Formation of Nb-rich droplets in laser deposited Ni-matrix microstructures," *Scripta Materialia,* vol. 146, pp. 36-40, 2018.
[117] N. Haghdadi, M. Laleh, M. Moyle, and S. Primig, "Additive manufacturing of steels: a review of achievements and challenges," *Journal of Materials Science,* vol. 56, pp. 64-107, 2021.

[118] P. Ji, Z. Wang, Y. Mu, Y. Jia, and G. Wang, "Microstructural evolution of (FeCoNi) 85.84 Al7. 07Ti7. 09 high-entropy alloy fabricated by an optimized selective laser melting process," *Materials & Design,* vol. 224, p. 111326, 2022.
[119] Y. Sun *et al.*, "Thermal and mechanical properties of selective laser melted and heat treated H13 hot work tool steel," *Materials & Design,* vol. 224, p. 111295, 2022.
[120] J. Xie *et al.*, "Mesoscopic segregation in H13 steel molten pool during laser remelting: a combined influence of Marangoni convection and oxidation," *Journal of Materials Processing Technology,* vol. 316, p. 117956, 2023.
[121] H. Chen, Q. Fang, K. Zhou, Y. Liu, and J. Li, "Unraveling atomic-scale crystallization and microstructural evolution of a selective laser melted FeCrNi medium-entropy alloy," *CrystEngComm,* vol. 22, no. 24, pp. 4136-4146, 2020.
[122] G. Yang, Y. Xie, S. Zhao, L. Qin, X. Wang, and B. Wu, "Quality control: Internal defects formation mechanism of selective laser melting based on laser-powder-melt pool interaction: A review," *Chinese Journal of Mechanical Engineering: Additive Manufacturing Frontiers,* p. 100037, 2022.
[123] R. Li, J. Liu, Y. Shi, L. Wang, and W. Jiang, "Balling behavior of stainless steel and nickel powder during selective laser melting process," *The International Journal of Advanced Manufacturing Technology,* vol. 59, pp. 1025-1035, 2012.
[124] S. Liu and H. Guo, "Balling behavior of selective laser melting (SLM) magnesium alloy," *Materials,* vol. 13, no. 16, p. 3632, 2020.
[125] C. Zöller, N. Adams, and S. Adami, "Numerical investigation of balling defects in laser-based powder bed fusion of metals with Inconel 718," *Additive Manufacturing,* vol. 73, p. 103658, 2023.
[126] W. Di, Y. Yongqiang, S. Xubin, and C. Yonghua, "Study on energy input and its influences on single-track, multi-track, and multi-layer in SLM," *The International Journal of Advanced Manufacturing Technology,* vol. 58, pp. 1189-1199, 2012.
[127] D. Gu and Y. Shen, "Balling phenomena in direct laser sintering of stainless steel powder: Metallurgical mechanisms and control methods," *Materials & Design,* vol. 30, no. 8, pp. 2903-2910, 2009.
[128] H. Rezaeifar and M. Elbestawi, "Porosity formation mitigation in laser powder bed fusion process using a control approach," *Optics & Laser Technology,* vol. 147, p. 107611, 2022.
[129] A. K. Agrawal, B. Rankouhi, and D. J. Thoma, "Predictive process mapping for laser powder bed fusion: A review of existing analytical solutions," *Current Opinion in Solid State and Materials Science,* vol. 26, no. 6, p. 101024, 2022.
[130] M. Awd, J. Johannsen, S. Siddique, C. Emmelmann, and F. Walther, "Qualification of selective laser-melted Al alloys against fatigue damage by means of measurement and modeling techniques," in *MATEC Web of Conferences,* 2018, vol. 165: EDP Sciences, p. 02001.
[131] H. Choo *et al.*, "Effect of laser power on defect, texture, and microstructure of a laser powder bed fusion processed 316L stainless steel," *Materials & Design,* vol. 164, p. 107534, 2019.

[132] M. D. Sangid, P. Ravi, V. Prithivirajan, N. A. Miller, P. Kenesei, and J.-S. Park, "ICME approach to determining critical pore size of IN718 produced by selective laser melting," *Jom*, vol. 72, pp. 465-474, 2020.
[133] M. Awd, J. Tenkamp, M. Hirtler, S. Siddique, M. Bambach, and F. Walther, "Comparison of microstructure and mechanical properties of Scalmalloy® produced by selective laser melting and laser metal deposition," *Materials*, vol. 11, no. 1, p. 17, 2017.
[134] Y. Liu, Y. Yang, and D. Wang, "A study on the residual stress during selective laser melting (SLM) of metallic powder," *The International Journal of Advanced Manufacturing Technology*, vol. 87, pp. 647-656, 2016.
[135] H. Vemanaboina, P. Ferro, B. S. Babu, E. Gundabattini, K. Kumar, and F. Berto, "Residual Stress Distribution in Selective Laser Melting of SS316L Parts," *Advances in Materials Science and Engineering*, vol. 2022, 2022.
[136] D. Wang *et al.*, "The effect of a scanning strategy on the residual stress of 316L steel parts fabricated by selective laser melting (SLM)," *Materials*, vol. 11, no. 10, p. 1821, 2018.
[137] I. Yadroitsev and I. Yadroitsava, "Evaluation of residual stress in stainless steel 316L and Ti6Al4V samples produced by selective laser melting, Virtual Phys. Prototyp. 10 (2015) 67–76," ed, 2015.
[138] J. Yan *et al.*, "Selective laser melting of H13: microstructure and residual stress," *Journal of Materials Science*, vol. 52, pp. 12476-12485, 2017.
[139] M. Narvan, A. Ghasemi, E. Fereiduni, S. Kendrish, and M. Elbestawi, "Part deflection and residual stresses in laser powder bed fusion of H13 tool steel," *Materials & Design*, vol. 204, p. 109659, 2021.
[140] N. Omidi, P. Farhadipour, L. Baali, K. Bensalem, N. Barka, and M. Jahazi, "A comprehensive review of additively manufactured H13 tool steel applicable in the injection mold industry: Applications, designs, microstructure, mechanical properties," *JOM*, pp. 1-13, 2023.
[141] G. Huang, K. Wei, and X. Zeng, "Microstructure and mechanical properties of H13 tool steel fabricated by high power laser powder bed fusion," *Materials Science and Engineering: A*, vol. 858, p. 144154, 2022.
[142] C. Chen *et al.*, "Effect of heat treatment on microstructure and mechanical properties of laser additively manufactured AISI H13 tool steel," *Journal of Materials Engineering and Performance*, vol. 26, pp. 5577-5589, 2017.
[143] A. Ning, Y. Liu, R. Gao, S. Yue, M. Wang, and H. Guo, "Effect of Tempering Condition on Microstructure, Mechanical Properties and Precipitates in AISI H13 Steel," *JOM*, vol. 73, no. 7, pp. 2194-2202, 2021.
[144] W. Prudente, J. F. C. Lins, R. Siqueira, and S. Priscila, "Microstructural evolution under tempering heat treatment in AISI H13 hot-work tool steel," *International journal of engineering research and applications*, vol. 7, no. 4, pp. 67-71, 2017.
[145] H.-S. Park and X.-P. Dang, "Development of a smart plastic injection mold with conformal cooling channels," *Procedia Manufacturing*, vol. 10, pp. 48-59, 2017.
[146] P. A. Gruber and D. A. de Miranda, "Heat transfer simulation for decision making in plastic injection mold design," *Polímeros*, vol. 30, p. e2020005, 2020.

[147] S. Shen, B. B. Kanbur, Y. Zhou, and F. Duan, "Thermal and mechanical analysis for conformal cooling channel in plastic injection molding," *Materials Today: Proceedings,* vol. 28, pp. 396-401, 2020.
[148] J. M. Mercado-Colmenero, C. Martin-Doñate, M. Rodriguez-Santiago, F. Moral-Pulido, and M. A. Rubio-Paramio, "A new conformal cooling lattice design procedure for injection molding applications based on expert algorithms," *The International Journal of Advanced Manufacturing Technology,* vol. 102, pp. 1719-1746, 2019.
[149] T. Wu and A. Tovar, "Multiscale, thermomechanical topology optimization of self-supporting cellular structures for porous injection molds," *Rapid Prototyping Journal,* vol. 25, no. 9, pp. 1482-1492, 2019.
[150] S. L. Sing and W. Y. Yeong, "Laser powder bed fusion for metal additive manufacturing: perspectives on recent developments," *Virtual and Physical Prototyping,* vol. 15, no. 3, pp. 359-370, 2020.
[151] E. Liverani, S. Toschi, L. Ceschini, and A. Fortunato, "Effect of selective laser melting (SLM) process parameters on microstructure and mechanical properties of 316L austenitic stainless steel," *Journal of Materials Processing Technology,* vol. 249, pp. 255-263, 2017.
[152] S. Akhtar *et al.*, "Direct selective laser sintering of tool steel powders to high density: part B-the effect on microstructural evolution," in *2003 International Solid Freeform Fabrication Symposium,* 2003.
[153] M. Pereira, M. Williams, and W. Du Preez, "Characterization of metal powder based rapid prototyping components under aluminium high pressure die casting process conditions," 2009.
[154] Y. Guanghua *et al.*, "Effects of heat treatment on mechanical properties of H13 steel," *Metal Science and Heat Treatment,* vol. 52, pp. 393-395, 2010.
[155] N. Angang, G. Hanjie, C. Xichun, and W. Mingbo, "Precipitation behaviors and strengthening of carbides in H13 steel during annealing," *Materials Transactions,* vol. 56, no. 4, pp. 581-586, 2015.
[156] J. Wang, Z. Xu, and X. Lu, "Effect of the quenching and tempering temperatures on the microstructure and mechanical properties of H13 steel," *Journal of materials engineering and performance,* vol. 29, pp. 1849-1859, 2020.
[157] G. Telasang, J. D. Majumdar, G. Padmanabham, and I. Manna, "Structure–property correlation in laser surface treated AISI H13 tool steel for improved mechanical properties," *Materials Science and Engineering: A,* vol. 599, pp. 255-267, 2014.
[158] A. Kardak, L. Bilich, and G. Sinclair, "Stress Concentration Factors for ASTM E8/E8M-15a Plate-Type Specimens for Tension Testing," *Journal of Testing and Evaluation,* vol. 45, no. 6, pp. 2294-2298, 2017.
[159] H. Jia, H. Sun, H. Wang, Y. Wu, and H. Wang, "Scanning strategy in selective laser melting (SLM): a review," *The International Journal of Advanced Manufacturing Technology,* vol. 113, pp. 2413-2435, 2021.
[160] E. B. Fonseca, A. H. Gabriel, L. C. Araujo, P. L. Santos, K. N. Campo, and E. S. Lopes, "Assessment of laser power and scan speed influence on microstructural features and consolidation of AISI H13 tool steel processed by additive manufacturing," *Additive Manufacturing,* vol. 34, p. 101250, 2020.

[161] V. Sarrak and G. Filippov, "Brittleness of martensite," *Metal Science and Heat Treatment,* vol. 20, no. 4, pp. 279-285, 1978.
[162] Q. Tan *et al.*, "Rationalization of brittleness and anisotropic mechanical properties of H13 steel fabricated by selective laser melting," *Scripta Materialia,* vol. 214, p. 114645, 2022.
[163] F. Qiu, "Surface transformation hardening of carbon steel with high power fiber laser," 2013.
[164] R. Tewari, D. Srivastava, G. Dey, J. Chakravarty, and S. Banerjee, "Microstructural evolution in zirconium based alloys," *Journal of Nuclear Materials,* vol. 383, no. 1-2, pp. 153-171, 2008.
[165] M. J. Holzweissig, A. Taube, F. Brenne, M. Schaper, and T. Niendorf, "Microstructural characterization and mechanical performance of hot work tool steel processed by selective laser melting," *Metallurgical and Materials Transactions B,* vol. 46, pp. 545-549, 2015.
[166] H. Chen, D. Gu, D. Dai, C. Ma, and M. Xia, "Microstructure and composition homogeneity, tensile property, and underlying thermal physical mechanism of selective laser melting tool steel parts," *Materials Science and Engineering: A,* vol. 682, pp. 279-289, 2017.
[167] M. Rashid, "Dual phase steels," *Annual Review of Materials Science,* vol. 11, no. 1, pp. 245-266, 1981.
[168] X.-L. Cai, A. Garratt-Reed, and W. Owen, "The development of some dual-phase steel structures from different starting microstructures," *Metallurgical Transactions A,* vol. 16, pp. 543-557, 1985.
[169] G. Karthik and H. S. Kim, "Heterogeneous aspects of additive manufactured metallic parts: a review," *Metals and Materials International,* vol. 27, pp. 1-39, 2021.
[170] A. C. S. Sabioni, R. P. B. Ramos, V. Ji, and F. Jomard, "Oxygen diffusion study in oxidation films of the AISI 304 austenitic stainless steel," in *Defect and Diffusion Forum*, 2012, vol. 323: Trans Tech Publ, pp. 345-351.
[171] C. Herzig and Y. Mishin, "Grain boundary diffusion in metals," in *Diffusion in condensed matter: methods, materials, models*: Springer, 2005, pp. 337-366.
[172] Q. Chao, S. Thomas, N. Birbilis, P. Cizek, P. D. Hodgson, and D. Fabijanic, "The effect of post-processing heat treatment on the microstructure, residual stress and mechanical properties of selective laser melted 316L stainless steel," *Materials Science and Engineering: A,* vol. 821, p. 141611, 2021.
[173] A. Ning, S. Yue, R. Gao, L. Li, and H. Guo, "Influence of tempering time on the behavior of large carbides' coarsening in aisi h13 steel," *Metals,* vol. 9, no. 12, p. 1283, 2019.
[174] A. Ning, W. Mao, X. Chen, H. Guo, and J. Guo, "Precipitation behavior of carbides in H13 hot work die steel and its strengthening during tempering," *Metals,* vol. 7, no. 3, p. 70, 2017.
[175] M. Lin, X. Zhao, L. Han, Q. Liu, and J. Gu, "Microstructural evolution and carbide precipitation in a heat-treated H13 hot work mold steel," *Metallography, Microstructure, and Analysis,* vol. 5, pp. 520-527, 2016.

[176] J. Li, J. Li, L. Wang, and L. Li, "Study on carbide in forged and annealed H13 hot work die steel," *High Temperature Materials and Processes,* vol. 34, no. 6, pp. 593-598, 2015.
[177] J. Zhu, Z. Zhang, and J. Xie, "Improving strength and ductility of H13 die steel by pre-tempering treatment and its mechanism," *Materials Science and Engineering: A,* vol. 752, pp. 101-114, 2019.
[178] A. Samuel and K. N. Prabhu, "Residual stress and distortion during quench hardening of steels: a review," *Journal of Materials Engineering and Performance,* vol. 31, no. 7, pp. 5161-5188, 2022.
[179] F. Lei, T. Wen, H. Yang, J. Fu, and J. Wang, "Microstructures and Mechanical Properties of H13 Tool Steel Processed by Selective Laser Melting," *Hailin and Fu, Junwei and Wang, Jiong and ji, shouxun, Microstructures and Mechanical Properties of H13 Tool Steel Processed by Selective Laser Melting*.
[180] G. Bansal *et al.*, "Influence of quenching strategy on phase transformation and mechanical properties of low alloy steel," *Materials Science and Engineering: A,* vol. 826, p. 141937, 2021.
[181] J. Hidalgo, M. Vittorietti, H. Farahani, F. Vercruysse, R. Petrov, and J. Sietsma, "Influence of M23C6 carbides on the heterogeneous strain development in annealed 420 stainless steel," *Acta Materialia,* vol. 200, pp. 74-90, 2020.
[182] A. l. Goodall, "Effect of initial microstructural conditions and tempering parameters on the carbide characteristics and hardness of alloyed quenched and tempered steel " Doctor of philosophy, School of Metallurgy and Material Science University of Birmingham 2019.